Czech Technical University in Prague

Faculty of Nuclear Sciences and Physical Engineering

Department of Physics
Study program: Nuclear and Particle Physics

Global polarization of hyperons in STAR Beam Energy Scan

DIPLOMA THESIS

Author:	Bc. Ondřej Lomický
Supervisor:	Dr. Barbara Trzeciak, Ph.D.
Year:	2022

České vysoké učení technické v Praze
Fakulta jaderná a fyzikálně inženýrská

Katedra fyziky
Studijní program: Jaderná a částicová fyzika

Globální polarizace hyperonů v energetickém skenu svazků na STARu

DIPLOMOVÁ PRÁCE

Vypracoval:	Bc. Ondřej Lomický
Vedoucí práce:	Dr. Barbara Trzeciak, Ph.D.
Rok:	2022

ČESKÉ VYSOKÉ UČENÍ TECHNICKÉ V PRAZE
FAKULTA JADERNÁ A FYZIKÁLNĚ INŽENÝRSKÁ
PRAHA 1 - STARÉ MĚSTO, BŘEHOVÁ 7 - PSČ 115 19

Katedra: fyziky   *Akademický rok:* 2021/2022

ZADÁNÍ DIPLOMOVÉ PRÁCE

Student: Bc. Ondřej Lomický

Studijní program: Jaderná a částicová fyzika

Název práce: Globální polarizace hyperonů v energetickém skenu svazků na STARu
(česky)

Název práce: Global polarization of hyperons in STAR Beam Energy Scan
(anglicky)

Pokyny pro vypracování:

1) Přehled současných experimentálních výsledků globální polarizace hyperonů ve srážkách těžkých jader

2) Polarizace hyperonů v relativistických hydrodynamických simulacích

3) Určení polarizace lambda hyperonu z dat STAR BES

4) Korekce na akceptanci a účinnost helicity

5) Vyhodnocení systematických chyb

6) Diskuze a závěr

Doporučená literatura:

[1] J. Kirsch, et. al.: Discoveries at the Frontiers of Science: From Nuclear Astrophysics to Relativistic Heavy Ion Collisions, J. Kirsch, et. al, Springer, 2020

[2] H. Satz: Extreme States of Matter in Strong Interaction Physics, Springer, 2018

[3] I. Karpenko, F. Becattini: Study of Lambda polarization in relativistic nuclear collisions at 7.7-200 GeV, Eur. Phys. J. C 77 213 (2017)

[4] I. Upsal: Global Polarization of the Lambda system in the STAR BES, Ph.D. Thesis, The Ohio State University, 2018

[5] J. Adam, et. al.: Global polarization of Lambda hyperons in Au+Au collisions at 200 GeV, Phys. Rev. C 98, 014910 (2018)

Jméno a pracoviště vedoucího diplomové práce:

Dr. Barbara Trzeciak, Ph.D., Katedra fyziky, Fakulta jaderná a fyzikálně inženýrská ČVUT v Praze
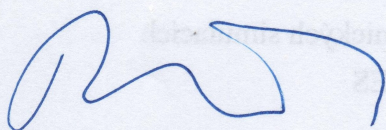
Jméno a pracoviště konzultanta:

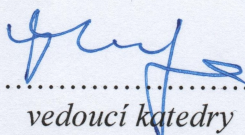doc. Mgr. Jaroslav Bielčík, Ph.D., Katedra fyziky, Fakulta jaderná a fyzikálně inženýrská ČVUT v Praze

Datum zadání diplomové práce: 20.10.2021
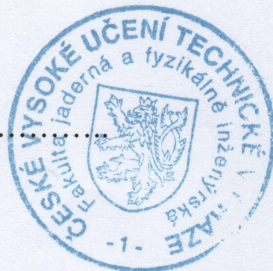
Termín odevzdání diplomové práce: 02.05.2022

Doba platnosti zadání je dva roky od data zadání.

....
garant studijního programu

....
vedoucí katedry

....
děkan

V Praze dne   20.10.2021

Prohlášení

Prohlašuji, že jsem svou diplomovou práci vypracoval samostatně a použil jsem pouze podklady (literaturu, projekty, SW atd.) uvedené v přiloženém seznamu.

Nemám závažný důvod proti použití tohoto školního díla ve smyslu § 60 Zákona č. 121/2000 Sb., o právu autorském, o právech souvisejících s právem autorským a o změně některých zákonů (autorský zákon).

V Praze dne ....
                                                              Bc. Ondřej Lomický

Poděkování

Chtěl bych velice poděkovat vedoucí mé diplomové práce Dr. Barbaře Trzeciak, Ph.D., za trpělivost, pomoc a velice podnětné rady. Dále bych rád poděkoval doc. Mgr. Jaroslavu Bielčíkovi, Ph.D., za pomoc v pochopení teoretické roviny této práce a také Iurimu Karpenkovi, Ph.D., za velkou trpělivost a pomoc s pochopením hydrodynamického modelu, obzvláště v těchto těžkých časech.

Bc. Ondřej Lomický

Název práce:
Globální polarizace hyperonů v energetickém skenu svazků na STARu

Autor: Bc. Ondřej Lomický

Studijní program: Jaderná a částicová fyzika
Druh práce: Diplomová práce

Vedoucí práce: Dr. Barbara Trzeciak, Ph.D.
    Katedra fyziky, Fakulta jaderná a fyzikálně inženýrská,
    České vysoké učení technické v Praze
Konzultant: doc. Mgr. Jaroslav Bielčík, Ph.D.
    Katedra fyziky, Fakulta jaderná a fyzikálně inženýrská,
    České vysoké učení technické v Praze

Abstrakt: Vysokoenergetické jádro-jaderné srážky mohou zformovat horké a husté skupenství hmoty, takzvané kvark-gluonové plazma. Tyto malé třesky jsou studovány v Brookhavenské národní laboratoři a CERNu. Studie odhalily, že kvark-gluonové plazma je nejen téměř dokonalá kapalina, ale i nejvířivější objekt, který byl kdy pozorován. Tato silná vířivost ovlivňuje orientaci spinu kvarků, jež jsou v tomto médiu, a následně i emitovaných částic. Hyperony, jako například Λ a $\overline{\Lambda}$, mohou být využity k určení této spinové orientace. Tato práce si klade za cíl rekonstrukci nestabilních Λ a $\overline{\Lambda}$ hyperonů a určení jejich globální spinové polarizace ve srážkách Au-Au s těžišťovou energií 27 GeV na experimentu STAR a v hydrodynamickém modelu.
Klíčová slova: STAR, hyperon, lambda, polarizace, Kálmánův filtr

Title:
Global polarization of hyperons in STAR Beam Energy Scan

Author: Bc. Ondřej Lomický

Abstract: High-energy heavy-ion collisions can create a hot and dense state of matter, the so-called Quark-gluon plasma. Those Little Bangs are studied at Brookhaven National Laboratory and CERN. The studies revealed that the Quark-gluon plasma is not only almost a perfect fluid but also the most vortical object ever observed. The strong vorticity influences the spin orientation of the quarks in the medium and subsequently the emitted particles. Hyperons, such as Λ and $\overline{\Lambda}$, can be used to determine the spin orientation. This thesis aims to reconstruct the unstable Λ and $\overline{\Lambda}$ hyperons and to determine their global spin polarization in Au-Au collisions at the center-of-mass energy of 27 GeV from the STAR experiment, and in the hydrodynamic model.
Key words: STAR, hyperon, lambda, polarization, Kalman filter

Contents

Introduction

The Quark-Gluon Plasma (QGP) is a state of matter with partonic, quarks and gluons, degrees of freedom. It is expected that the QGP existed in the early Universe just after the Big Bang. Nowadays, the QGP can be studied in a laboratory in the so-called Little Bangs created in relativistic heavy-ion collisions [1]. Since direct measurements of its properties is practically impossible due to the short lifetime of this matter (units of fm/c [2]), one uses various probes for its study. For example soft probes (particles with low transverse momenta $p_{\mathrm{T}} < 2$ GeV/c), hard probes (particles with high transverse momenta $p_{\mathrm{T}} > 10$ GeV/c) or electromagnetic probes (e.g. photons or dileptons) [3], [4]. The properties of the QGP can be successfully described by a hydrodynamical model [5]. For instance, this model revealed that the QGP is an almost perfect liquid [6].

Among many studied properties of the QGP is for instance its vorticity. The measured value of the QGP's vorticity reaches the highest value which has been ever observed in the universe [7]. The vorticity is a thermodynamic quantity and it can be perceived as a local rotation at a point in a fluid being parallel to the angular momentum of the whole medium [8]. Although the vorticity cannot be measured directly, there is a way how to reveal its value, i.e. by a particle polarization measurement. The vorticity can cause the spin orientation the emitted particles to be aligned with the global angular momentum. Therefore, a polarization measurement is based on a measurement of the alignment between the spin orientation of the emitted particles and the global angular momentum. However, the spin orientation of the emitted particle cannot be measured directly. Fortunately, baryons that are among the hyperons have the so-called self-analyzing nature of decay, i.e. the direction of the daughter decay baryon is highly correlated with the spin orientation of the mother hyperon. The best choice of the hyperon is Λ and $\overline{\Lambda}$ hyperons because of their relatively high abundance in heavy-ion collision.

In this thesis, the main goal is to extract the global Λ and $\overline{\Lambda}$ hyperon polarization from the data from Au-Au collisions at $\sqrt{s_{\mathrm{NN}}} = 27$ GeV, collected by the STAR experiment in 2018. The Λ and $\overline{\Lambda}$ particles are reconstructed via the most common decay into proton and pion by means of the Kalman Filter [9]. For purpose of the polarization measurement, the other task is the reconstruction of the event plane describing the geometry of the colliding nuclei. Then, the global Λ and $\overline{\Lambda}$ polarization is measured via two different analysis techniques, i.e. the invariant mass method and the event plane method. Different methods can help to estimate the precision of the result. Furthermore, other corrections are discussed, such as acceptance efficiency or helicity efficiency.

The hyperon polarization in relativistic heavy-ion collisions can be also extracted via the hydrodynamic model which is based on the assumption that the polarization of the quarks in the QGP is transferred to the emitted particles [10], [11].

The hyperon polarization compared to different model predictions could reveal the initial vorticity of the medium. The knowledge of the vorticity is crucial to the QGP modeling since the vorticity as the thermodynamic quantity can help to better understand the QGP formation and dynamics.

Chapter 1

Heavy-ion collisions

In this chapter, Standard Model (SM) of particle physics is briefly introduced including the basic information about the Quark-Gluon Plasma, heavy-ion collisions and the related observables.

1.1 Standard model

The standard model is the theory describing elementary particles and the interplay of three of four standard forces, namely strong, weak, and electromagnetic. The fourth, gravity, is still not included. Each of the included forces has the associated intermediating particles - so called force carriers.
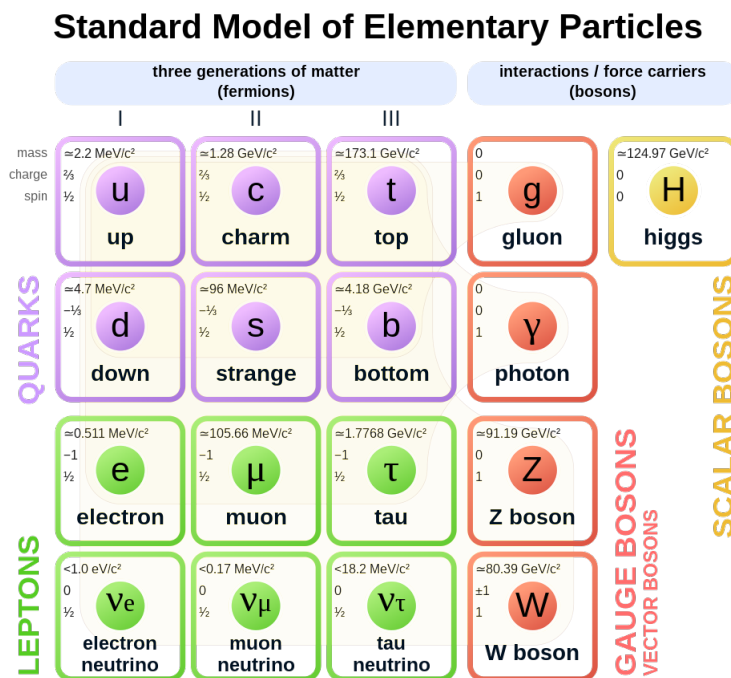

Figure 1.1: The standard model of elementary particles [12].

This model has shown that it successfully describes the high energy interaction of particles [13]. The correct prediction of the Higgs boson discovered by the ATLAS and CMS experiments at CERN's Large Hadron Collider (LHC) on 4th July 2012 can be considered a success of the SM and the big milestone in modern physics [14]. The particles of the SM can be divided into fundamental fermions and bosons according to whether their spin is non-integer and integer, respectively. The fundamental fermions are then divided into leptons and quarks, into 3 generations. The main differences are that leptons occur freely and do not interact via strong force contrary to quarks. The bosons are scalar (zero spin) or vector (nonzero spin). Each particle has a related antiparticle or is its own antiparticle.

A group of quarks forms hadrons. If a hadron consists of a quark and an antiquark (i.e. $q\overline{q}$), it is labeled as a meson. A group of 3 quarks or 3 antiquarks (i.e. qqq or $\overline{qqq}$) are called baryons.

1.1.1 Quantum chromodynamics

The interaction between quarks and gluons is described by quantum chromodynamics (QCD). The QCD is similar to quantum electrodynamics (QED) describing interaction between electrons and photons. Contrary to electrons in the QED, quarks in the QCD have three different charges called color (R - red, G - green and B - blue). The gluons carry 8 charges, i.e. 3×3 different combinations of colors and anticolors (e.g. $R\overline{R}$, $R\overline{B}$ etc.) where one combination is excluded due to the unitarity restriction. This intrinsic charge allows direct interaction of gluons between each other contrary to the photons in the QED which need intermediate electrons to interact [6]. The QCD can be defined by Lagrangian density as

$$\mathcal{L} = -\frac{1}{4}F_{\mu\nu}^{\alpha}F_{\alpha}^{\mu\nu} - \sum_{f}\overline{\psi}_{f}^{\alpha}\left(i\gamma^{\mu}\partial_{\mu} + m_{f} - g\gamma^{\mu}A_{\mu}\right)_{\alpha\beta}\psi_{f}^{\beta}, \tag{1.1}$$

where f denotes different flavor, m_f is the mass of the related quark, ψ_f^{α} is the quark spinor field with color $\alpha \in \{1, 2, 3\}$ and

$$F_{\mu\nu}^{\alpha} = (\partial_{\mu}A_{\nu}^{a} - \partial_{\nu}A_{\mu}^{a} - gf_{bc}^{a}A_{\mu}^{b}A_{\nu}^{c}), \tag{1.2}$$

where A_{μ}^{a} is the gluon field with color $a \in \{1, 2, ..., 8\}$ and f_{bc}^{a} is the structure function [15]. One derives the partition function $Z(T, V)$ as a function of temperature T and volume V expressed as a functional path integral

$$Z(T, V) = \int \mathrm{d}A\mathrm{d}\psi\mathrm{d}\overline{\psi}\exp\left(-\int_{V}\mathrm{d}^{3}x\int_{0}^{\frac{1}{T}}\mathrm{d}\tau\mathcal{L}(A, \psi, \overline{\psi})\right). \tag{1.3}$$

Once the partition function is known, the thermodynamic observables, such as energy density ϵ and pressure P are as follows

$$\epsilon = \frac{T^{2}}{V}\left(\frac{\partial \ln Z}{\partial T}\right)_{V}, \tag{1.4}$$

$$P = T\left(\frac{\partial \ln Z}{\partial V}\right)_T. \tag{1.5}$$

The QCD model is a success, however, it has one disadvantage - its calculations cannot be performed in the same manner as were developed for the QED. This is caused by the relatively high value of the QCD coupling constant α_s which is of the order of one, while the electromagnetic coupling constant is:

$$\alpha = \frac{e^2}{4\pi\varepsilon_0\hbar c} \doteq \frac{1}{137}, \tag{1.6}$$

where ε_0 is the vacuum permittivity, $\hbar$ is the reduced Planck constant, c is the speed of light in vacuum. Although α_s is called constant, it depends on the transfered momentum Q^2 in the interaction as follows

$$\alpha_s(Q^2) \propto \frac{1}{\ln\left(\frac{Q^2}{\Lambda^2}\right)}, \tag{1.7}$$

where $\Lambda \approx 200$ MeV [16] is a constant defining the scale [17]. Hence, the α_s becomes small at large Q^2 and the perturbation theory pQCD applied in QED is applicable. On the other hand, pQCD cannot be performed for low Q^2 and this energy region is labeled as non-perturbative QCD [15]. In 1974, its numerical calculations were introduced by means of the lattice approach by Kenneth Wilson [17]. This method is called lattice QCD. The quark and gluon field configuration is generated and weighted by the Boltzmann factor

$$\frac{\exp(-S)}{Z} = \frac{\exp\left(-\int d^4x \mathcal{L}(x)\right)}{Z}, \tag{1.8}$$

where S is the action. The integration is performed numerically considering 4-dimensional lattice (t, x, y, z). The precision of the computation is proportional to the number of points on the lattice but at the cost of a longer calculation time [17].

As has been already noted, the quarks cannot occur alone which is another typical feature of QCD. Let us consider a static quark pair $q\bar{q}$ connected by a gluonic flux tube which can be called a string. If one would want to separate the quarks apart, at the certain distance, the string will break, creating a new $q\bar{q}$ pair, see Fig. 1.2.
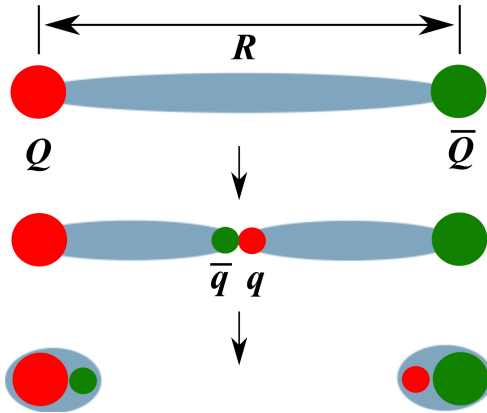

Figure 1.2: The breaking of the QCD string between a static quark Q and an antiquark $\overline{Q}$ into a new quark pair q and $\bar{q}$ [18].

In a case of static $q\bar{q}$ pair at $T = 0$ K, their free energy is described by the Cornell potential

$$V_{\text{cor}}(r) = \sigma r - \frac{\alpha}{r}, \qquad (1.9)$$

where r is the distance between the quarks, $\sigma = 1$ GeV/fm is the string tension and $\alpha = \pi/12$ (predicted by the string theory) is called the color coupling [6]. The first term represents the string free energy linearly increasing with the increasing distance and the second one is related to the Coulomb interaction between the static charges. The fact that quarks cannot be separated and observed free is called confinement. However, quarks at short distances behave as free particles. This feature is called asymptotic freedom [17].
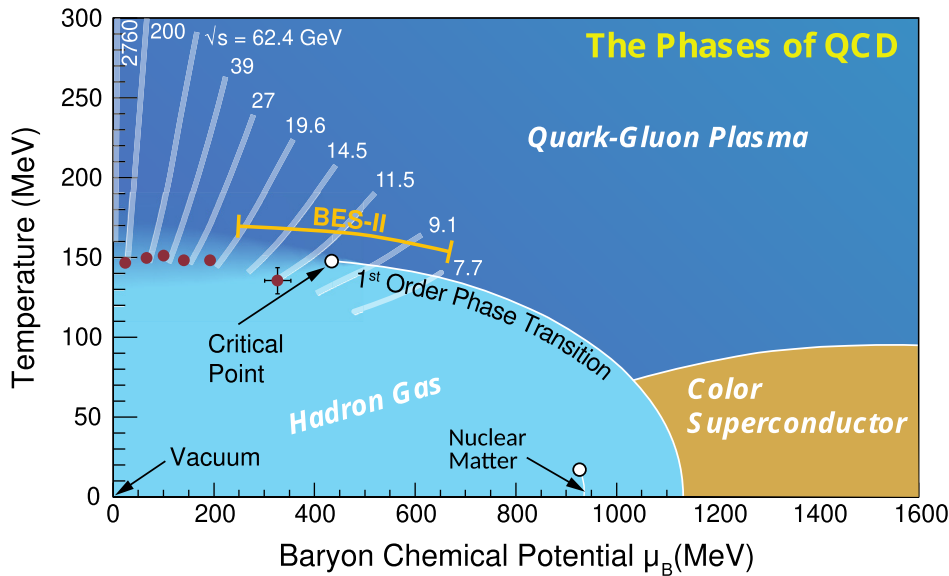
1.2   Quark-gluon plasma

Figure 1.3: The QCD phase diagram as function of temperature T and baryon chemical potential μ_B [19].

The most interesting result of QCD is the prediction of a new state of matter - the Quark-Gluon Plasma (QGP) where partons (quarks and gluons) are asymptotically free and which should exist at high temperatures T and/or high baryon chemical potential μ_B. In 2000, the first evidence of such state was observed at CERN [20]. Later, the existence of the QGP was independently confirmed by RHIC at BNL [21]. The QCD phase diagram, see Fig. 1.3, describes three phases of nuclear matter: hadron gas, quark-gluon plasma, and color superconductor with respect to temperature T and baryon chemical potential μ_B. Between the hadron gas and QGP phase, the two different phase transitions can be observed. The transition from the hadron gas to the QGP can be perceived as the melting of hadrons. For the lower μ_B values, the transition is expected to be a crossover. For $\mu_B = 0$, the lattice QCD calculations

predict the phase transition at $T = (156.5 \pm 1.5)$ MeV [22]. On the other hand, the first order phase transition is expected for the higher μ_B.

The point between the crossover and the first order phase transition is called a critical point. The search for this point is one of the goals of the BES program at RHIC [23]. The approximate sketch of cooling droplets of QGP crossing the phase transition for a given energy of the collision including the BES-II program (second phase of the BES program) at RHIC are depicted in Fig. 1.3 [19].

Due to the requirement on the high temperature and/or high pressure, the QGP is expected to be found in three places [1]:

- The beginning of the Universe (10^{-5} s after the Big Bang).

- In superdense stars, for instance neutron and quark stars [1].

- In relativistic heavy-ion collisions which are sometimes referred to as "Little Bang".

1.3 Heavy-ion collisions

After the prediction of the existence of the QGP, it was believed that relativistic heavy-ion collisions could create a similar environment to the Early universe. Therefore facilities such as Brookhaven National Laboratory in the USA and CERN in Switzerland launched the program of accelerating heavy nuclei at high energies.

In Fig. 1.4 on the left, a sketch of the heavy-ion collision in the center-of-mass (CMS) frame is depicted. The nuclei resemble thin disc (pancakes) because they are Lorentz-contracted due to their high velocity. The highest energy density is in the center of the collision where the creation of the QGP is expected. In short, the expansion of the QGP cools down the medium until it reaches the final freeze-out temperature where the hadrons are formed and can be measured by surrounding detectors [24].

In Fig. 1.4 on the right, the space-time evolution in the light cone variables space z and time t is shown. Before the collision at time $t = 0$, the nuclei flying almost at the speed of light are moving along the light cone. Then, the collision occurs at position $z = 0$ and $t = 0$. Whereas the nuclear fragments of the collisions continue along the light cone, most of the matter is in the central region [17]. The first stage of the matter lasting a short time $\tau < 1$ fm/c is called pre-equilibrium [25]. There the partons of the colliding nuclei interact and produce another partons [6]. In the next stage, the QGP is created in case the energy density and pressure are sufficiently high. Then, the QGP expands and cools down. It is expected that in the case of the first-order phase transition, the QGP is converted into a mixed-phase containing hadrons and the QGP at the temperature of the phase transition. On the other hand, the mixed-phase is not expected for energies where the matter undergoes a crossover transition [15], [26]. The moment at which the inelastic collisions in the medium cease is called chemical freeze-out. In the next stage, the hadrons interact with each

other via elastic collisions. Finally, the last stage where the elastic collisions cease is called thermal freeze-out. The free hadrons fly out from the medium and can be measured in various experiments [26].
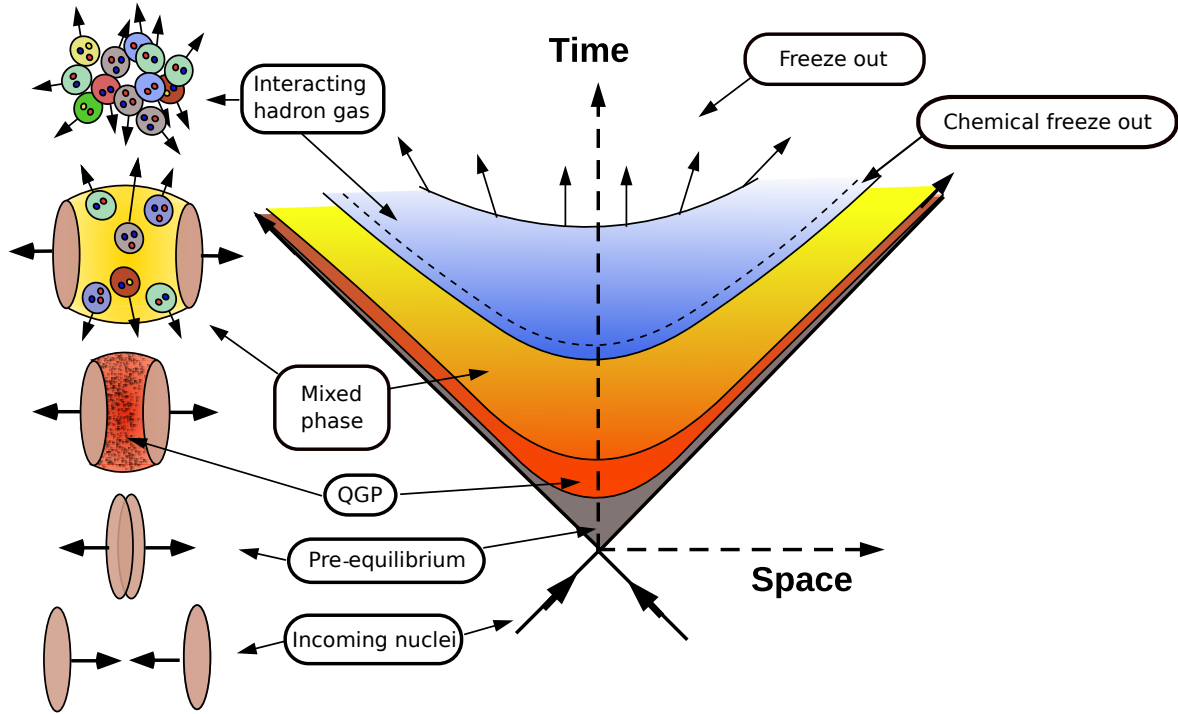
Figure 1.4: Space-time evolution of a heavy-ion collision [27], modified.

1.3.1 Collision parameters

The Heavy-Ion (HI) collisions can differ with respect to the centrality of the collision. Therefore, the impact parameter $\vec{b}$ connecting the centers of the colliding nuclei is introduced, cf. Fig. 1.5.
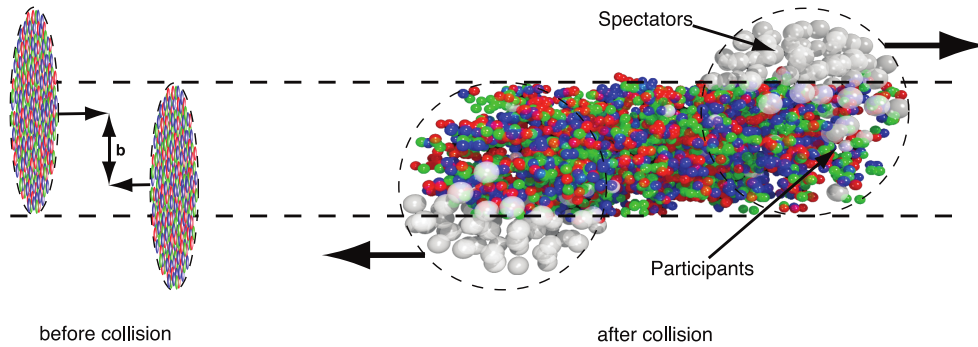
Figure 1.5: Left: Two nuclei before collision including the impact parameter $\vec{b}$. Right: Two nuclei after collision where the spectators and participants are described [28].

The centrality of the collision C for the given impact parameter b is defined as

$$C = \frac{1}{\sigma_{\mathrm{inel}}} \int_0^b P_{\mathrm{inel}}(b') 2\pi b' \mathrm{d}b', \tag{1.10}$$

where σ_{inel} is the inelastic nucleus-nucleus cross-section and $P_{\mathrm{inel}}(b')$ is the probability of the inelastic collision at impact parameter b'. The collisions with C close to 0 and 1 are called central and peripheral collisions, respectively. In the case of the peripheral collisions, the nucleons can be divided into participants (undergo collision) and spectators (do not collide). In experiments, the direct measurement of the impact parameter is not feasible. Therefore, a single variable n is measured instead of b. The definitions of the n are various, however, it can be perceived as a number of produced charged particles in chosen pseudorapidity window. Using the Glauber model simulation, it is then possible to estimate the centrality range for the measured n values [17], [29].

In order to describe the energy of the collision, Mandelstam variable s for a collision of particles 1 and 2 is introduced as follow

$$s = (p_1 + p_2)^2, \tag{1.11}$$

where p is the four-momentum of the related particle. The Mandelstam variable s is Lorentz-invariant. Owing to this property, the colliding particles can be boosted to the center of mass (CMS) frame where the sum of momenta $\vec{p}_1$ and $\vec{p}_2$ is zero. Hence, the s value can be written as[1]

$$s = (E_1 + E_2; \overbrace{\vec{p}_1 + \vec{p}_2}^{=\vec{0}})^2 = (E_1 + E_2)^2. \tag{1.12}$$

Thus, the energy of the collision in the CMS is expressed as $\sqrt{s}$.

1.3.2 Parameters of produced particles

The new particles produced in HI collisions fly out from the interaction point to detectors measuring their properties. One of them is rapidity y defined as

$$y = \frac{1}{2} \ln\left(\frac{E + p_{\mathrm{L}}}{E - p_{\mathrm{L}}}\right) = \mathrm{artanh}\left(\frac{p_{\mathrm{L}}}{E}\right), \tag{1.13}$$

where E is the energy and p_{L} is the longitudinal momentum (i.e. momentum in the beam axis direction). The rapidity y of particles flying perpendicularly to the beam axis is zero and it increases with the increasing p_{L}.

More intuitive variable than the rapidity is so-called pseudorapidity η that is related to the polar angle θ with respect to the beam axis. The pseudorapidity is defined as

$$\eta = \frac{1}{2} \ln\left(\frac{|\vec{p}| + p_{\mathrm{L}}}{|\vec{p}| - p_{\mathrm{L}}}\right) = -\ln\tan\left(\frac{\theta}{2}\right). \tag{1.14}$$

---

[1]In this thesis, natural units are used, i.e. $c = \hbar = k_{\mathrm{B}} = 1$. In the opposite case, the four-momentum would be $p = \left(\frac{E}{c}; \vec{p}\right)$.
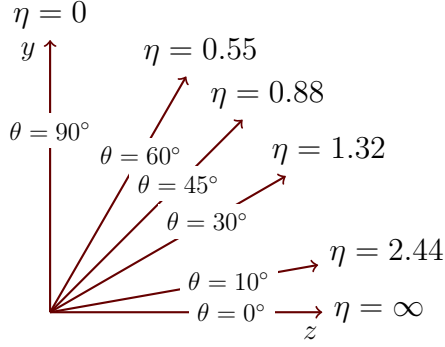
Figure 1.6: The pseudorapidity η and the related polar angles θ with respect to the beam axis z.

If one considers that $m \ll |\vec{p}|$ than $E \approx |\vec{p}|$, than $y \approx \eta$ as can be seen from Eq. (1.13) and Eq. (1.14). Examples of a chosen polar angle θ and the related pseudorapidity is shown in Fig. 1.6. The determination of the pseudorapidity η is easier than the rapidity y because only the angle θ is required.

Among the observables indicating the presence of the QGP in HI collisions can be included the nuclear modification factor R_{AA} which is defined as a ratio of number of produced particles in HI and p-p collisions normalized by the mean number of binary nucleon-nucleon collisions $\langle N_{\mathrm{coll}} \rangle$:

$$R_{\mathrm{AA}}(p_{\mathrm{T}}) = \frac{1}{\langle N_{\mathrm{coll}} \rangle} \frac{\frac{\mathrm{d}N_{\mathrm{AA}}}{\mathrm{d}p_{\mathrm{T}}}(p_{\mathrm{T}})}{\frac{\mathrm{d}N_{\mathrm{pp}}}{\mathrm{d}p_{\mathrm{T}}}(p_{\mathrm{T}})}. \tag{1.15}$$
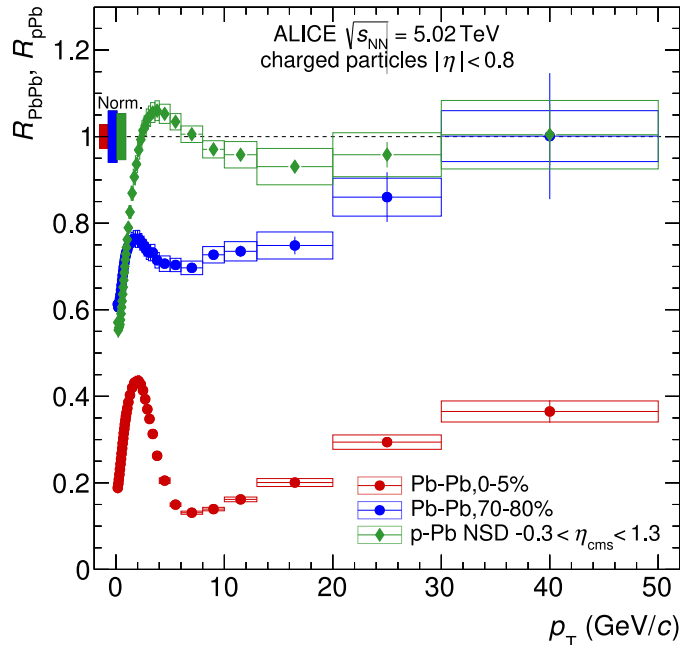
Figure 1.7: Nuclear modification factor R_{AA} as a function of the transverse momentum p_{T} for Pb-Pb and p-Pb collisions at $\sqrt{s_{\mathrm{NN}}} = 5.02$ TeV in central $(0 - 5\%)$ and peripheral $(70 - 80\%)$ collisions measured by ALICE [30].

22

If the medium and other nuclear effects are not presented, it is expected that $R_{\mathrm{AA}} = 1$. In central collisions at sufficiently high energy, QGP should be created and therefore the created particles have to go through the medium where they lose energy. Hence, one should observe suppression of p_{T} spectra, i.e. $R_{\mathrm{AA}} < 1$. In non-central collision, much smaller medium is created. Thus the suppression is weaker than in the previous case, see Fig. 1.7.

1.3.3 Flow

In high-energy HI collisions, a large number of emitted particles is observed. Hence, one could expect some multiparticle correlation, called flow. The collective phenomena in collisions are fairly successfully described by hydrodynamical models.
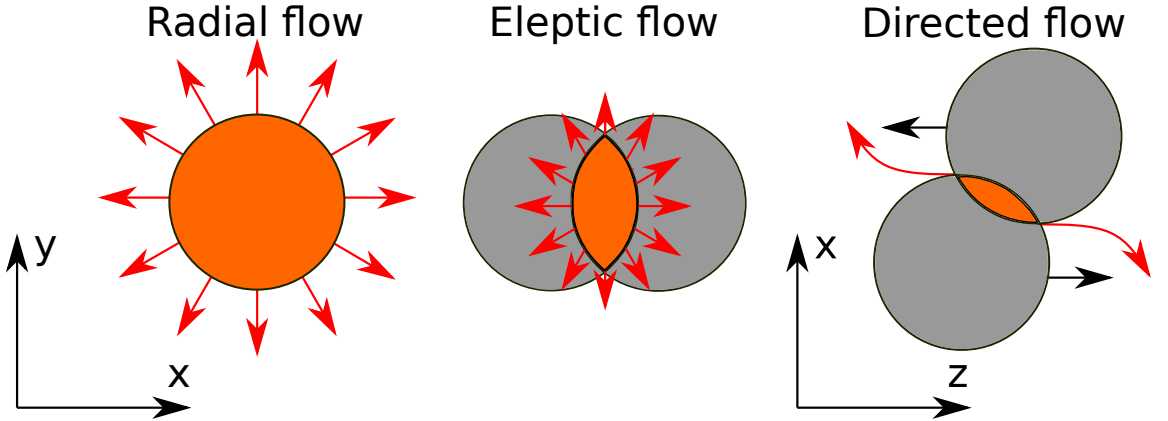

Figure 1.8: Different types of flow phenomena in HI collision where z is the beam axis.

The types of flow can be divided into 3 main types, see Fig. 1.8. In central collisions of spherical symmetric nuclei, the particle emission is uniform in all directions in the transverse plane ($x - y$ plane). This type of isotropic flow is called radial flow. The anisotropic flow can be observed in a non-central collision. In order to describe the anisotropy, the particle distribution in the transverse plane is expanded into Fourier series as

$$E\frac{\mathrm{d}^3N}{\mathrm{d}p^3} = \frac{1}{2\pi}\frac{\mathrm{d}^2N}{p_{\mathrm{T}}\mathrm{d}p_{\mathrm{T}}\mathrm{d}y}\left\{1 + 2\sum_{n=1}^{+\infty}v_n(p_{\mathrm{T}}, y)\cos\left[n(\phi - \Psi_{\mathrm{RP}})\right]\right\}, \qquad (1.16)$$

where $p_{\mathrm{T}} = \sqrt{p_x^2 + p_y^2}$ is the transverse momentum, $v_n(p_{\mathrm{T}}, y)$ is the flow coefficients, ϕ is the azimuthal angle and Ψ_{RP} is the reaction plane (RP) which is defined by two vectors (beam axis z and impact parameter $\vec{b}$) as is shown in Fig. 1.9. The flow coefficients can be calculated as

$$v_n(p_{\mathrm{T}}, y) = \langle\cos[n(\phi - \Psi_{\mathrm{RP}})]\rangle. \qquad (1.17)$$

In the Fourier series in Eq. (1.16), the sinus terms are not presented because of the reflection symmetry with respect to the RP. For the isotropic production, all of the

flow coefficients v_n are zero. The first flow coefficient v_1 is related to the directed flow, see Fig. 1.8. This type of flow is mostly formed at the beginning of the collision being influenced by the early pressure gradients of the matter [31]. Regarding the formation of QGP should be noted that the v_1 is sensitive to QGP creation because in the case of the mixed-phase of QGP, the pressure gradients may disappear, thereby the v_1 is significantly reduced [17], [32].
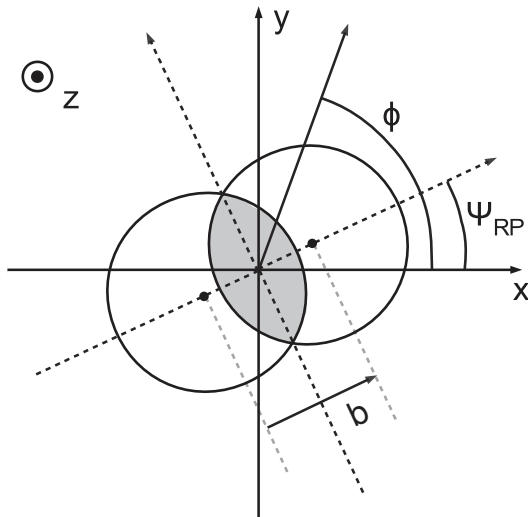
Figure 1.9: A scheme of the angle of the reaction plane Ψ_{RP} in a non-central HI collision where $\vec{b}$ is the impact parameter and ϕ is the azimuthal angle of a produced particle [33].
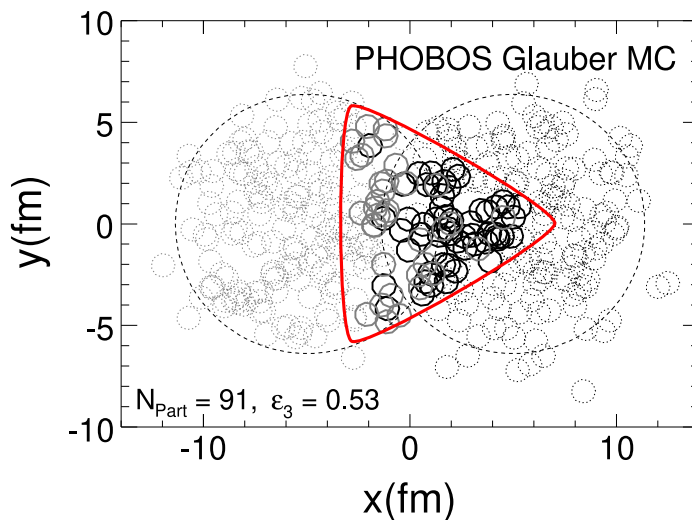
Figure 1.10: Nucleon distribution on the transverse plane for Au-Au collision at $\sqrt{s_{NN}} = 200$ GeV from Glauber Monte Carlo where ε_3 is the participant eccentricity, N_{Part} is the number of participants visualized as solid circles (spectators as dotted circles), and the red triangle shows the triangular shape of medium, modified [5].

The second flow coefficient v_2 is related to the elliptic flow, see Fig. 1.8, and it describes the ellipticity of the angular distribution. The v_2 caused by the initial

ellipsoidal overlap of the colliding nuclei is the strongest flow pattern which centrality and p_T dependencies are successfully described by hydrodynamical calculations [5].

The higher flow coefficient v_3, known as the triangular flow, almost does not depend on the centrality of the collision contrary to the elliptical flow [34], [35]. The triangular flow origins from the fluctuation of the energy-density in the overlap region as can be seen in Fig. 1.10.

Chapter 2

STAR experiment

In this chapter, the STAR experiment at the RHIC collider at Brookhaven National Laboratory, including the future plan of EIC collider, is discussed.

2.1 RHIC

The Relativistic Heavy Ion Collider (RHIC) is a scientific research facility at Brookhaven National Laboratory (BNL) on Long Island in the USA. The year 1983 can be considered the beginning of this collider when a task to prepare all required parameters of the new collider was assigned during the Aurora meeting.
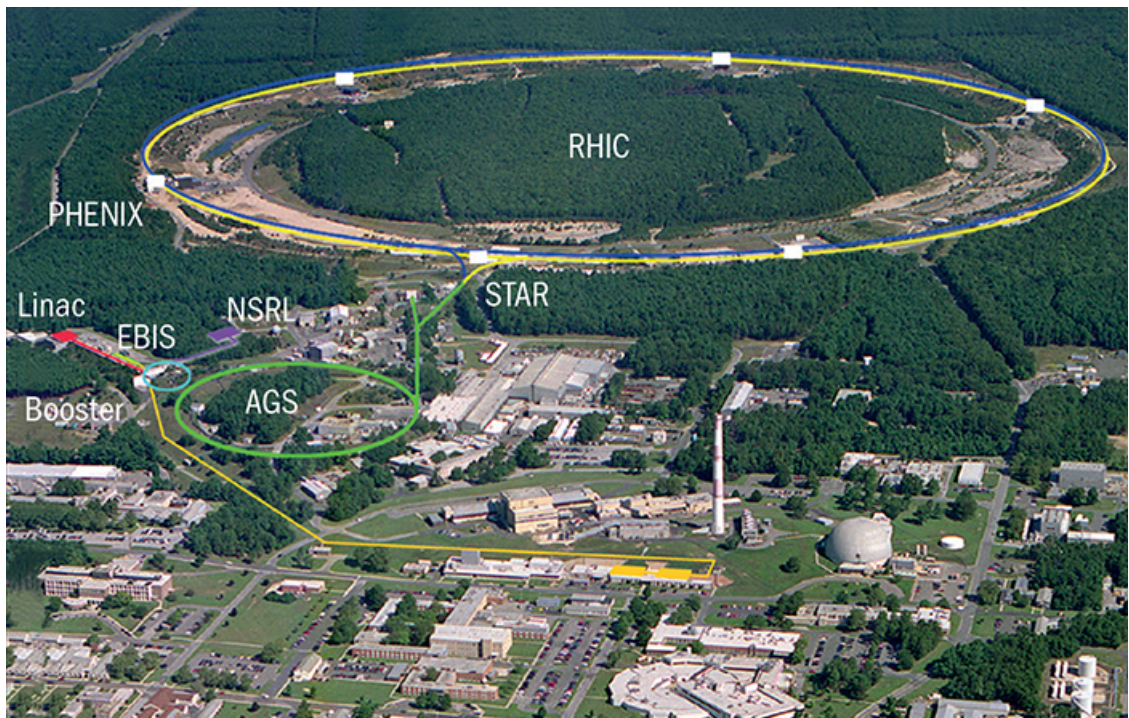
Figure 2.1: An aerial photograph of the RHIC with highlighted accelerators and positions of STAR and PHENIX experiments [36].

The building of the RHIC started from tunnels (circle with a circumference of 3.8 km [37]) used in the previous project called Colliding Beam Accelerator (CBA) which had been formerly called ISABELLE [38]. As one of RHIC's first aims was to achieve a small net baryon density [39].

EBIS		
Au^{32+} ⇓	17 keV/u	3.4×10^9 ions
RFQ		90%
Au^{32+} ⇓	300 keV/u	3.0×10^9 ions
Linac		90%
Au^{32+} ⇓	2 MeV/u	2.7×10^9 ions
BOOSTER		85%
Au^{32+} ⇓	70 MeV/u	2.3×10^9 ions
▬▬▬ STRIPPER FOIL		60%
Au^{77+} ⇓	70 MeV/u	1.4×10^9 ions
AGS		90%
Au^{77+} ⇓	9 GeV/u	1.2×10^9 ions
▬▬▬ STRIPPER FOIL		100%
Au^{79+} ⇓	9 GeV/u	1.2×10^9 ions
RHIC		

Figure 2.2: A scheme of acceleration process of Au nucleus including the number of ions per pulse and efficiencies at each stage [40].

The RHIC consists of two (blue and yellow) storage rings, see Fig. 2.1. The rings cross at overall 6 interaction points (IPs) [41]. In 2000, there were a total of 4 experiments: STAR (at 6 o'clock position) that is currently still operating, PHENIX (at 8 o'clock

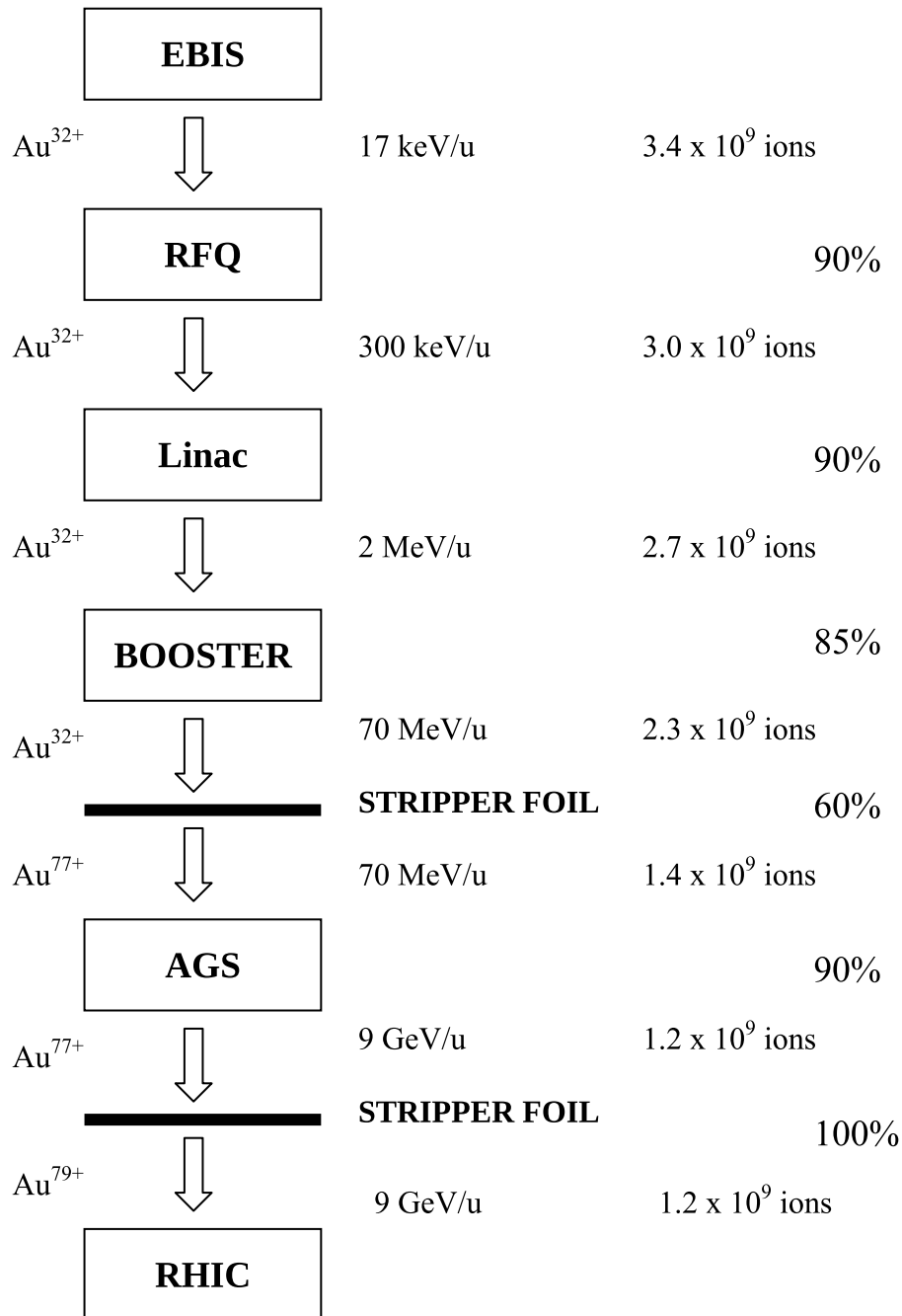position) that was stopped in 2016, and two smaller detectors PHOBOS (at 10 o'clock position) and BRAHMS (at 2 o'clock position) that finished their operations at 2005. A brand new sPHENIX detector is currently under construction. This new detector will record data for systems p-p, p-Au, and Au-Au at energy $\sqrt{s_{\mathrm{NN}}} = 200$ GeV and its running plan is for three years (2023-2025) with an opportunity to continue next two years until 2027 [42], [43], [44].

The RHIC is a long chain complex of different accelerators which lead to the storage rings (SRs), as can be seen in Fig. 2.2.

The source of ions is Electron Beam Ion Source (EBIS) accelerator which replaced the older Tandem Van de Graaf preinjectors as the source. Contrary to the old one, EBIS is able to switch rapidly the species of injected ions and provides also noble gas ions required by NASA [45].
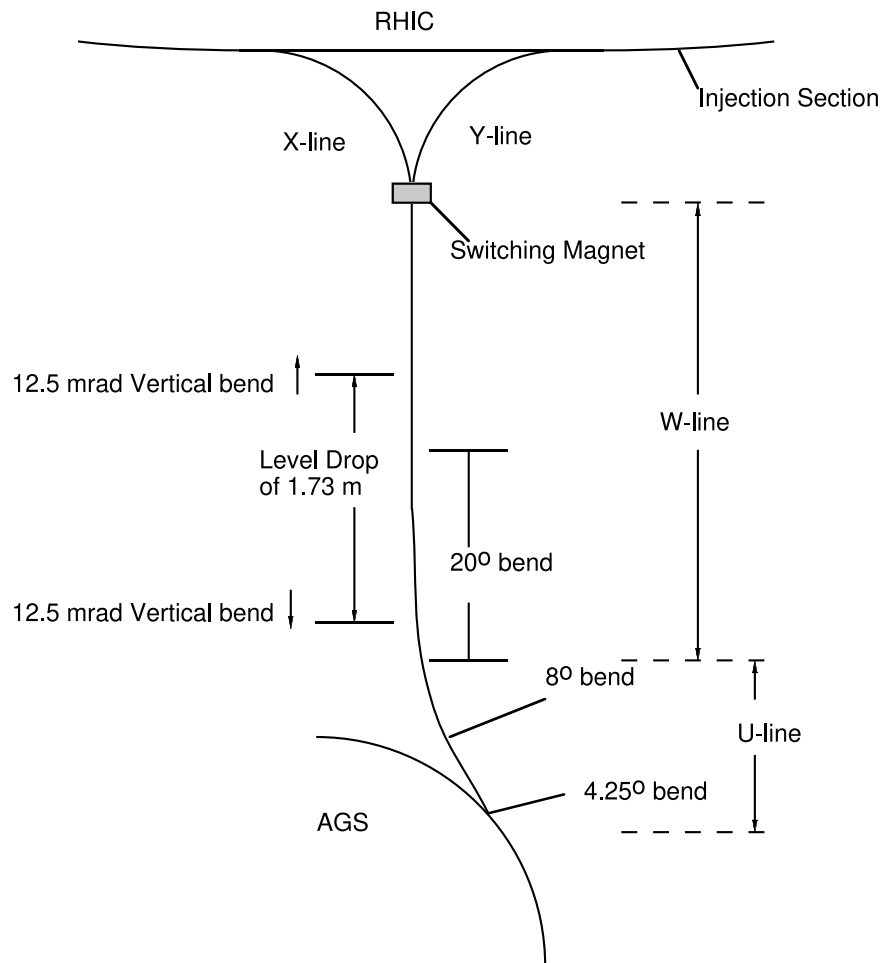

Figure 2.3: A schematic of the RHIC transfer line [46].

The next stage is Radiofrequency Quadrupole (RFQ) accelerator accepting low energy charged ions from EBIS. These ions or bunches are then accelerated with high efficiency and low change of beam emittance. The operation frequency of this device is 100.625 MHz [47].

Then the ions proceed to Interdigital H-type (IH) Linac with KONUS beam dynamics [48]. After that they continue into Booster synchrotron which is used as a preaccelerator for 4 times larger Alternating Gradient Synchrotron (AGS) which is known because of 3 Nobel prizes from results which were performed there [36].

The last step for the beam is a transport from AGS into the RHIC's storage rings via ATR (AGS to RHIC) line, see Fig. 2.3. This transfer link has four main goals: match the trajectory of the beam, tranverse focusing, dispersion, and minimize losses of energy. The first part of ATR (so-called U-line) extracts accelerated particles from the AGS at its beginning. The rest of the U-line bends the beam in two sections including dipole and quadrupole magnets.

The second part (W-line) consists of a couple of magnets to bend the trajectory and lowers the beam elevation by 1.7 m by means of two vertical dipoles (pitching magnets) [49].

At the end of W-line, there is ATR split into X-line and Y-line which leads to the blue SR (clockwise motion) and yellow SR (anticlockwise motion) [50], [51].

The RHIC provides possibility of colliding a wide range of heavy-ions (such as Cu, Au or U nuclei including different nuclei combination p-Au, d-Au or ^{3}He-Au). Furthermore, the collided protons can be polarized [52], [53]. The reachable collision energies $\sqrt{s_{NN}}$ for Au-Au collisions are between 7.7 and 200 GeV and up to 510 GeV in the case of p-p collisions. A brief summary of different energies and different species is shown in Fig. 2.4.
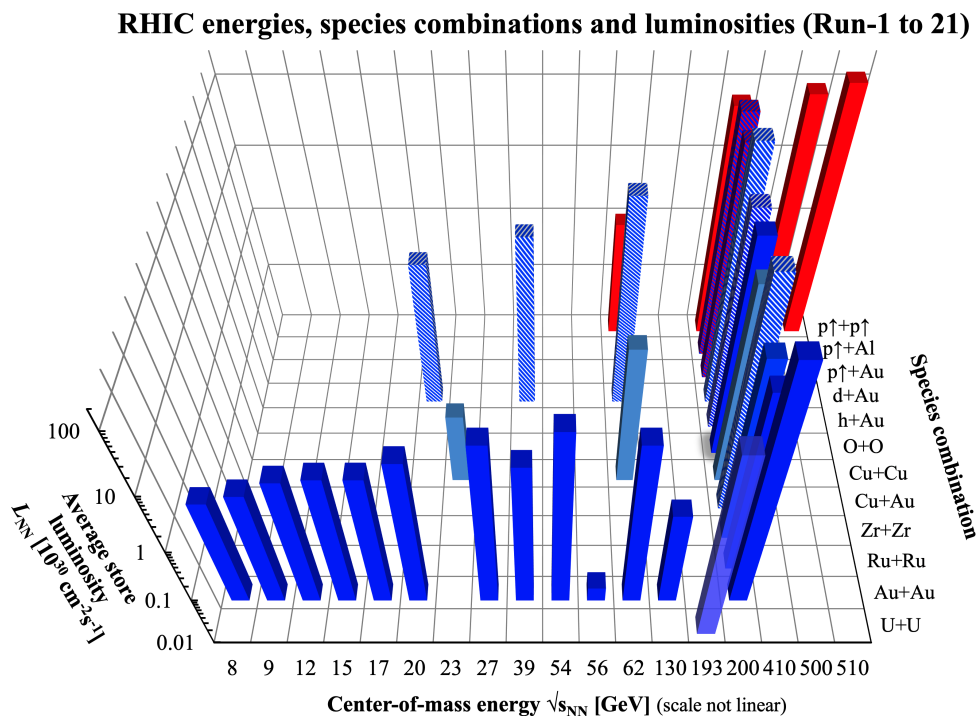

Figure 2.4: Visualization of RUN-1 to 21 at RHIC including chosen energy of the collision $\sqrt{s_{NN}}$, nuclei species and average store luminosity L_{NN} [54].

30

2.2 STAR

The STAR experiment (an acronym for Solenoidal Tracker At RHIC) was designed for observation of strongly interacting matter QGP. The STAR detector had consisted of 18 subsystems (some subdetectors are shown in Fig. 2.5), before the new upgrades for the second phase of the Beam Energy Scan program (BES-II) which took place between 2019 and 2022 [55].
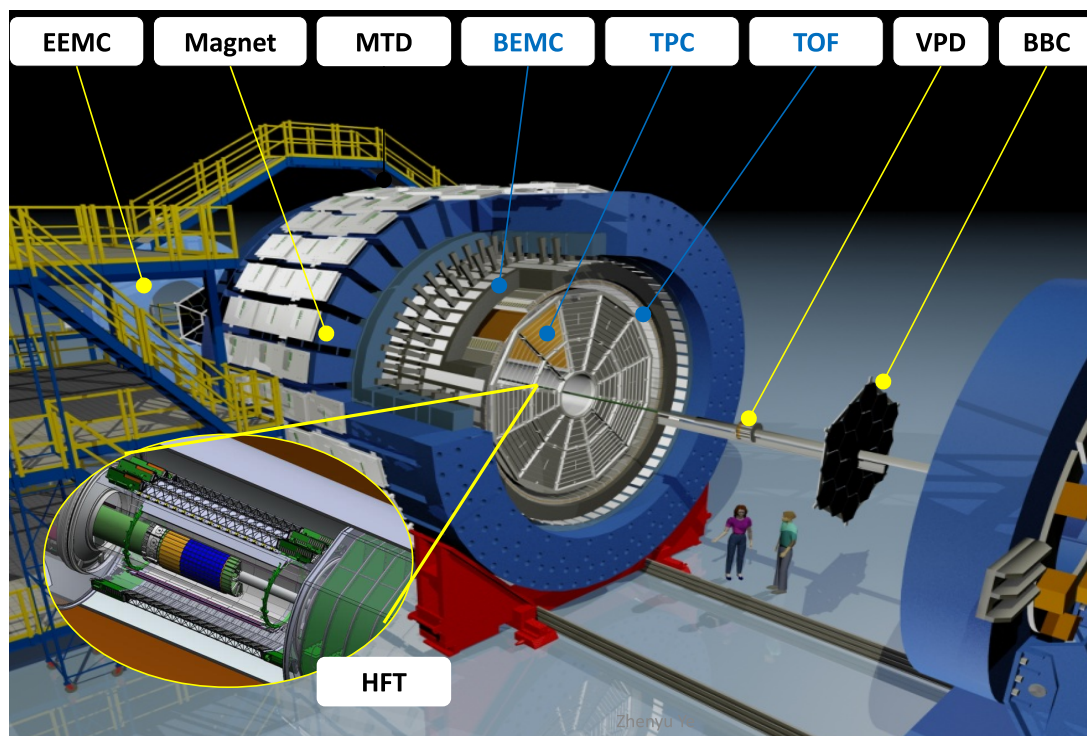
Figure 2.5: The STAR detector layout before the upgrade [56].

The STAR subdetectors include:

- The **Time Projection Chamber (TPC)** located in the center of the STAR. The shape of the TPC is a cylinder with an outer diameter of the drift volume of 4 m and a length of 4.2 m. It covers pseudorapidity region $|\eta| < 1.8$. The purpose of the TPC is to reconstruct tracks, measure momenta and identify species of the passing particles. In order to perform the Particle IDentification (PID), information about the particle's ionization energy loss $(\mathrm{d}E/\mathrm{d}x)$ in the TPC gas is required [57].

- The **Time of Flight (TOF)** detector installed in the year 2003 is based on the Multi-gap Resistive Plate Chamber (MRPC) technology. It is positioned 220 cm from the interaction point. Its psuedorapidity coverage is $|\eta| < 1$. The time resolution of the TOF detector is less than 100 ps. Together with the TPC detector, they can be used for the separation of specific particle species. For example, the TPC detector itself is unable to reasonably distinguish between

pions and protons and the TOF detector itself cannot distinguish between pions and protons at $2.0 < p_{\mathrm{T}} < 4.0$ GeV/c [58], [59].

- The **Barrel Electromagnetic Calorimeter (BEMC)** is installed around the TPC and TOF detectors. It measures particles in pseudorapidity $|\eta| < 1.0$. The BEMC detector is composed of 120 separated calorimeter modules made for the electromagnetic energy measurement. As it is an electromagnetic calorimeter, it is able to identify electrons and detect high-p_{T} particles (such as jets, leading hadrons or direct photons) [60].

- The **solenoidal magnet** producing a uniform magnetic field of 0.5 T inside the cylindrical volume is posited along the beam direction [61]. The TPC, TOF, and BEMC detectors are located inside the magnet as is shown in Fig. 2.5.

- The **Beam-Beam Counters (BBC)** consist of scintillators posited perpendicular to the beam pipe on the north and the south pole tips of the solenoidal magnet. Both parts of the annuli shape are installed 3.75 m from the STAR detector center. The pseudorapidity coverage of the BBC is $3.4 < |\eta| < 5.0$ [62].

- The **Vertex Position Detector (VPD)**, currently pseudo Vertex Position Detector (pVPD), is integrated into the trigger system of the STAR detector. The purpose of VPD is the localization of the collision vertex. Like BBC, the VPD consists of two detectors on the west and the east side of the STAR detector installed immediately outside the beam pipe [63], [64].
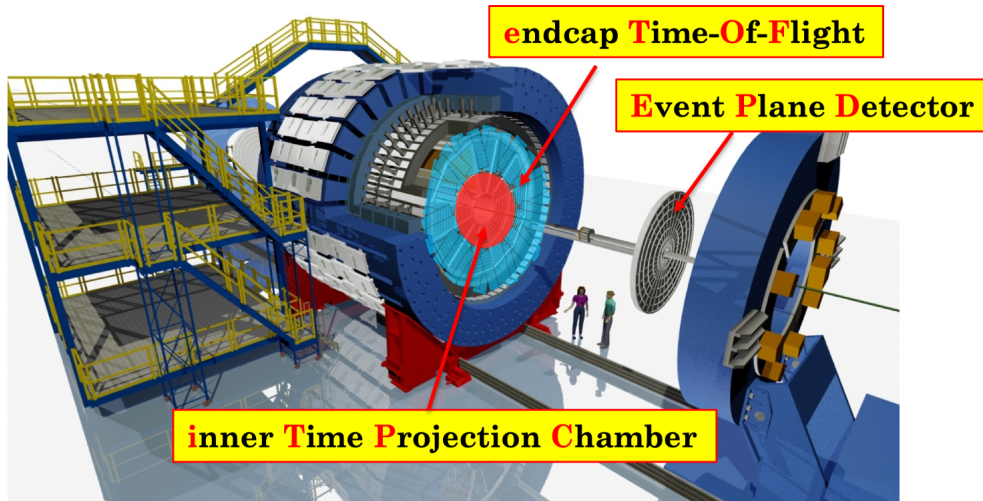
Figure 2.6: The STAR detector layout after the installation of new components iTPC, EPD and eTOF for the RHIC BES-II program [65].

The first stage of the BES program (BES-I) that ran from 2010 to 2014 [66] was aimed at the exploration of the QCD phase diagram, in particular search for the existence and position of the critical point and study of the phase transition between hadron gas and QGP [67]. In this program, the collisions were performed for energies

between 7.7 GeV and 19.6 GeV. Nevertheless, the sensitivity of some measurements (such as the net proton kurtosis, the directed flow, or the production of dileptons [65]) was insufficient to draw precise physics conclusions. For this purpose, the STAR detector underwent a few upgrades, i.e. installation of new subdetectors: inner Time Projection Chamber (iTPC), endcap Time of flight detector (eTOF), and Event Plane Detector (EPD) so that the measurement in the next stage (BES-II) would be more accurate. In particular, the iTPC provides better energy loss dE/dx and p_T resolution, a lower p_T threshold (60 MeV/c) and a wider pseudorapidity coverage $|\eta| < 1.5$. The eTOF located on one side of the STAR detector improves the PID coverage to $|\eta| < 1.6$ in the fixed-target mode [68]. The EPD will be described later.

Beam Energy	$\sqrt{s_{NN}}$ (GeV)	Expected Duration	Actual Duration	Proposed Events	Recorded Events	Year
3.85	3.0	4 days	3.5 days	100 M	258 M	2018
3.85	3.0	3 days	3.3 days	300 M	307 M	**2021**
3.85	3.0	3 weeks	TBD	2 B	TBD	**2021**
4.59	3.2	2 days	46 hours	200 M	200.6 M	2019
5.75	3.5	1 day	23 hours	100 M	115.6 M	2020
7.3	3.9	0.5 days	12 hours	50 M	52.7 M	2019
7.3	3.9	1 day	29 hours	100 M	117 M	2020
9.8	4.5	1 day	31 hours	100 M	108 M	2020
13.5	5.2	1 days	21 hours	100 M	103 M	2020
19.5	6.2	1 days	22 hours	100 M	118 M	2020
26.5	7.2	parasitic	2 days	none	155 M	2018
26.5	7.2	parasitic	3.5 days	none	317 M	2020
26.5	7.2	parasitic	TBD	none	TBD	2021
31.2	7.7	0.5 days	11.5 hours	50 M	50.6 M	2019
31.2	7.7	1 day	26 hours	100 M	112 M	2020
44.5	9.1	0.5 days	12 hours	50 M	53.9 M	**2021**
70	11.5	0.5 days	12 hours	50 M	51.7 M	**2021**
100	13.7	0.5 days	10 hours	50 M	50.7 M	**2021**

Table 2.1: Summary of BES-II and FXT programs for Au-Au beam energy $\sqrt{s_{NN}}$ with event statistics [69].

The collected data are gathered in Tab. 2.1. It can be seen that the BES-II has been successful. Currently, the main priority is to complete the BES-II program and start with Cold QCD forward physics program. The future plan is a study of the microstructure of QGP by means of soft and hard probes in 2023-2025 [69].

The fixed-targed mode (FXT) at STAR is performed to reach lower collision energies (up to $\sqrt{s_{NN}} = 3$ GeV). The FXT experiment is a part of BES-II. The fixed target made of gold foil of a width of 1 mm is posited 2.05 m west of the STAR detector center. To obtain sufficient statistics for the BES-II program, just a few days of running (1-2 days) is required [69].

2.2.1   Event plane detector

This detector is crucial for analysis performed in this thesis therefore it is introduced in more detail.

The Event Plane Detector (EPD) installed in 2018 measures passing particles from HI collisions in polar angle range $0.7° < \theta < 13.5°$ (corresponds to $2.14 < |\eta| < 5.09$). The purpose of the EPD is reconstruction of the event plane, see Chapter 3.6 for more details. Similarly to BBC, the EPD consists of two parts (west and east). Both of them are segmented into 12 supersectors. The supersector consists of 31 tiles as is depicted in Fig. 2.7. A total of 31 optical fibers in a bundle connect the supersector to a silicon photomultiplier (SiPM) where the light signal is transformed into an electrical signal which is additionally amplified and processed in the STAR digitizing and acquisition system [70].

In addition to the division into tiles, the EPD can be segmented into 16 rings. One ring represents a group of tiles lying at the same distance from the beam pipe. This segmentation is important because of the signal corrections as will be seen later.
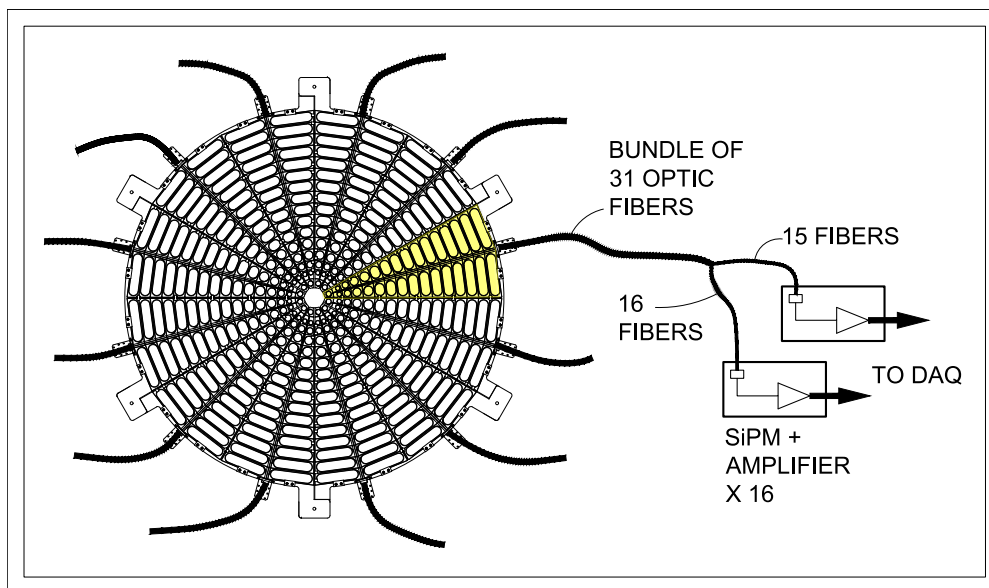
Figure 2.7: The layout of the EPD wheel [70].

The magnetic field of 0.5 T does not significantly affect the reconstructed event plane. Therefore, the sufficient information needed for the reconstruction is a single hit of each charged particle passing through the EPD wherein the signal is produced in the plastic scintillator planes. The significant peaks in the measured signal distributions correspond to each minimally ionizing particle (MIPs) traversing the EPD [70].

2.3 EIC

The construction of the new Electron-Ion Collider (EIC) is planned at BNL in the year 2025 after the retirement of RHIC. The EIC is expected to begin operations in the early 2030s [71]. A schematic of the EIC is shown in Fig. 2.8 where the additional Electron Storage Ring (cyan color), Polarized Electron source, Injector Linac and Electron cooler are built including the former RHIC. The EIC project was officially launched in December 2019 when it was granted Critical Decision Zero (CD0) [72].

Currently, it is expected that the EIC should start operate in the early 2030s. The new collider will allow to collide polarized electrons with polarized light ions at high intensities. The cost of the EIC project was estimated between 1.6 and 2.6 billion $ [73].

The planned EIC will have to fulfill following requirements [72]:

- Collisions of protons and electrons polarized at least at a level of 70%.

- The wide-ranging scale of different ions (from deuterium to uranium).

- The collision energies $\sqrt{s_{\mathrm{NN}}} = $ 20-100 GeV for e-p collisions including possibility of additional upgrade up to 140 GeV.

- The luminosity at least 10^{33} - 10^{34} cm^{-2}·s^{-1}.
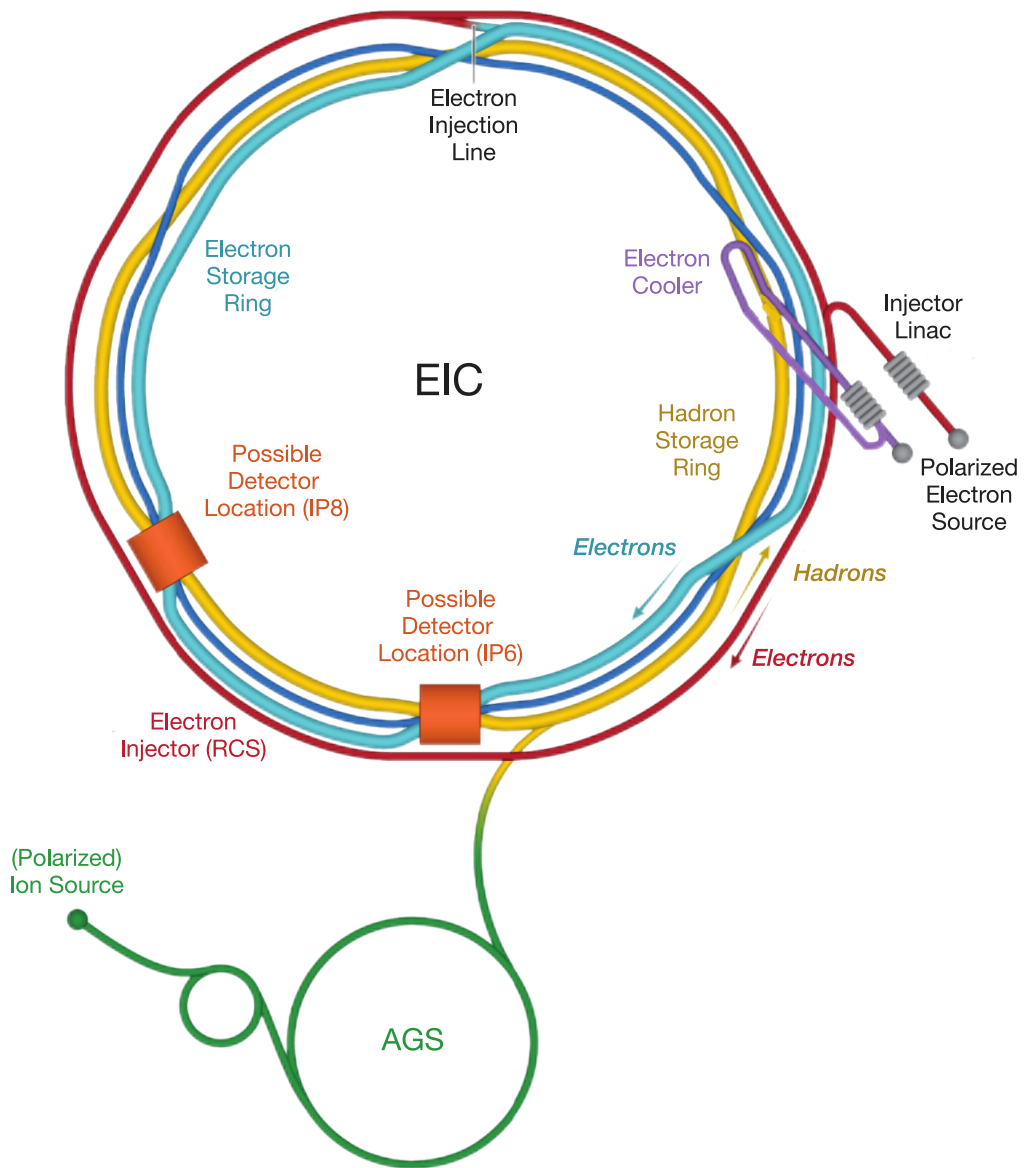
Figure 2.8: The layout of the planned EIC [72].

For purpose of new colliding beams, a new suitable detector is required. The EIC program includes the study of the inclusive, semi-inclusive and exclusive processes of the electron-light nucleus, electron-heavy nucleus and polarized electron-light nucleus collisions. The preliminary proposal of the detector can be seen as a 3D model in Fig. 2.8. The required pseudorapidity coverage is $|\eta| < 3.5$. The precision of tracking should have a resolution of 20 μm for all coordinates. For the momentum measurement, the 2% resolution for $p_{\mathrm{T}} > 0.1$ GeV/c is required. In addition, the detector should be able to identify electrons, hadrons including jet energy measurement [72].

Figure 2.9: The generic concept of the future EIC detector [72].

Chapter 3

Global polarization of hyperons in heavy-ion collisions

3.1 Hyperons

Hyperons are baryons that contain at least one s-quark and no heavier quarks [7]. This name was first suggested by Louis Leprince-Ringuet at the Bagnères de Bigorre conference in 1953 [74]. Examples of hyperons are:

$$\Lambda \ (uds), \quad \Sigma^+ \ (uus), \quad \Sigma^0 \ (uds), \quad \Sigma^- \ (dds), \quad \Xi^0 \ (uss), \quad \Xi^- \ (dss), \quad \Omega^- \ (sss).$$

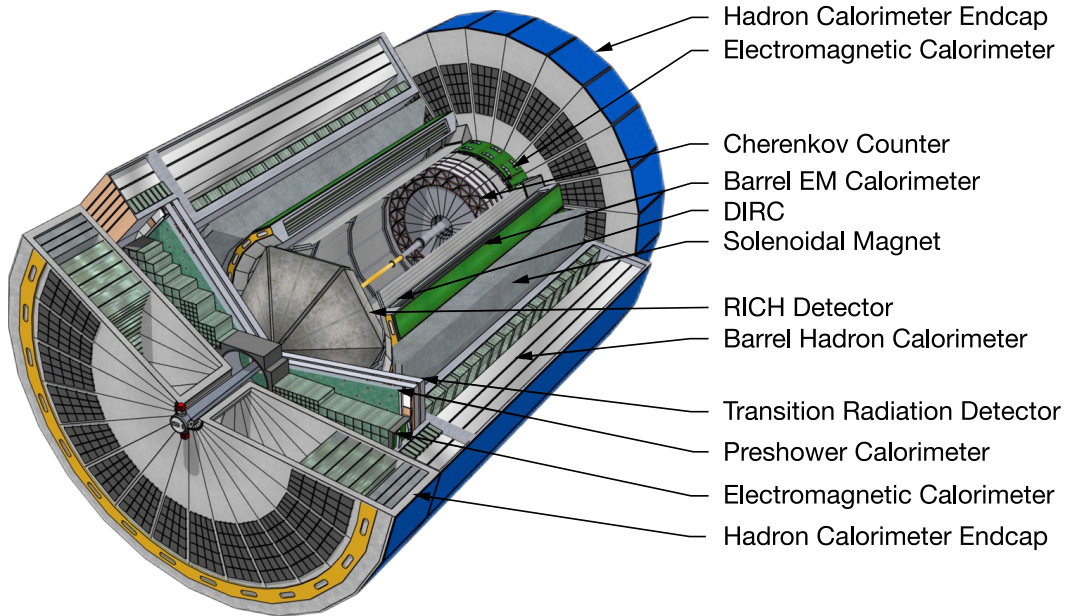The hyperons may be also part of a nucleus. Such nuclei are called hypernuclei. They were first discovered by Marian Danysz and Jerzy Pniewski in Warsaw in 1952 [75],[76]. Later, more than 40 single Λ-, few double Λ- and single Ξ- hypernuclei were identified by means of high-energy accelerators. The hyperons including the hypernuclei are unstable in classical conditions and decay into nuclei, cf. Tab. 3.1. However, it is expected that in neutron stars, matter maintains the weak equilibrium between the hyperon decays and the related inverse processes. Hence, some amount of hyperons can persist in the inner core of neutron stars whether the inverse process of decay is energetically advantageous. The studies of hypernuclei properties could help to find or at least constraint the equation of state for the neutron stars [77].

	Λ	$^5_\Lambda$He	$^{12}_\Lambda$C	$^{28}_\Lambda$Si
τ [ps]	263 ± 2	278 ± 11	212 ± 7	206 ± 11

Table 3.1: Examples of hypernuclei including their mean lifetimes τ compared to Λ hyperon [78].

3.1.1 Λ hyperon

The first observation of a new unknown neutral particle was performed in Wilson cloud chamber by G. D. Rochester and C. C. Butler in 1947. They expected spontaneous

decay of new neutral particle into lighter charged particles, see Fig. 3.1 [79]. Similar events were observed by A. J. Seriff et al. [80] in a series of 10 000 photographs made in the cloud chamber.[1] Using the geometry of the chamber and the relativistic time dilatation factor, it was computed that the mean lifetime of the new neutral particle is $\tau = (3 \pm 2) \cdot 10^{-10}$ s [80]. This relatively long lifetime was unexpected based on the assumed strong interaction that anticipated the mean lifetime on the order of 10^{-23} s [81]. This strange property together with the observation that these new particles are always produced in pairs gave them the label strange [82].
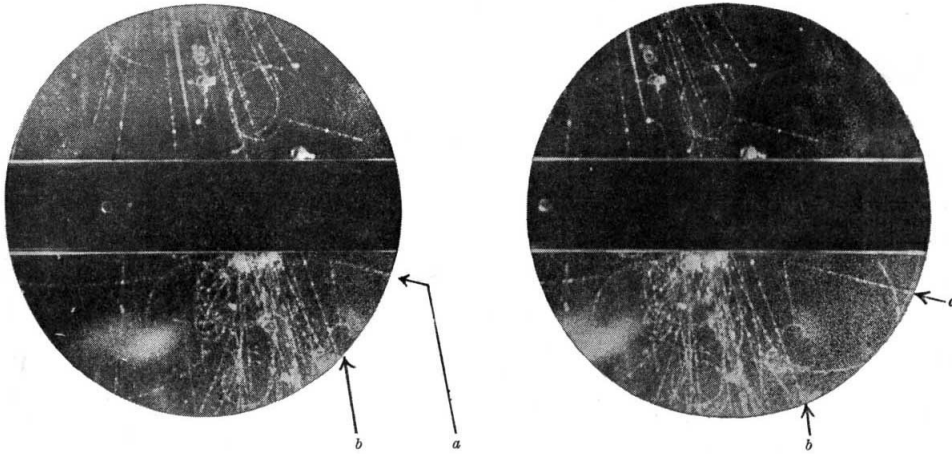
Figure 3.1: Photographs of a fork trajectory (a,b) in the gas. Positive particles going downwards are curved in an anticlockwise direction in the magnetic field [79].

However, the cloud chamber did not allow the identification of the daughter particle. In 1950, V. D. Hopper and S. Biswas observed the new particle in a 400μm-thick Ilford G5 nuclear emulsion at an altitude of 21 km [83]. The results shown that daughters are proton and pion or muon (at that time improperly called μ-meson). They also refuted the option that the observed fork trajectory (also called "V" trajectory) is just the collision of a charged particle with a neutral particle [83]. Hereby, the existence of the new particle called Λ was confirmed.
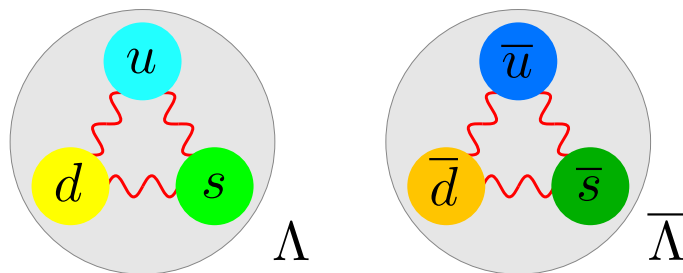
Figure 3.2: The Λ and $\overline{\Lambda}$ hyperons.

The Λ particle is classified as baryon, hyperon and V-particle because, as can be seen in Fig. 3.1, its decay resembles a V-shape in the bubble chamber where just the

---

[1]The Λ particle was not the only new observed particle. They observed another new unknown strange particles which was later labeled as kaons [79].

38

charged particles can be observed [81]. The Λ and $\overline{\Lambda}$ particles consist of $u-$, $d-$, and $s-$quark and $\overline{u}-$, $\overline{d}-$, and $\overline{s}-$quark, respectively, see Fig. 3.2. The main properties of these particles are gathered in Tab. 3.2.

|	Q [e]	m [MeV/c^2]	τ [10^{-10} s]	cτ [cm]	$I(J^P)$	$\alpha(p^{\pm}\pi^{\mp})$	S
Λ	0	1115.683 ± 0.006	2.632 ± 0.020	7.89	$0(\frac{1}{2}^+)$	0.732 ± 0.014	-1
$\overline{\Lambda}$						-0.758 ± 0.012	1

Table 3.2: The main properties of Λ and $\overline{\Lambda}$ hyperons where Q represents electric charge, m is the mass, τ is the mean lifetime, I is the isospin, J is the spin, P is the parity, α is the decay parameter for the main decay channel and S is the strangeness [84].

The main decay channels for Λ hyperon are gathered in Tab. 3.3 where the most useful for the Λ polarization measurements is the first one because of the charged daughters.

Γ_i	Fraction (Γ_i/Γ)
$\Lambda \rightarrow p + \pi^-$	(63.9 ± 0.5)%
$\Lambda \rightarrow n + \pi^0$	(35.8 ± 0.5)%
$\Lambda \rightarrow n + \gamma$	(1.75 ± 0.15)·10^{-3}

Table 3.3: The main decays modes for Λ hyperon [84].

3.2 Vorticity

The vorticity vector $\vec{\omega}$ plays an important part in the study of the kinematics of continuum. As the other important quantities in this area of physics, the vorticity vector can be defined employing velocity gradient tensor L_{ij} defined as

$$L_{ij} = \frac{\partial u_i}{\partial x_j}, \tag{3.1}$$

where $\vec{u}$ is the velocity vector. The vorticity vector is introduced as

$$\omega_i = \mathcal{E}_{ijk} L_{jk} \quad \text{or} \quad \vec{\omega} = \vec{\nabla} \times \vec{u}, \tag{3.2}$$

where $\mathcal{E}_{ijk}$ denotes the Levi-Civita symbol and $\vec{\nabla} = \left(\frac{\partial}{\partial x}; \frac{\partial}{\partial y}; \frac{\partial}{\partial z}\right)$ [85]. The units of $|\vec{\omega}|$ are inverse seconds, s^{-1}. One can imagine the vorticity by a paddle wheel in water where the water currents have different strengths, cf. Fig. 3.3. The direction of the vorticity can be determined by the right-hand rule - curl fingers in direction of the wheel rotation and thumb shows the vorticity direction [86]. Briefly, the vorticity ω is related to the angular velocity Ω as follows

$$\omega = \vec{\nabla} \times \overbrace{\vec{v}}^{\vec{\Omega}\times\vec{r}} = \Omega(\vec{\nabla} \cdot \vec{r}) - r\overbrace{(\vec{\nabla} \cdot \vec{\Omega})}^{0} = \Omega\left(\frac{\partial x}{\partial x} + \frac{\partial y}{\partial y} + \frac{\partial 0}{\partial z}\right) = 2\Omega. \tag{3.3}$$

Therefore in some cases [7], the additional factor $1/2$ is added to the definition in Eq. 3.2. Using this alternative definition, the vorticity ω has exactly the same value as the angular velocity Ω. In short, the angular momentum is manifested as vorticity in the case of flow description.
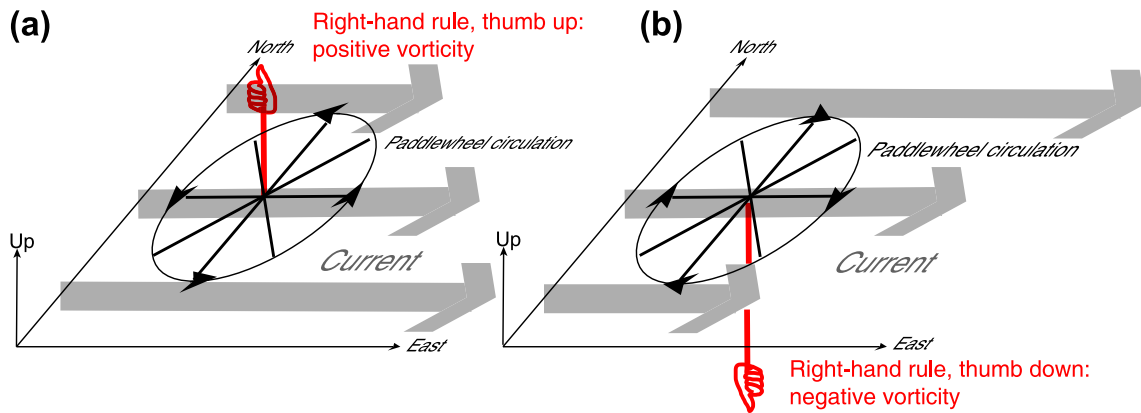
Figure 3.3: Visualization of the positive (a) and negative (b) vorticity. The thumb shows its direction [86].

In non-central collisions of two heavy ion nuclei where the QGP was produce, the strong vorticity of the fluid medium can be observed. In Fig. 3.4, the schematic of such collision in the reaction plane with impact parameter $\vec{b}$ is depicted. The upper part of the figure presents situation before the collision.
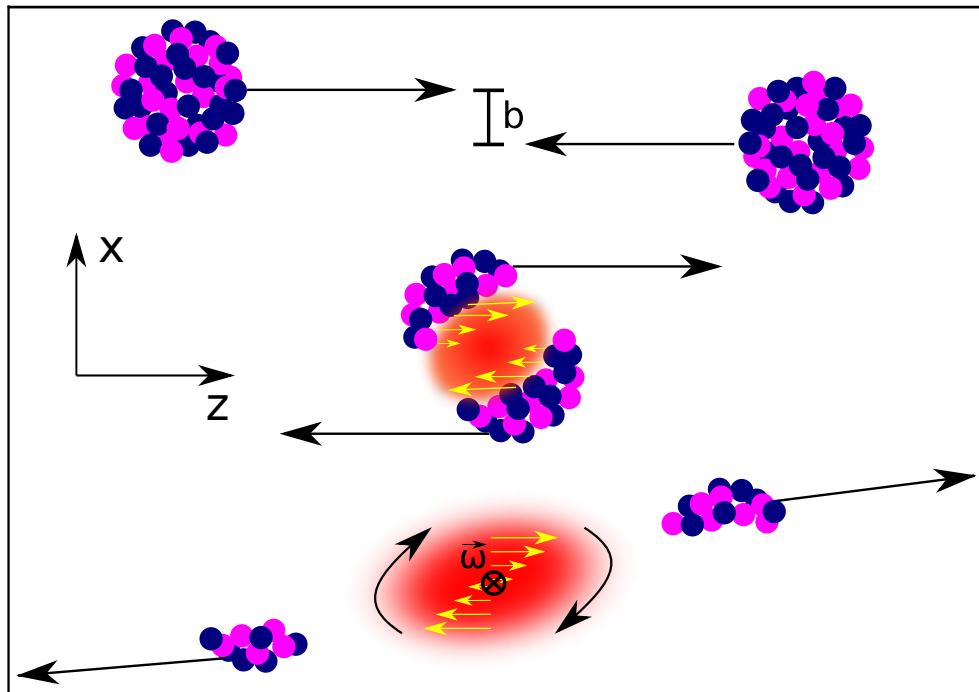
Figure 3.4: Collision of two heavy ions with impact parameter $b > 0$ in the $x - z$ plane (reaction plane) where z is the beam direction and $\vec{\omega}$ is the vorticity of the created QGP.

The second and third parts of the picture show the creation of the fireball (the red area) by the high deposition of the energy from overlapping and colliding participants of the collision. The spectators continue in their direction with light deflection caused by the repulsive impulse in the time of the collision. This deflection from t z axis can be labeled as positive and it manifests positive directed flow v_1 in the forward direction. The opposite, negative deflection, is also possible but for much lower energies [8]. In fact, the deflection can reveal the direction of the fireball angular momentum which on average due to symmetry gives the average direction of the vorticity. The angular momentum of the system J_{sys} by means of the spectators is estimated by forward detectors situated at large pseudorapidity.

The estimated value of the vorticity for the QGP for $\sqrt{s_{\mathrm{NN}}}$-averaged collisions is $\omega = (9 \pm 1) \cdot 10^{21}$ s^{-1}. For comparison [7]:

- Solar subsurface flow $\omega = 10^{-7}$ s^{-1}.

- Large-scale terrestrial atmospheric patterns $\omega = 10^{-7} - 10^{-5}$ s^{-1}.

- Supercell tornado cores $\omega = 10^{-1}$ s^{-1}.

- Heat soap bubbles $\omega = 100$ s^{-1}.

- Superfluid nanodroplets $\omega = 10^7$ s^{-1}.

As can be seen, the vorticity of the QGP could be the most vortical fluid ever observed in the universe.

3.3   Chiral vortical effect

The vorticity of the QGP cannot be measured directly. One can just observe its influence on the created particles and from it reconstruct its original value. This influence is known as chiral vorticity effect (CVE) and it causes polarization of the fermions in the QGP. ´

It is noteworthy that one might find analogy between the fluid rotation and electromagnetic fields. The fluid velocity $\vec{u}$ is an analogy to vector gauge potential $\vec{A}$ and the $\vec{\omega}$ is analogous to the magnetic field $\vec{B}$ because they meet the condition

$$\vec{B} = \vec{\nabla} \times \vec{A}, \tag{3.4}$$

which resembles Eq. (3.2). If a charged particle circulating perpendicular to a constant magnetic field $\vec{B}$, the quantum mechanical effect adds a phase factor

$$\exp\left(\frac{iQe\Phi_B}{\hbar}\right), \tag{3.5}$$

where Q is a charge of the particle and Φ_B is magnetic flux through the circle. In case of the same configuration but with the distinction that particle is circulating in

the constant field $\vec{\omega}$ instead of $\vec{B}$, the gained phase factor is as follows

$$\exp\left(\frac{iL}{\hbar}\right), \tag{3.6}$$

where L is the related angular momentum. Hence, one could expect vorticity-driven effects as the analogy to the chiral magnetic effect (CME) and the chiral separation effect (CSE). Currently, this effect is described in the anomalous hydrodynamic framework [87]. The vector current $\vec{J}$ along the vorticity direction from the CVE is

$$\vec{J} = \frac{1}{2\pi^2}\mu_5\mu_B\vec{\omega}, \tag{3.7}$$

where μ_5 is the chiral chemical potential and μ_B is the baryon chemical potential. The analogous vector current for the CME has form

$$\vec{J} = \frac{e^2}{2\pi^2}\mu_5\vec{B}. \tag{3.8}$$

As can be seen, the main distinction is that CVE is driven by the term $\mu_B\vec{\omega}$ and CME by $\vec{B}$ in a medium with non-zero chiral chemical potential μ_5. In the case of the CVE, the effective interaction of the fermions with spin $\vec{S}$ in their rest frame in the presence of the global rotation, has form $\sim -\vec{\omega}\cdot\vec{S}$ [87]. This interaction polarizes the quarks in sense of their spin direction which is preferably aligned with the vorticity $\vec{\omega}$, see Fig. 3.5.
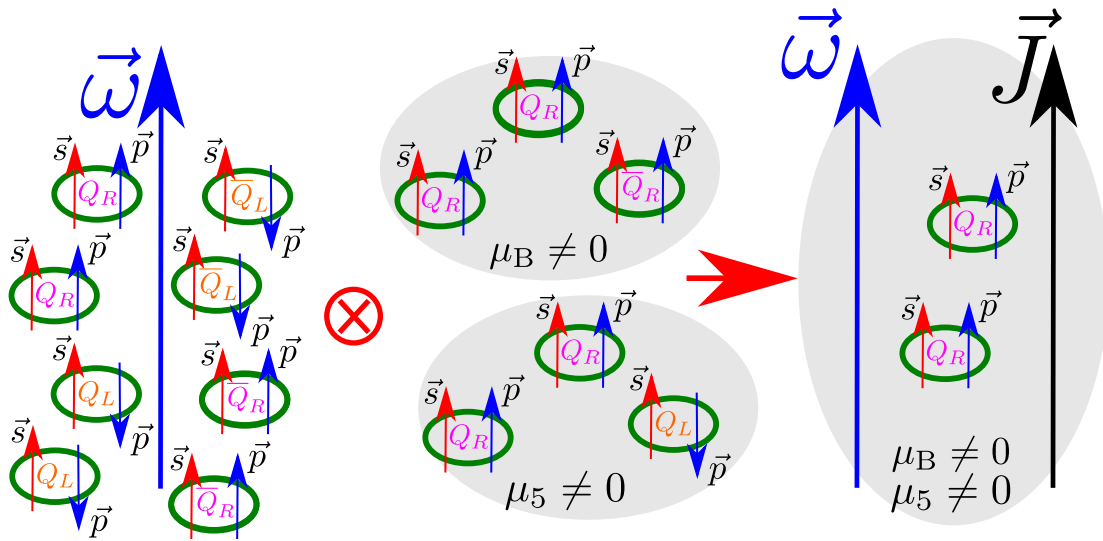
Figure 3.5: Illustration of the chiral vortical effect for massless quarks and antiquarks where $\mu_B > 0$, $\mu_5 > 0$, $\vec{\omega}$ is the vorticity and $\vec{J}$ is the vector current [87], modified.

This kind of polarization is so-called charge-blind contrary to the magnetic polarization. Hence follows that in the case of $\mu_5 > 0$, there is more right-handed quarks and antiquarks than the left-handed ones moving along the vorticity direction $\vec{\omega}$ because

$$\langle\vec{p}\rangle \propto \langle\vec{s}\rangle \propto \vec{\omega}, \tag{3.9}$$

where $\vec{p}$ and $\vec{s}$ are the fermion momentum and spin, respectively.

However, the question arises, how the polarization of the quarks is transferred to the hadrons after the hadronization of the QGP. According to the non-relativistic quark model, entire spin of the Λ hyperon is formed by s-quark and u- with d-quark should be paired to zero spin and isospin [88], [89]. The same model also predicts that the quarks form whole spin of nucleons. However, it was shown that the latter statement does not match the measured data [88]. The core of the problem is that the quarks in hadron are confined in a very small area. Therefore they have to be treated as relativistic [90]. Regarding the Λ hyperon, data suggests that s-quark holds approximately 60% of the hyperon spin, whereas u- and s-quark 40% [89].

In summary, the chiral vortical effect polarizes quarks in the QGP and the polarization is transfer to the created hyperons. Hence, the hyperons keep information about the initial vorticity. Nevertheless, even the direct measurement of the spin orientation of the short living hyperons is not feasible. Fortunately, the hyperons are so-called self-analyzing, i.e. in their decays, the daughter baryons prefers the direction of the mother hyperon spins. The polarization of the hyperon with respect to the global angular momentum of the system $\vec{J}_{sys}$ is

$$P_{\mathrm{H}} = \frac{8}{\pi \alpha_{\mathrm{H}}} \frac{\langle \sin\left(\Psi_1 - \phi_p^*\right)\rangle}{\mathscr{R}_1}, \tag{3.10}$$

where Ψ_1 is the event plane of the first order, $\mathscr{R}_1$ its resolution, ϕ_p^* is the azimuthal angle of the daughter baryon in the rest frame of the mother hyperon and α_{H} is the decay parameter.

Once the global hyperon polarization is known, for instance for Λ and $\overline{\Lambda}$ hyperon, the vorticity[2] may be computed via the hydrodynamical estimation

$$\omega \approx \frac{k_{\mathrm{B}}T}{\hbar} \left(P_{\Lambda'} + P_{\overline{\Lambda'}}\right), \tag{3.11}$$

where k_{B} is the Boltzmann constant, T denotes the fluid temperature at the particle emitting moment and the superscripts (e.g. Λ') mean that the related hyperons have to be primary [7].

3.4 Decay parameter α

The decay parameter α for parity-violating weak decays is one of the important observables for polarization measurements. In the case of Λ and $\overline{\Lambda}$ decay, one can study the related decay parameters α_{Λ} and $\alpha_{\overline{\Lambda}}$ separately as a check of CP symmetry for strange baryons. These studies can help with matter-antimatter asymmetry observed in the Universe [91].

To derive Eq. 3.10 including the decay parameter α_{H}, one considers Λ particle decaying into two particles (p and π^-) in its rest frame. Next, the spin orientation of

---

[2]There is considered the additional factor $1/2$ in Eq. 3.2.

the mother particle is in the positive direction of the z-axis [92]. This state is labeled as

$$\Psi_\Lambda = s_{\frac{1}{2}}, \tag{3.12}$$

where $s_{\frac{1}{2}} = \begin{pmatrix} 1 \\ 0 \end{pmatrix}$ represents "spin-up" orientation and $s_{-\frac{1}{2}} = \begin{pmatrix} 0 \\ 1 \end{pmatrix}$ would describe "spin-down" orientation.

Due to angular momentum conservation, the final states of daughter proton are restricted to three cases:

$$\Psi_1 = A_s Y_{0,0} s_{\frac{1}{2}}, \tag{3.13}$$

$$\Psi_2 = A_p \left(-\sqrt{\frac{1}{3}}\right) Y_{1,0} s_{\frac{1}{2}}, \tag{3.14}$$

$$\Psi_3 = A_p \sqrt{\frac{2}{3}} Y_{1,1} s_{-\frac{1}{2}}, \tag{3.15}$$

where $Y_{l,m}$ is spherical harmonic (eigenfunctions of the orbital angular momentum squared), the numbers $-\sqrt{\frac{1}{3}}$ and $\sqrt{\frac{2}{3}}$ are related Clebsch-Gordon coefficients and A_s and A_p are amplitudes of the angular momentum state[3]. In this notation, letter s represents angular momentum $l = 0$ and p represents $l = 1$ [92].

As can be seen from the final states, considered orbital momenta are s and p. The conservation of parity can be expressed as

$$\underbrace{\xi_\Lambda}_{+1} = \underbrace{\xi_p}_{+1} \cdot \underbrace{\xi_{\pi^-}}_{-1} \cdot (-1)^l, \tag{3.16}$$

where ξ is the intrinsic parity of the related particle and l is the angular momentum of the final state. From the Eq. (3.16), one can see that the parity conservation is violated for s final state.

The total wave function of the final state is

$$\Psi = \Psi_1 + \Psi_2 + \Psi_3 = \underbrace{(A_s + A_p \cos\theta^*)}_{A_{\frac{1}{2}}} s_{\frac{1}{2}} + \underbrace{(A_p e^{i\phi^*} \sin\theta^*)}_{A_{-\frac{1}{2}}} s_{-\frac{1}{2}}, \tag{3.17}$$

where θ^* and ϕ^* are the polar and angular angle in the rest frame of the Λ particle, respectively. The angular distribution of the p in the rest frame of Λ can be computed as follows

$$\begin{aligned}\frac{dN}{d\cos\theta^*} &= \Psi^*\Psi = |A_{\frac{1}{2}}|^2 + |A_{-\frac{1}{2}}|^2 + 2\,\mathrm{Re}(A_{\frac{1}{2}}^* A_{-\frac{1}{2}}) \\ &= |A_s|^2 + |A_p|^2 + 2\,\mathrm{Re}(A_s^* A_p)\cos\theta^*.\end{aligned} \tag{3.18}$$

Hence after the normalization of the wave function, one gets

$$\frac{dN}{d\cos\theta^*} = 1 + \underbrace{2\,\mathrm{Re}(A_s^* A_p)}_{\alpha}\cos\theta^*, \tag{3.19}$$

---

[3]Because of the sign convention, $-A_p$ is later used instead of A_p.

where the definition of the decay parameter α can be found [92]. If the decay parameter is nonzero, an asymmetry of up and down spin orientation occurs. Hence one can observe the violation of the parity conservation.

Let's now consider a particle with general spin orientation

$$\Psi = as_{\frac{1}{2}} + bs_{-\frac{1}{2}}, \tag{3.20}$$

where a and b are complex coefficients normalized as follows

$$|a|^2 + |b|^2 = 1. \tag{3.21}$$

The polarization vector $\vec{P}$ of that particle can be expressed as

$$\vec{P} = \Psi^* \vec{\sigma} \Psi, \tag{3.22}$$

where $\vec{\sigma}$ is a vector of Pauli matrices

$$\vec{\sigma} = (\sigma_1; \sigma_2; \sigma_3) = \left(\begin{pmatrix} 0 & 1 \\ 1 & 0 \end{pmatrix}; \begin{pmatrix} 0 & -i \\ i & 0 \end{pmatrix}; \begin{pmatrix} 1 & 0 \\ 0 & -1 \end{pmatrix} \right). \tag{3.23}$$

Hence, the polarization vector is 1 in the direction

$$\vec{P} = (2\operatorname{Re}(a^* \cdot b); 2\operatorname{Im}(a^* \cdot b); |a|^2 - |b|^2). \tag{3.24}$$

Whether the spin orientation is defined by the azimuthal angle ϕ^* and the polar angle θ^*, one can write coefficients a and b as

$$a = -\sin\left(\frac{\theta^*}{2}\right), \qquad b = \mathrm{e}^{i\phi^*}\sin\left(\frac{\theta^*}{2}\right). \tag{3.25}$$

Now, one returns to the final state in Eq. (3.17) that can be normalized into

$$\Psi_p = \frac{\Psi}{|\Psi|} = \underbrace{\frac{A_s + A_p\cos\theta^*}{\sqrt{1 + \alpha\cos\theta^*}}}_{a} s_{\frac{1}{2}} + \underbrace{\frac{A_p\mathrm{e}^{i\phi^*}\sin\theta^*}{\sqrt{1 + \alpha\cos\theta^*}}}_{b} s_{-\frac{1}{2}}. \tag{3.26}$$

As the mother particle is oriented in the z direction, one can choose $\phi^* = 0$ without loss of generality. Because of this choice, the direction of the proton emission is limited to the $z - x$ plane. The polarization vector components defined in Eq. (3.24) are

$$(1 + \alpha\cos\theta^*)P_x = 2\operatorname{Re}\left[(A_s^* + A_p^*\cos\theta^*)(A_p\sin\theta^*)\right] =$$

$$= \overbrace{2\operatorname{Re}[A_s^* A_p]}^{\alpha}\sin\theta^* + 2|A_p|^2\cos\theta^*\sin\theta^*, \tag{3.27}$$

$$(1 + \alpha\cos\theta^*)P_y = 2\operatorname{Im}\left[(A_s^* + A_p^*\cos\theta^*)(A_p\sin\theta^*)\right] =$$

$$= \overbrace{2\operatorname{Im}[A_s^* A_p]}^{\beta}\sin\theta^* + 2\overbrace{\operatorname{Im}(|A_p|^2)}^{=0}\cos\theta^*\sin\theta^* =$$

$$= \beta\sin\theta^*, \tag{3.28}$$

$$(1 + \alpha\cos\theta^*)P_z = |(A_s + A_p\cos\theta^*)|^2 - |A_p\sin\theta^*|^2 =$$

$$= |A_s|^2 + |A_p|^2 \cos^2 \theta^* + \overbrace{2\,\mathrm{Re}(A_s^* A_p)}^{\alpha} \cos \theta^* - |A_p|^2 \sin^2 \theta^* =$$

$$= \overbrace{|A_s|^2 - |A_p|^2}^{\gamma} + 2|A_p|^2 \cos^2 \theta^* + \alpha \cos \theta^*, \qquad (3.29)$$

where β and γ are another decay parameters [92], see Fig. 3.6. Recall, these relations apply to the full Λ polarization only.
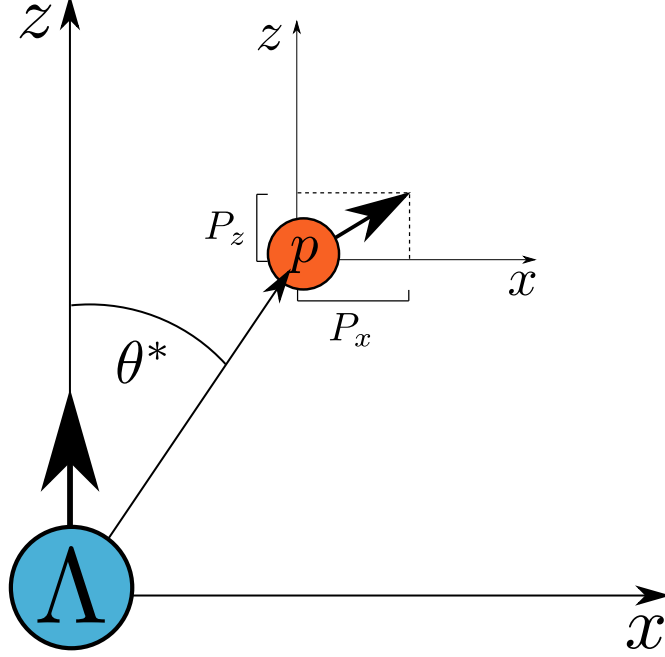
Figure 3.6: The decay of Λ baryon into a proton in Λ's rest frame in $z - x$ plane where θ^* is a polar angle of the proton emission, and p_x and p_y are projection of proton spin direction.

In order to describe the real situation, one considers Λ particles with spin along the z direction N^+ and with the opposite direction of the spin N^-. The Λ source polarization is

$$P_\Lambda = \frac{N^+ - N^-}{N^+ + N^-}. \qquad (3.30)$$

The expected value of p spin for a given direction for both Λ spin orientations, as can be seen in Fig. 3.7, can be computed as a weighted average, where the Λs with spin-up and spin-down orientations have weights N^+ and N^-, respectively [92]. For sake of simplicity, the direction of z and y axes are flipped in the case of spin-down orientation of the mother particle, thereby one gets similar equations as for the spin-up case, see Eq. (3.29), with the difference that

$$P_y \to -P_y,$$
$$P_z \to -P_z,$$
$$\cos \theta^* \to -\cos \theta^*.$$
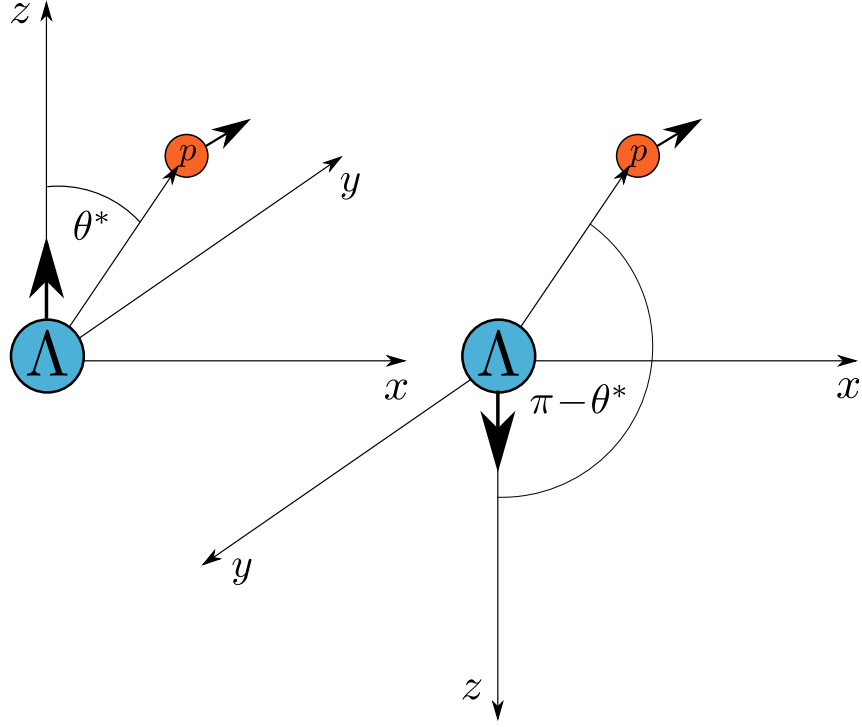
Figure 3.7: The decay of Λ baryon into a proton in Λ's rest frame with spin-up (left) and spin-down (right) configuration where the emission of the daughter proton is fixed in the same direction.

The above-mentioned weighted averages can be derived as follows

$$\frac{N^+}{N^+ + N^-}(1 + \alpha \cos \theta^*)P_x + \frac{N^-}{N^+ + N^-}(1 - \alpha \cos \theta^*)P_x =$$

$$= \frac{N^+}{N^+ + N^-}(\alpha \sin \theta^* + 2|A_p|^2 \cos \theta^* \sin \theta^*) + \frac{N^-}{N^+ + N^-}(\alpha \sin \theta^* - 2|A_p|^2 \cos \theta^* \sin \theta^*)$$

$$\left(1 + \overbrace{\frac{N^+ - N^-}{N^+ + N^-}}^{P_\Lambda} \alpha \cos \theta^*\right)P_x = \alpha \sin \theta^* + 2 \overbrace{\frac{N^+ - N^-}{N^+ + N^-}}^{P_\Lambda} |A_p|^2 \cos \theta^* \sin \theta^*$$

$$P_x = \frac{\alpha \sin \theta^* + 2P_\Lambda |A_p|^2 \cos \theta^* \sin \theta^*}{1 + P_\Lambda \alpha \cos \theta^*}, \tag{3.31}$$

$$(1 + P_\Lambda \alpha \cos \theta^*) P_y = \frac{N^+}{N^+ + N^-}\beta \sin \theta^* + \frac{N^-}{N^+ + N^-}(-\beta \sin \theta^*)$$

$$P_y = \frac{P_\Lambda \beta \sin \theta^*}{1 + P_\Lambda \alpha \cos \theta^*}, \tag{3.32}$$

$$(1 + P_\Lambda \alpha \cos \theta^*) P_z = \frac{N^+}{N^+ + N^-}(\gamma + 2|A_p|^2 \cos^2 \theta^* + \alpha \cos \theta^*) +$$

$$+ \frac{N^-}{N^+ + N^-}(-\gamma - 2|A_p|^2 \cos^2 \theta^* + \alpha \cos \theta^*)$$

$$P_z = \frac{P_\Lambda \gamma + 2P_\Lambda |A_p|^2 \cos^2 \theta^* + \alpha \cos \theta^*)}{1 + P_\Lambda \alpha \cos \theta^*}. \tag{3.33}$$

From the form of Eq. (3.31), (3.32) and (3.33) one can read out that the angular distribution of protons in the rest frame of mother Λ particle with $P_\Lambda < 1$ has form

$$\frac{\mathrm{d}N}{\mathrm{d}\cos\theta^*} = 1 + P_\Lambda \alpha \cos\theta^*. \tag{3.34}$$

In conclusion, the α parameter describes the interference between parity-violating s and parity-conserving p contribution, see Eq. (3.17). It is an important value for Λ polarization computation. As this chapter is focused on hyperon decays, the α parameter will be denoted as α_H where H denotes the related hyperon.

3.5 Global polarization of Λ hyperon
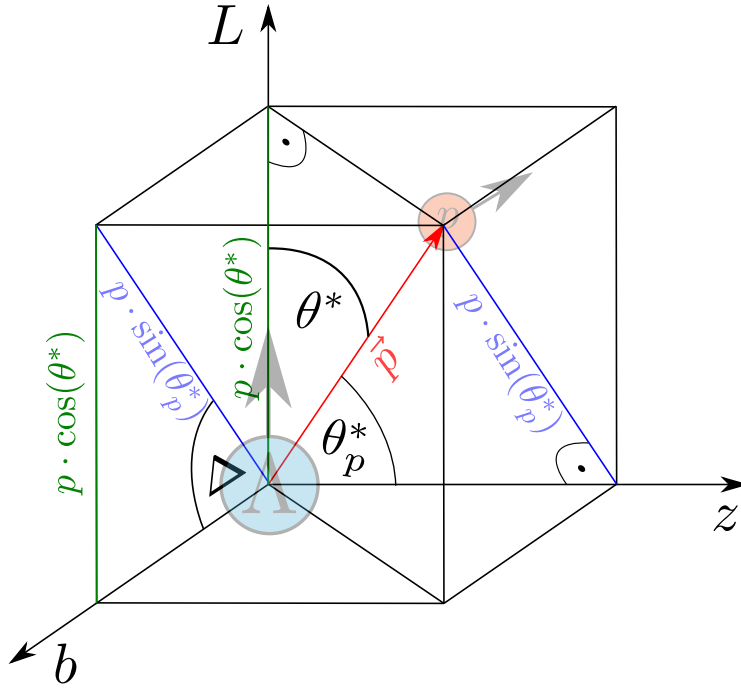
Figure 3.8: The decay of Λ hyperon into a proton in Λ's rest frame where L, z and b are the angular momentum of the system, beam axis and direction of the impact parameter, respectively, $\vec{p}$ is an unit vector of the proton emission direction, θ^* is the polar angle of the proton w.r.t L axis, $\Delta = \Psi_\mathrm{RP} - \phi_p^*$, and θ_p^* is the polar angle of the proton w.r.t. z-axis.

The daughter proton distribution in Eq. (3.34) is related to the polar angle θ^* that depends on the reaction plane orientation which might be different in each HI collision. Therefore, it is better to choose the polar angle θ_p^* with respect to the z-axis which is in each collision identical. As illustrated in Fig. 3.8, the $\cos\theta^*$ can be rewritten by means of θ_p^* as follows

$$\cos\theta^* = \sin\theta_p^* \sin\left(\Psi_\mathrm{RP} - \phi_p^*\right), \tag{3.35}$$

where Ψ_{RP} is the angle of the reaction plane and ϕ_p^* is the azimuthal angle of the daughter proton w.r.t. the z-axis.

Now, one can derive the global polarization along the global angular momentum of the system $\vec{J}_{sys}$ as follows

$$
\langle\sin(\Psi_{\mathrm{RP}}-\phi_p^*)\rangle = \frac{1}{4\pi}\int_S \overbrace{\frac{\mathrm{d}N}{\mathrm{d}\Omega}}^{\frac{\mathrm{d}N}{\mathrm{d}\cos\theta^*}}\sin(\Psi_{\mathrm{RP}}-\phi_p^*)\mathrm{d}\Omega =
$$

$$
=\frac{1}{4\pi}\int_S [1+\alpha_{\mathrm{H}}P_{\mathrm{H}}\cos(\theta^*)]\sin(\Psi_{\mathrm{RP}}-\phi_p^*)\overbrace{\mathrm{d}\Omega}^{\mathrm{d}(\cos\theta_p^*)\mathrm{d}\phi_p^*}
$$

$$
=\frac{1}{4\pi}\overbrace{\int_0^{2\pi}\mathrm{d}\phi_p^*\int_0^1 \mathrm{d}(\cos\theta_p^*)\sin(\Psi_{\mathrm{RP}}-\phi_p^*)}^{\int_0^{2\pi}\mathrm{d}\phi_p^*\sin(\Psi_{\mathrm{RP}}-\phi_p^*)=0}
$$

$$
+\frac{1}{4\pi}\int_0^{2\pi}\mathrm{d}\phi_p^*\int_0^1 \mathrm{d}(\cos\theta_p^*)\,\alpha_{\mathrm{H}}P_{\mathrm{H}}\overbrace{\cos(\theta^*)}^{\overbrace{\int_0^\pi \mathrm{d}\theta_p^*\sin\theta_p^*}\;\;\sin\theta_p^*\sin(\Psi_{\mathrm{RP}}-\phi_p^*)}\sin(\Psi_{\mathrm{RP}}-\phi_p^*)
$$

$$
=\frac{\alpha_{\mathrm{H}}P_{\mathrm{H}}}{4\pi}\overbrace{\int_0^{2\pi}\mathrm{d}\phi_p^*\sin^2(\Psi_{\mathrm{RP}}-\phi_p^*)}^{\pi}\overbrace{\int_0^\pi \mathrm{d}\theta_p^*\sin^2\theta_p^*}^{\frac{\pi}{2}}=\frac{\alpha_{\mathrm{H}}P_{\mathrm{H}}\pi}{8}. \quad (3.36)
$$

From Eq. (3.36) the global polarization P_{H} can be expressed as follows

$$
P_{\mathrm{H}} = \frac{8}{\alpha_{\mathrm{H}}\pi}\langle\sin(\Psi_{\mathrm{RP}}-\phi_p^*)\rangle. \qquad (3.37)
$$

The derived Eq. (3.37) is still not suitable due to impossibility of the direct measurement of the reaction plane Ψ_{RP}. Fortunately, the mean value of sinus resembles the definition of the hyperon directed flow

$$
v_1^{\mathrm{H}} = \langle\cos(\Psi_{\mathrm{RP}}-\phi_{\mathrm{H}})\rangle, \qquad (3.38)
$$

where ϕ_{H} is the azimuthal angle of the hyperon transverse momentum [93]. In the event plane method, the flow coefficients are calculated as follows

$$
v_n^{\mathrm{H}} = \frac{\langle\cos(n[\Psi_n^{A\cup B}-\phi_{\mathrm{H}}])\rangle}{\sqrt{\langle\cos(n[\Psi_n^A-\Psi_n^B])\rangle}} = \frac{\langle\cos(n[\Psi_n-\phi_{\mathrm{H}}])\rangle}{\mathscr{R}_n} = \frac{v_n^{\mathrm{obs}}}{\mathscr{R}_n}, \qquad (3.39)
$$

where Ψ_n denotes the EP of the n-th order and $\mathscr{R}_n$ is the resolution of the related Ψ_n. The EP is computed from the chosen group of particles A, B or both of them $A\cup B$ [94]. Due to similarity, one can utilize the same method and rewrite the Eq. (3.37) by means of the first order EP Ψ_1 into

$$
P_{\mathrm{H}} = \frac{8}{\alpha_{\mathrm{H}}\pi}\frac{\langle\sin(\Psi_1-\phi_p^*)\rangle}{\mathscr{R}_1}. \qquad (3.40)
$$

Theoretically, it is possible to measure the global polarization P_{H} of any hyperon. The main requirement is the weak parity-violating decay including some daughter baryon

as described in the derivation of the daughter baryon distribution in Chapter 1.4. The natural choice is the lightest strange baryon Λ or $\overline{\Lambda}$ with the highest abundance in HI collisions.

3.6   Event plane

The needed ingredient for the polarization measurement is the so-called event plane (EP). The reason for introducing the EP is that the reaction plane, see Fig. 1.9, cannot be measured directly because the impact parameter $\vec{b}$ defining this plane is immeasurable as well. Therefore, the EP can be perceived as an experimental estimation of the RP. Hence, there is a difference between them caused by a finite number of produced particles together with the particle multiplicity fluctuations between collisions at fixed impact parameter orientation [95]. Thus the resolution of the EP $\mathscr{R}_n$ has to be also computed to determine the precision.

In order to mathematically introduce the EP, more precisely the azimuthal angle of the EP with respect to the spectator plane, first one needs to introduce the so-called event flow vector $\vec{Q}_n$ (also called Q-vector) defined as

$$\vec{Q}_n = \begin{pmatrix} Q_{x,n} \\ Q_{y,n} \end{pmatrix} = \begin{pmatrix} \sum_i w_i \cos n\phi_i \\ \sum_i w_i \sin n\phi_i \end{pmatrix}, \tag{3.41}$$

where w_i and ϕ_i are the chosen weight and azimuthal angle of i-th produced charged particle, respectively. As the weight particle's transverse momentum p_{T}, energy E, or pseudorapidity η can be chosen, or one can compute weights maximizing the EP. Finally, the EP Ψ_n of the n-th harmonic (the n-th order) is calculated as

$$\Psi_n = \frac{1}{n} \arctan\begin{pmatrix} Q_{y,n} \\ Q_{x,n} \end{pmatrix}. \tag{3.42}$$

The n-th order of Ψ_n is in the range $\langle 0; 2\pi/n)$ [96].

3.6.1   Reconstruction of event plane

´

In this thesis, the EPD detector at STAR is used for the EP reconstruction. The weights w_i in Eq. (3.41) are chosen as

$$w_i = \begin{cases} 0 & \mathrm{nMIP} < Min \\ \mathrm{nMIP} & Min \leq \mathrm{nMIP} < Max \\ Max & Max \leq \mathrm{nMIP} \end{cases}, \tag{3.43}$$

where nMIP denotes the number of minimum ionizing particles. The thresholds are set to $Min = 0.3$ and $Max = 3$ to prevent the dark signal (Min) and the Landau fluctuation effect (Max) [97].

The nMIP value can be extracted from ADC (analog-to-digital converter) signal produced by the EPD. If a linear dependence of the particle lost energy dE in the tile of the EPD on the ADC value is considered, one can write

$$dE = G \cdot (ADC + o), \tag{3.44}$$

where a gain G and an offset o are calibration constants [98]. The linear consideration requires [98]:

- Proportionality of dE to number of photons.

- Proportionality of produced photons to number of transported photons to SiPM.

- Proportionality of number of generated electrons to number of photons impinging on SiPM.

- Linear gains of SiPM, FEE (Front End Electronics) and QT board.

However, the Eq. (3.44) is only a calibration equation in this case. The nMIP value from ADC signal can be obtained as follows

$$nMIP = \frac{ADC + o}{MIP}, \tag{3.45}$$

where MIP denotes the most probable value for the MIP via Landau distribution.

Assuming an ideal detector, the EP of the first order Ψ_1 could be computed by Eq. (3.42). Unfortunately, the EPD detector has finite acceptance and not all of the EPD's tiles have the same measurement sensitivity. These biases are collectively called acceptance correlations. To remove their negative influence on the results, one has to make the distribution of EP Ψ_1 isotropic in the laboratory frame [99]. This can be achieved by applying various correction, such as

- Weightings:

    - Phi-weighting - different weights for each tile of the EPD.
    - Ring-weighting - different weights for each ring of the EPD.
    - Eta-weighting - pseudorapidity η as the weight of each particle.

- Psi-shifting - flattening of the EP distribution via Fourier series [100].

Phi-weighting

For a finite element system, the EPD in this case, phi-weighting correction is trivial to introduce, assuming an azimuthal symmetry of each EPD ring for the particle flux averaged over a large sample of events and proportionality of the measured signal to the flux. As was already mention before, as the wights in Eq. (3.41) nMIP value from the ADC signal including the thresholds which can disrupt the clean linearity

is chosen. The anisotropies in the distribution $dw/d\phi$ considered as inefficiency may be corrected by a ϕ-dependent[4] coefficient b_k defined as

$$b_k \equiv \frac{\langle w \rangle_k}{\langle \langle w \rangle_k \rangle_r},$$

(3.46)

where w is defined in Eq. 3.43, r is the r-th EPD ring including the k-th tile of the detector and the angle brackets $\langle \dots \rangle_k$ and $\langle \dots \rangle_r$ denote the mean value for the given tile k and for all tiles in the given EPD ring r, respectively. The corrected weight w'_k is then nothing but

$$w'_k = \frac{w_k}{b_k}.$$

(3.47)

Most of the observed anisotropies in the distribution $dw/d\phi$ are cause by the particle scattering in the upstream material. Hence a multiplying effect occurs manifested as the greater number of measured particles than their number really was ($b_k > 1$). It was already shown, that phi-weighting itself is a strong tool enough to get a reasonably flat Ψ_1 distribution without the application of any other correction [101].

Ring-weighting

This correction considers different weight with respect to each ring or ring-groups (RGs) of the EPD. For Au-Au collisions at 27 GeV it was shown that the directed flow (v_1 coefficient) has a different sign for the inner rings and outer rings of the EPD, and if all of the tiles or rings are not weighted, the resolution of the EP deteriorates [102]. The next observations revealed that [102]:

- Each EPD ring is correlated (a few percent) with the adjacent rings.

- The inner rings (1-5) are strongly correlated through the entire group.

- The intermediate rings (6-11) are weakly correlated with the inner and outer RGs. These rings behaves like a transition area.

- The outer rings (12-16) are correlated with each other but negatively correlated with the inner ones.

The observed autocorrelation is caused by the flow and antiflow effects of spectators and participants.

The ring weights Z_r included in the ring-weighting for the first order EP Ψ_1 are introduced as follows

$$\Psi_1 = \arctan\left(\frac{\sum_{r=1}^{16} Z_r Q_{y,1,r}}{\sum_{r=1}^{16} Z_r Q_{x,1,r}}\right),$$

(3.48)

---

[4]Because the considered system is the EPD detector, more precisely it could be called tile-dependent.

where r represents each ring. Some of the weights can be chosen as $Z_r = 0$ whether one wants to neglect the problematic r-th ring.

In order to obtain the most optimal set of Z_r weights, one should maximize the resolution of the EP which corresponds to minimizing value of

$$\xi = 1 - \sqrt{\langle \cos \left[(\Psi_1^E - \Psi_1^W) \right] \rangle},$$ (3.49)

where Ψ_1^E and Ψ_1^W denote the first order EP obtained by the east and west wheel of the EPD, respectively. This mathematic problem is suitable for the CERN library MINUIT (Function Minimization and Error Analysis [103]). It should be noted that only the relative weights Z_r between each other are crucial for the analysis. Hence one can choose one an arbitrary non-zero value, and the number of remaining unknowns is 15.

Eta-weighting

Instead of ring-weighting, more general eta-weighting can be implemented. Assuming flow coefficient v_1 depends on the collision centrality C and pseudorapidity η, the $v_1(C, \eta)$ value can be used as the weight for measured charged particles passing the EPD. The straightest way to extract the weights is to divide the measured data with respect to the collision centrality bin C and then fit each of them with the flow coefficient v_1 using the third-order polynomial

$$v_1(\eta, C) = a\eta^3 + b\eta^2 + c\eta + d.$$ (3.50)

Because the quadratic coefficient b is always approximately 0 and the constant coefficient d is usually negative and low w.r.t. the other coefficients, both of them can be neglected [104]. Hence, the final weight is

$$v_1(\eta, C) = a\eta^3 + c\eta.$$ (3.51)

However, the knowledge of v_1 is not known until the first reconstruction. Therefore, for the first analysis, the ring-weighting has to be used as the first iteration. The most common choice of Z_r weights is $\vec{Z} = (1, 1, 1, 1, 1, \vec{0})$ where just inner rings are considered.

Psi-shifting

The psi-shifting correction is used to flatten the Ψ_1 distribution. The corrected distribution Ψ_1' can be expressed as

$$\Psi_1' = \Psi_1 + \Delta\Psi_1$$ (3.52)

with

$$\Delta\Psi_1 = \sum_n \left[A_n \cos(n\Psi_1) + B_n \sin(n\Psi_1) \right].$$ (3.53)

As follows from Eq. (3.52), the Ψ_1 distribution is flat provided that $\Delta\Psi_1 = 0$. Hence, the requirement on the Fourier coefficient is

$$A_n = -\frac{2}{n}\langle\sin(n\Psi_1)\rangle, \tag{3.54}$$

$$B_n = \frac{2}{n}\langle\cos(n\Psi_1)\rangle, \tag{3.55}$$

where the mean value denoted by $\langle\ldots\rangle$ is performed for a large sample of events. Consequently, the psi-shifting can be written as

$$\Psi'_1 = \Psi_1 + \sum_n \frac{2}{n}\left[-\langle\sin(n\Psi_1)\rangle\cos(n\Psi_1) + \langle\cos(n\Psi_1)\rangle\sin(n\Psi_1)\right]. \tag{3.56}$$

In practice, the correction is usually done up to the fourth harmonic ($n \leq 4$) because the other terms do not have significant effect on the EP resolution [105]. By repeated application of the psi-shifting the result Ψ_1 distribution can be flatten even more. Thus the full process of the EP correction including all the above-mentioned methods has to be repeated more times (iterated).

3.6.2 Resolution of event plane

The accuracy of the reconstructed EP is limited. Therefore, it is necessary to compute the resolution of the EP defined for n-th harmonic as follows

$$\mathscr{R}_n = \langle\cos[n(\Psi_n - \Psi_{\mathrm{RP}})]\rangle, \tag{3.57}$$

where the mean value $\langle\ldots\rangle$ is for a large sample of events. However, as was already mentioned the RP Ψ_{RP} cannot be measured. Thus resolution is computed in different way. It was derived [106] that the resolution can be expressed as

$$\mathscr{R}_n = \frac{\sqrt{\pi}}{2}\chi\exp\left(-\frac{\chi^2}{2}\right)\left[I_{\frac{k-1}{2}}\left(\frac{\chi^2}{2}\right) + I_{\frac{k+1}{2}}\left(\frac{\chi^2}{2}\right)\right] \tag{3.58}$$

with

$$\chi = v_n\sqrt{M}, \tag{3.59}$$

where I_k is the modified Bessel function of the first kind, v_n is the n-th flow coefficient and M is the multiplicity of particles used for the EP reconstruction. The dependence of the EP resolution on the parameter χ is shown in Fig. 3.9.
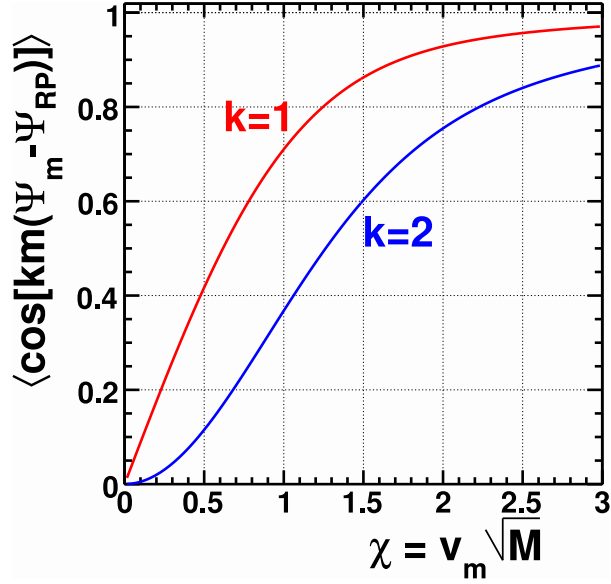
Figure 3.9: The resolution of EP $\mathscr{R}_n$ as a function of dimensionless resolution parameter χ [100].

In order to estimate the EP resolution, one should divide each event into two independent sub-events with equal multiplicity which are provided by the west (W) and east (E) wheel of the EPD in this thesis. The advantage of this step is that the sub-events are positively correlated because both of them are correlated with the RP. Hence, the EP resolution for the sub-events is the square root of the correlation, i.e.

$$\mathscr{R}_{n,\text{sub}} = \sqrt{\langle \cos[n(\Psi_n^{\text{W}} - \Psi_n^{\text{E}})]\rangle}. \tag{3.60}$$

The related resolution parameter χ_{sub} is computed as the solution for Eq. (3.58) by means of iteration. Finally, the full resolution is computed as

$$\mathscr{R}_{n,\text{full}} = \mathscr{R}(\sqrt{2}\chi_{\text{sub}}), \tag{3.61}$$

using Eq. (3.58). In the linear region of the resolution dependence ($\mathscr{R} < 0.5$), see Fig. 3.9 for $k = 1$, the full resolution can be approximated as

$$\mathscr{R}_{n,\text{full}} \approx \sqrt{2}\mathscr{R}_{n,\text{sub}}. \tag{3.62}$$

which greatly simplifies the calculation [100].

3.7 Recent results of global hyperon polarization

The current status of experimental results on the global Λ and $\overline{\Lambda}$ hyperon polarization P_{H} is shown in Fig. 3.10. The results show that the global Λ and $\overline{\Lambda}$ polarization increases with decreasing collision energy and there is a hint of higher P_{H} for $\overline{\Lambda}$ than for Λ.

The polarization at the highest energies ($\sqrt{s_{\text{NN}}} = 2.76$ TeV and 5.02 TeV) were measured by ALICE at LHC. The both polarization values for Λ and $\overline{\Lambda}$ hyperons are

consistent with zero. Nevertheless, the prove of the zero polarization would require larger statistics [107], [108]. The older results for energies ($\sqrt{s_{\mathrm{NN}}} = 7.7$ - 62.4 GeV and 200 GeV) are from the STAR experiment at RHIC. The newer results with improved statistical precision provided in 2018 revealed nonzero polarization at 200 GeV: $P_\Lambda = 0.277 \pm 0.040$ (stat.) $^{+0.039}_{-0.049}$ (syst.)% and $P_{\overline{\Lambda}} = 0.240 \pm 0.045$ (stat.) $^{+0.061}_{-0.045}$ (syst.)% [109].
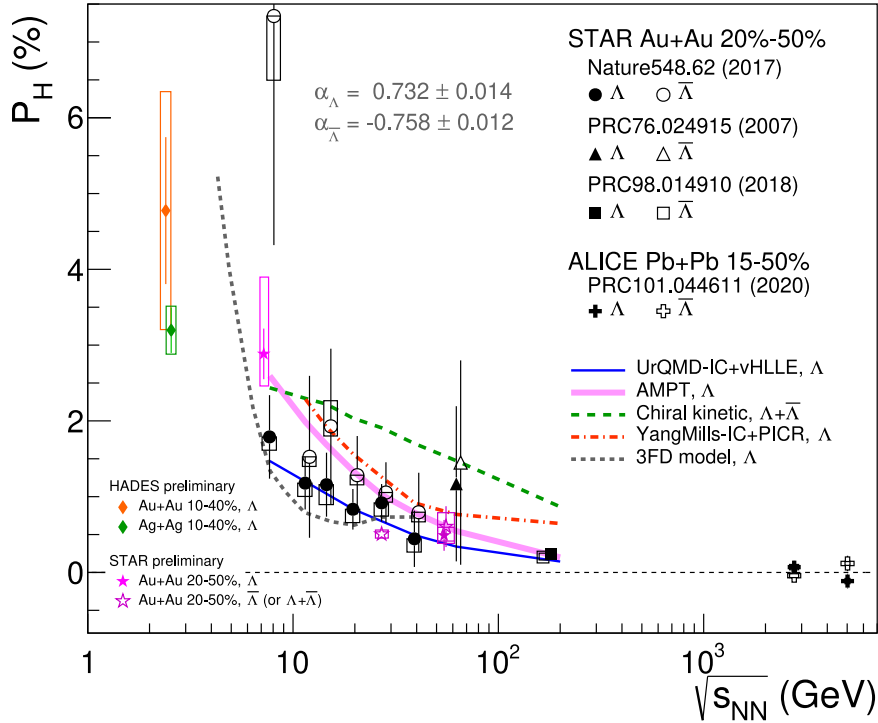

Figure 3.10: Global polarization of Λ (solid markers) and $\overline{\Lambda}$ (open markers) hyperon P_{H} in HI collisions as a function of collision energy $\sqrt{s_{\mathrm{NN}}}$ including predictions of various theoretical models [107].

Another interesting energy range for the hyperon polarization is $\sqrt{s_{\mathrm{NN}}} < 7.7$ GeV. The previous naive extrapolations of data expected higher polarization with a lower energy of a collision. However, the region is still not thoroughly explored. At STAR, the hyperon polarization for the above-mentioned energy range is measured in the fixed-targed mode. It is expected that the polarization should vanish at $\sqrt{s_{\mathrm{NN}}} = 2m_{\mathrm{N}}$ where m_{N} denotes the nucleon mass because of too low system angular momentum. Hence, a peak in the Λ polarization is expected, its location is predicted to be around $\sqrt{s_{\mathrm{NN}}} \approx 3$ GeV. Nevertheless, the $P_{\overline{\Lambda}}$ is complicated to measure because of its insufficient yield [110]. Therefore the preliminary STAR polarization measurement at $\sqrt{s_{\mathrm{NN}}} = 7$ GeV includes only Λ hyperon. This P_Λ value still follows the global increasing trend [111]. The other STAR result at $\sqrt{s_{\mathrm{NN}}} = 3$ GeV shows the Λ polarization $P_\Lambda = 4.91 \pm 0.81$(stat.) ± 0.15(syst)% that is the largest global Λ polarization yet observed at STAR, see Fig. 3.11 [110].

The new preliminary results from the HADES experiment at GSI for Au-Au and Ag-Ag collisions at $\sqrt{s_{\mathrm{NN}}} = 2.55$ GeV and $\sqrt{s_{\mathrm{NN}}} = 2.4$ GeV, respectively, show also

relatively high Λ polarization but with large uncertainty [112]. They are presented as orange and green diamonds in Fig. 3.10.
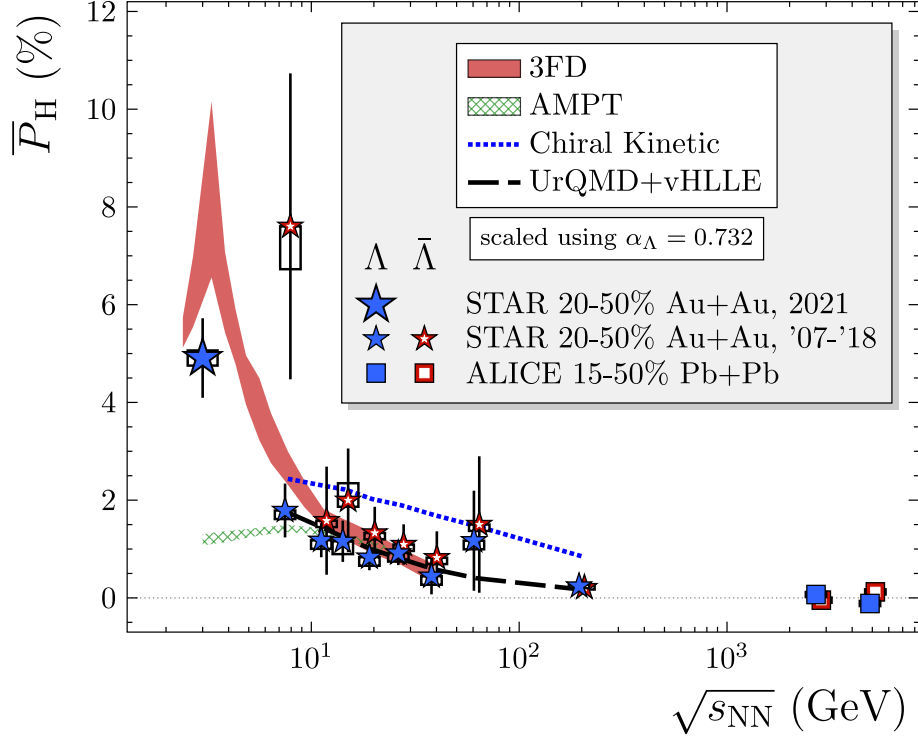
Figure 3.11: Global Λ and Λ polarization P_{H} in HI collisions as a function of collision energy $\sqrt{s_{\mathrm{NN}}}$ including the results from various theoretical models [110].

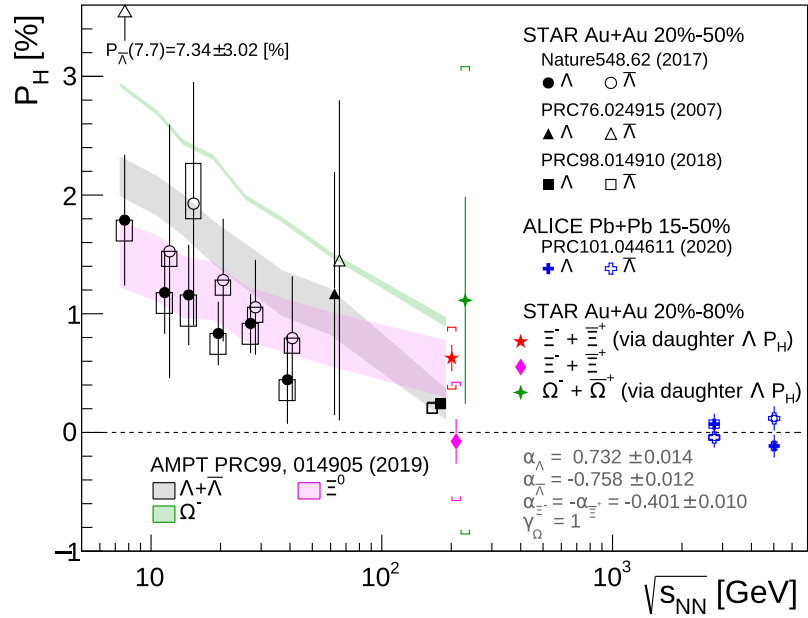Figure 3.12: Global polarization of various hyperons P_{H} in HI collisions as a function of collision energy $\sqrt{s_{\mathrm{NN}}}$ including the results of the AMPT model calculation [112].

The first polarization measurement including Ξ and Ω hyperons at $\sqrt{s_{\mathrm{NN}}} = 200$ GeV

from the STAR experiment is presented in Fig. 3.12 where for both hyperons, the results for particles and antiparticles are averaged so that the statistical uncertainty was reduced. It was found that the P_Ξ is slightly larger than the related Λ polarization which is in agreement with a multiphase transport model (AMPT) [112].
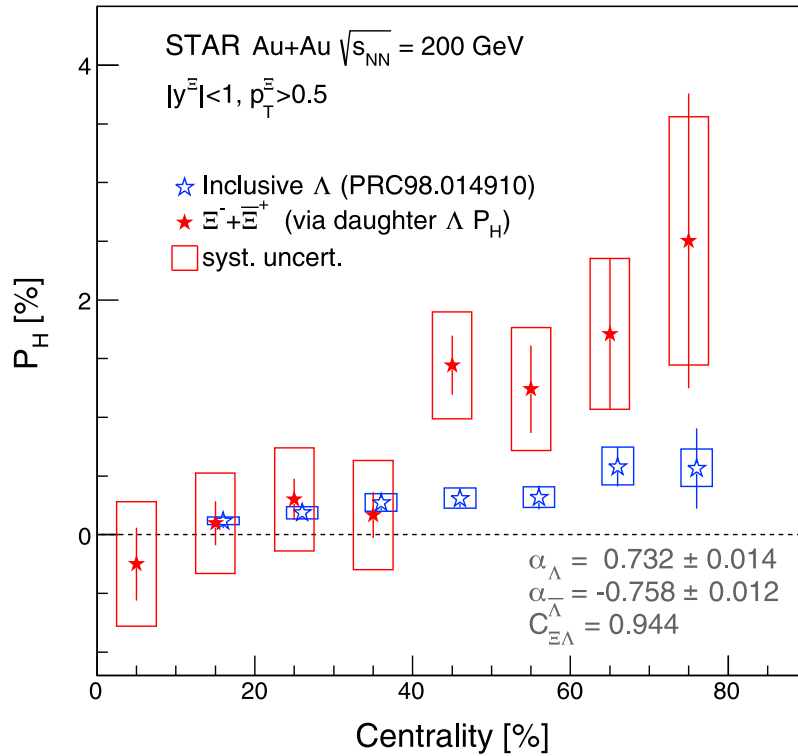
Figure 3.13: Global Λ and Ξ hyperons polarization in HI collisions at $\sqrt{s_{\mathrm{NN}}} = 200$ GeV as a function of the collision centrality [112].

The centrality dependence of the global hyperon polarization can be seen in Fig. 3.13 where the inclusive Λ means that non-primary Λs are considered as well. The hyperon polarization increases for the more peripheral collision which is expected because of the centrality dependence of the fluid velocity. Similar to the energy dependence, the Ξ polarization is there slightly larger, although to make clear conclusions, one would need lower uncertainties of the measurement [112].

Chapter 4

Global polarization of hyperons in hydrodynamic simulations

In this chapter, the hydrodynamic approach of the QGP evolution and hyperon polarization in the HI collision is discussed including various models and their short descriptions.

4.1 Hydrodynamic model of heavy-ion collisions

The observation of significant elliptic flow in HI collision described by flow coefficient v_2, see Chapter 1.3.3, was a sign of hydrodynamic behavior of the created medium. Therefore, as the first approach, ideal hydrodynamics not including viscous effect was used for description of HI collisions and it turned out to be successful. The even better description of experimental data was provided by viscous hydrodynamics with a low shear viscosity to entropy density η/s ratio. The hydrodynamics can be applied only if a mean free path is short with respect to the size of the system. Hence, it is expected that strongly interacting QGP should be a nearly perfect fluid [113].

Assuming ideal non-viscous fluid, the system evolution in relativistic HI meet 5 conservation equations including energy, momentum and charge conservation. In summary, they can be expressed as

$$\partial_\mu T_{\mathrm{id}}^{\mu\nu} = 0, \tag{4.1}$$

$$\partial_\mu J_B^\mu = 0, \tag{4.2}$$

where T_{id} and J_B^μ are the energy-momentum tensor and the net baryon current, respectively described as

$$T_{\mathrm{id}}^{\mu\nu} = (\varepsilon + p)u^\mu u^\nu - pg^{\mu\nu}, \tag{4.3}$$

$$J_B^\mu = \rho_B u^\mu, \tag{4.4}$$

where ε is the energy density, p is the pressure, ρ_b is the baryon density and $g^{\mu\nu}$ is

the metric tensor having the following form

$$g^{\mu\nu} = \begin{pmatrix} 1 & 0 & 0 & 0 \\ 0 & -1 & 0 & 0 \\ 0 & 0 & -1 & 0 \\ 0 & 0 & 0 & -1 \end{pmatrix},$$ (4.5)

and u^μ is the time-like flow four-vector defined as

$$u^\mu = \frac{1}{\sqrt{1 - v^2}} \left(1, v_x, v_y, v_z\right),$$ (4.6)

where $\vec{v}$ is the velocity. In order to connect the observables ε, p and ρ_B, the equation of state (EoS) of the general form is needed

$$p = p(\varepsilon, \rho_B).$$ (4.7)

For a purpose of further calculations, two directions are chosen (along u^μ and perpendicular to u^μ). The projector to the space which is perpendicular to flow four-vector u^μ has the following form

$$\Delta^{\mu\nu} = g^{\mu\nu} - u^\mu u^\nu.$$ (4.8)

Since $\Delta^{\mu\nu}$ is perpendicular to u^μ, it can be shown that

$$\Delta^{\mu\nu} u^\nu = g^{\mu\nu} u_\nu - u^\mu u^\nu u_\nu = u^\mu - u^\mu \overbrace{\frac{1 - v^2}{1 - v^2}}^{u^\nu u_\nu = 1} = 0.$$ (4.9)

Using the above-mentioned projections, the conservation of the energy-momentum tensor $T_{\text{id}}^{\mu\nu}$ in Eq. (4.3) can be divided into two directions as follows

$$u_\mu \partial_\nu T_{\text{id}}^{\mu\nu} = u_\mu \partial_\nu \varepsilon + (\varepsilon + p)\partial_\nu u^\nu = 0,$$ (4.10)
$$\Delta^\alpha_{\ \mu} \partial_\nu T_{\text{id}}^{\mu\nu} = (\varepsilon + p)u^\nu \partial_\nu u^\alpha - \Delta^{\alpha\nu} \partial_\nu p = 0,$$ (4.11)

which may be helpful for analytical calculations of hydrodynamic equations.

The first order Navier-Stokes formalism describing vicous hydrodynamics introduces stress-energy tensor as

$$T_{\text{1st}}^{\mu\nu} = T_{\text{id}}^{\mu\nu} + S^{\mu\nu},$$ (4.12)

where the second term $S^{\mu\nu}$ is the viscous part defined as

$$S^{\mu\nu} = \eta \left(\nabla^\mu u^\nu + \nabla^\nu u^\mu - \frac{2}{3} \nabla^{\mu\nu} \Delta_\alpha u^\alpha \right),$$ (4.13)

where η is the shear viscosity and $\nabla^\mu = \Delta^{\mu\nu} \partial_\nu$ the local spatial derivative. In addition, the viscous part $S^{\mu\nu}$ is perpendicular to the flow four-vector u^μ because of the $\Delta^{\mu\nu}$ term. The Navier-Stokes formalism is simple but at the cost of the unphysical superluminal signals which are numerically unstable [113].

A way to avoid the unphysical phenomena is to introduce second-order Israel-Stewart formalism. In this formalism, the stress-energy tensor is decomposed as

$$T_{\text{2nd}}^{\mu\nu} = T_{\text{id}}^{\mu\nu} + \pi^{\mu\nu}.$$ (4.14)

The evolution equations have form

$$\partial_\mu T_{2nd}^{\mu\nu} = 0, \tag{4.15}$$

$$\Delta^\mu_{\ \alpha} \Delta^\nu_{\ \beta} u^\sigma \partial_\sigma \pi^{\alpha\beta} = -\frac{1}{\tau_\pi}(\pi^{\mu\nu} - S^{\mu\nu}) - \frac{4}{3}\pi^{\mu\nu}(\partial_\alpha u^\alpha), \tag{4.16}$$

where for sake of simplicity terms including heat-flow, vorticity and numerically irrelevant contributions are neglected and τ_π is the relaxation time [113].

4.2 Hydrodynamic hybrid model

The evolution of the hot dense matter from the time of the collision to the time of kinetic freeze-out is currently often described by the so-called hybrid models. The main advantage of these models is that each stage of the medium expansion is described by a different model for which it is most accurate. The partonic matter in the early stage of expansion (initial condition - IC) is described by means of ideal or dissipative fluid dynamics. On the other hand, the dilute later stage after particle hadronization is described by a hadronic transport model (such as UrQMD, RQMD or JAM) [114]. The general stages of the hybrid model are depicted in Fig. 4.1. It turned out that it is easier to compare the hybrid model with the measured data providing that the particle ensemble event by event and then analyze the ensemble similar to the real data [115].
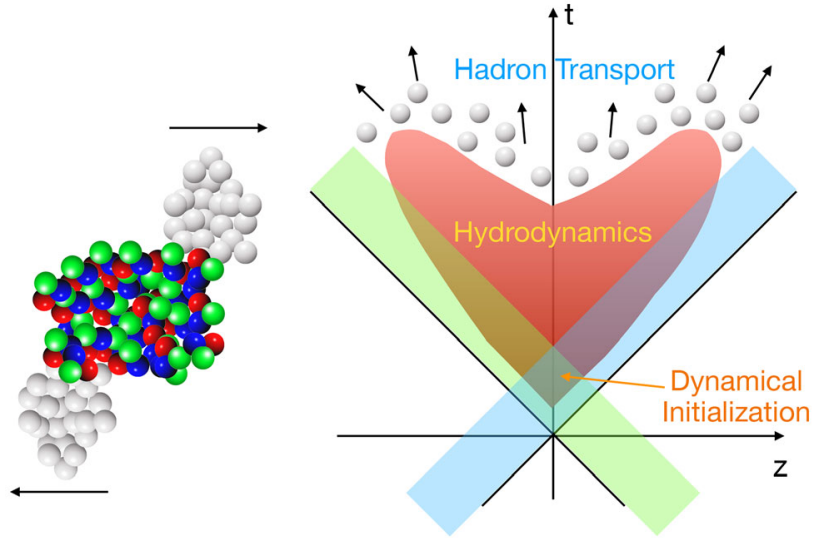
Figure 4.1: Illustration of relativistic HI collision at intermediate collision energy where the stages of the hybrid model are pointed out [116].

Nevertheless, the challenging part of the hybrid is the connection between two different approaches because each of them includes different degrees of freedom. In current practice, the hybrids models solve fluid dynamics regardless of the boundary condition provided by cascade models. As the boundary condition is taken vacuum at infinity. The point when fluid dynamical is switched to the transport model is

chosen a posteriori when the fluid evolution is completed. The switching surface usually meets conditions of constant temperature T, energy density ε, or time t. The distributions of particles on the switching surface Σ are computed via the Cooper-Frye formula given by

$$E\frac{\mathrm{d}^3N}{\mathrm{d}p^3} = \int_\Sigma \mathrm{d}\Sigma_\mu p^\mu f(x, p), \qquad (4.17)$$

where E is the energy, p^μ the momentum, $f(x, p)$ is the distribution function and the normal of the surface $\mathrm{d}\Sigma_\mu$ for known analytic expression has form

$$\mathrm{d}\Sigma_\mu = \varepsilon_{\mu\alpha\beta\gamma}\frac{\partial x^\alpha}{\partial a}\frac{\partial x^\beta}{\partial b}\frac{\partial x^\gamma}{\partial c}\mathrm{d}a\mathrm{d}b\mathrm{d}c. \qquad (4.18)$$

It should be noted that particlization (i.e. creation of particles from fluid in the hybrid model) does not correspond to freeze-out because, as has been already mentioned, after the (thermal) freeze-out there are no inelastic, not even elastic collisions. There can only occur decays of resonances. Therefore, the transport stage comprising the resonance decays has to be implemented. Moreover, there is no clear point of hadronization because of the crossover. Thus the switching surface is often chosen at the stage when the hadronization is completed [114]. As examples of hybrid models can be mentioned [117]:

- UrQMD hybrid [118]

    - IC: UrQMD cascade
    - Hydro: ideal 3+1D, SHASTA

- Skokov-Toneev hybrid [119]

    - IC: Quark-Gluon-String-Model
    - Hydro: ideal 3+1D, SHASTA

- Karpenko et. al. hybrid [120]

    - IC: UrQMD cascade
    - Hydro: viscous 3+1D

- Pang et. al. hybrid [121]

    - IC: AMPT
    - Hydro: ideal 3+1D, SHASTA

- SMASH-vHLLE hybrid [122]

    - IC: SMASH
    - Hydro: viscous 3+1D

4.2.1 SMASH

For the purpose of generating the initial state or the hadronic rescattering stage, the model Simulating Many Accelerated Strongly-Interacting Hadrons (SMASH) can be employed. SMASH is able to find a solution of the non-equilibrium dynamics of hadron considering inelastic interactions via the relativistic Boltzmann equation

$$p^\mu \partial_\mu f_i(x,p) + m_i F^\alpha \partial^p_\alpha f_i(x,p) = C^i_{\text{coll}}, \tag{4.19}$$

where $f_i(x,p)$ is the particle distribution, m_i is the particle mass, F^α is the force different for individual particle, and C^i_{coll} is the collision term [123].

Regarding the initial condition, the phase-space distribution of the collided nucleons has to be sampled. In the case of most rounded nuclei (Au or Pb), the position of nuclei is generated via Woods-Saxon distribution given by

$$\frac{\text{d}^3 N}{\text{d}r^3} = \frac{\rho_0}{\exp\left(\frac{r-r_0}{d}\right) + 1}, \tag{4.20}$$

where r is the radius, d is the nucleus diffusiveness and ρ_0 is the nuclear ground state density. Then, the nucleons in the momentum space get Fermi momenta and are boosted in the z direction. After that, the nucleons are propagated along straight lines and collide with each other. This is performed step-by-step in a grid [123]. Conditions of the initial state generated by SMASH are taken out on hypersurface Σ at proper time τ_0 defined as

$$\tau_0 = \frac{R_p + R_t}{\sqrt{\left(\frac{\sqrt{s_{\text{NN}}}}{2m_{\text{N}}}\right)^2 - 1}}, \tag{4.21}$$

where R_p and R_t correspond to the radii of the projective and target nucleus, respectively, $\sqrt{s_{\text{NN}}}$ is the collision energy and m_{N} is the mass of nucleon. At this time τ_0, the nuclei should have already passed through each other which can be assumed as the suitable time when the local equilibrium occurs. The SMASH evolution includes all scattering and particle interaction before the τ_0-hypersurface is reached. Particles that have crossed the hypersurface are taken out from the evolution and prepared for the possible further hydrodynamical evolution [122].

After particlization, SMASH can be used to perform non-equilibrium hadronic afterburner for particle evolution. First, the particles from the particlization are propagated backward in time to the moment of the hadronization of the first particle. Then, the particles free stream until they have reached their time of formation [122].

4.2.2 GLISSANDO

Alternatively, the initial condition can be provided by the GLauber Initial-State Simulation AND mOre (GLISSANDO) which is a Monte-Carlo generator for Glauber-like models describing the initial stage of relativistic HI collisions [124]. The simulated events can be divided into three stages. In the first one, positions of nucleons in the

nuclei are generated via radial nuclear density distribution similarly as in the previous case in SMASH. Then the CMS of nuclei are moved by the impact parameter b. In the next stage, transverse positions of sources[1] with their relative deposited strength (RDS) are generated. If the nucleons are considered as a hard-sphere, a nucleon is labeled wounded if its center passes in the transverse plane close to the center of another nucleon. This wounding distance r_0 is described as

$$r_0 = \sqrt{\frac{\sigma_w}{\pi}}, \qquad (4.22)$$

where σ_w describes the NN inelastic cross section for a collision energy $\sqrt{s_{\mathrm{NN}}}$. For instance[2], $\sigma_w = 42$ mb at the RHIC energy of $\sqrt{s_{\mathrm{NN}}} = 200$ GeV. The same description is applied to a binary collision. Thus for the hard-sphere nucleons, binary collisions have the same inelastic cross-sections as wounded nucleons. In the final stage, event-by-event averaged observables, profile of a fireball and their harmonic decomposition are calculated [125].

The GLISSANDO 2 version includes additional features, such as parametrization of the shape for all typical nuclei, the inclusion of the colliding nuclei deformation, possibility of choosing a correlated distribution of nucleons in nuclei and much more [124]. Currently, the newest extended version is GLISSANDO 3 including new features such as implementation of wounded quark model, possibility of colliding light nuclei (^{3}He and ^{3}H) or possibility of studying proton fluctuations [126].

4.2.3 vHLLE

Quark-gluon and hadron matter can be simulated by a 3+1 dimensional viscous hydrodynamic code for relativistic HI collisions. The vHLLE model is based on the Godunov-type relativistic Harten-Lax-van Leer-Einfeldt (HLLE) Riemann solver. The relativistic viscous hydrodynamic equations are solved in the Israel-Stewart framework [127].

The hydrodynamic simulations are performed in Milne coordinates for the $t - z$ plane in spacetime, i.e. x, y,$\tau = \sqrt{t^2 - z^2}$, $\eta = 1/2 \ln[(t + z)/(t - z)]$ in which case x, y, z and t are Minkowski coordinates. Next, the metric tensor in Milne coordinates has form

$$g^{\mu\nu} = \begin{pmatrix} 1 & 0 & 0 & 0 \\ 0 & -1 & 0 & 0 \\ 0 & 0 & -1 & 0 \\ 0 & 0 & 0 & -1/\tau^2 \end{pmatrix}. \qquad (4.23)$$

These coordinates lead to the following hydrodynamic equations

$$\partial_\nu T^{\tau\nu} + \tau T^{\nu\nu} + \frac{1}{\tau} T^{\tau\tau} = 0, \qquad \partial_\nu T^{x\nu} + \frac{1}{\tau} T^{x\tau} = 0 \qquad \partial_\nu T^{y\nu} + \frac{1}{\tau} T^{y\tau} = 0,$$

$$\partial_\nu T^{\eta\nu} + \frac{3}{\tau} T^{\eta\tau} = 0, \qquad \partial_\nu J_c^\nu + \frac{1}{\tau} J_c^\tau = 0, \qquad (4.24)$$

---

[1]As a source are considered wounded nucleons and binary collisions.
[2]1 mb = 0.1 fm^2

where J_c is the charge current. However, the numerical solution of Eq. (4.24) would require higher-order numerical time integration method. Therefore, the variables in Milne coordinates are redefined as follows

$$T^{\mu\nu} = \tilde{T}^{\mu\nu} \quad \text{for } \mu, \nu \neq \eta, \qquad\qquad T^{\mu\eta} = \frac{\tilde{T}^{\mu\eta}}{\tau} \quad \text{for } \mu \neq \eta,$$

$$T^{\eta\eta} = \frac{\tilde{T}^{\eta\eta}}{\tau^2}, \qquad\qquad\qquad\qquad J_c^\eta = \frac{\tilde{J}^\eta}{\tau}. \qquad (4.25)$$

Similarly, the shear stress tensor $\pi^{\mu\nu}$ and four-velocity u^μ are rewritten by separating the $1/\tau$ factor:

$$\pi^{\mu\eta} = \frac{\tilde{\pi}^{\mu\eta}}{\tau}, \qquad\qquad\qquad\qquad \pi^{\eta\eta} = \frac{\tilde{\pi}^{\eta\eta}}{\tau^2},$$

$$u^\eta = \frac{\tilde{u}^\eta}{\tau}, \qquad\qquad\qquad\qquad \partial_\eta \rightarrow \frac{1}{\tau}\partial_\eta. \qquad (4.26)$$

The changed hydrodynamic equations are then more suitable for the numerical solution which is performed via a finite volume method. In this method, space is discretized and the averaged values of the energy-momentum tensor $T^{\tau\mu}$ are considered in the mesh [127]. Example of the separating of fluid into cells is depicted in Fig. 4.2.
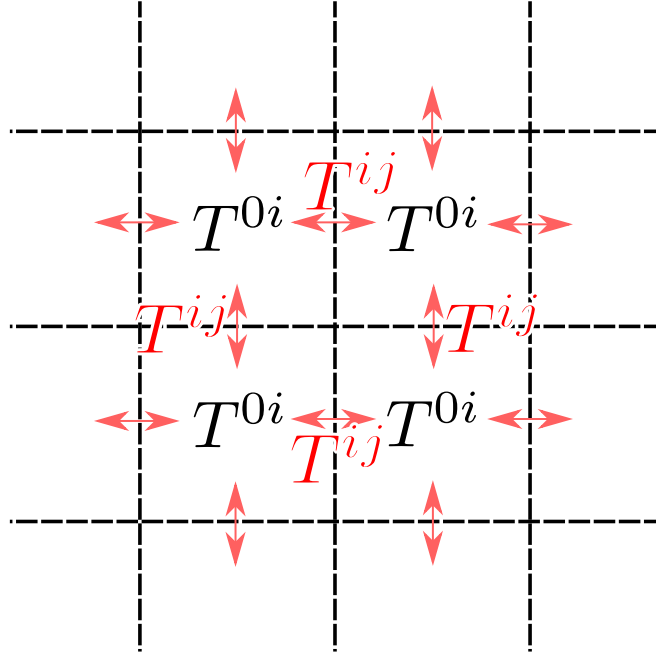

Figure 4.2: Visualization of spatial grid for the finite volume method.

4.3 Hyperon polarization in hydrodynamic model

Expectation of the global polarization of hyperon with respect to the direction of angular momentum is based on the idea that the polarization of quarks in

the QGP is transferred to hadrons. Hence, it may be theoretically possible to predict the polarization of created hadrons. The main assumption for that is the local thermodynamical equilibrium of the spin degrees of freedom at the stage of hadronization, similarly to the momentum degrees of freedom. Simply put, the Cooper-Frye formula has to be extended to the spin of particles [10].

The relativistic extension of the fluid vorticity defined in Eq. (3.2) can be introduced in different ways. However, for purpose of the spin polarization, most convenient is thermal vorticity tensor ϖ given by

$$\varpi_{\mu\nu} = -\frac{1}{2}(\partial_\mu \beta_\nu - \partial_\nu \beta_\mu) \tag{4.27}$$

with four-temperature field,

$$\beta^\mu = \frac{1}{T}u^\mu, \tag{4.28}$$

where T is the proper temperature [10],[11].

In general, the adimensional spin four-vector S^μ can be obtained as follows

$$\hat{S}^\mu = \frac{1}{m}\hat{W}^\mu, \tag{4.29}$$

where $\hat{W}^\mu$ is so-called Pauli-Lubanski vector operator given by

$$\hat{W}^\mu = -\frac{1}{2}\varepsilon^{\mu\nu\rho\sigma}\hat{J}_{\nu\rho}\hat{P}_\sigma, \tag{4.30}$$

where $\hat{J}_{\nu\rho}$ is the angular momentum-boost operators and $\hat{P}_\sigma$ is the four-momentum operator. The mean spin vector S^μ denotes the quantum and thermal average of $\hat{S}^\mu$ as follows

$$S^\mu = \text{tr}\left(\hat{\rho}\hat{S}^\mu\right), \tag{4.31}$$

where $\hat{\rho}$ is the related density operator. Considering the above-mentioned assumption, the mean spin four-vector of particle with spin s^3, mass m and momentum p at position x is

$$S_\varpi^\mu(x,p) = -\frac{s(s+1)}{6m}\left[1 - f(x,p)\right]\varepsilon^{\mu\nu\rho\sigma}p_\sigma\varpi_{\nu\rho} + \mathcal{O}(\varpi)^2, \tag{4.32}$$

where $f(x,p)$ is the Fermi-Dirac distribution. In Eq. (4.32), if the higher terms are neglected, the position x can be marginalized out as follows

$$S_\varpi^\mu(p) = -\frac{s(s+1)}{6m}\frac{\int_\Sigma \mathrm{d}\Sigma_\lambda p^\lambda f(x,p)\left[1 - f(x,p)\right]\varepsilon^{\mu\nu\rho\sigma}p_\sigma\varpi_{\nu\rho}}{\int_\Sigma \mathrm{d}\Sigma_\lambda p^\lambda f(x,p)}, \tag{4.33}$$

where Σ is the particlization hypersurface.

Now, the considered hyperon is Λ with spin $s = 1/2$. It was shown that the global spin polarization of Λ hyperon from the model, which is integrated over all momenta,

---

[3]The considered particles are fermions, thus the spin s has to meet condition $2s = 2n + 1$ where $n \in \mathbb{N}^0$.

describes the measurements [128]. Nevertheless, the dependence of the polarization on the momentum (local polarization) is not in agreement with the data. More precisely, the predicted longitudinal component of the spin polarization together with the trend of the component which is perpendicular to the reaction plane with respect to the azimuthal angle is opposite to the measured data. One of the possible sources of this problem was the neglected $\mathcal{O}(\varpi)^2$ and higher terms however it was refuted [128].
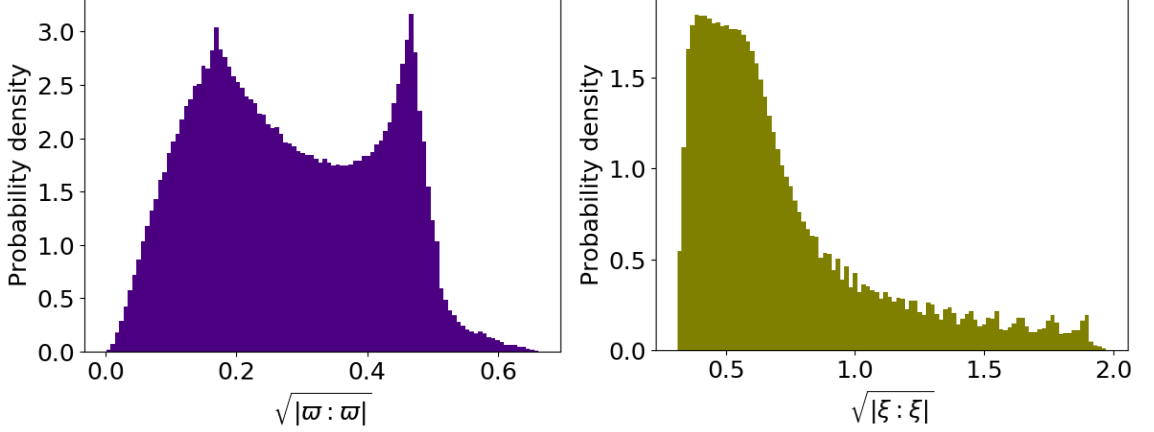

Figure 4.3: Distributions of the thermal vorticity $\sqrt{|\varpi : \varpi|}$ (left) and thermal shear $\sqrt{|\xi : \xi|}$ (right) at decoupling surface for a temperature $T = 165$ MeV for HI collision with impact parameter $b = 9.2$ fm at energy $\sqrt{s_{\mathrm{NN}}} = 200$ GeV [128].

Lately, additional contribution to spin polarization vector at local equilibrium was observed. Contrary to the above-mentioned contribution $S_{\varpi}^{\mu}(p)$ related to the thermal vorticity tensor ϖ, the new observed contribution is described by means of thermal shear tensor given by

$$\xi_{\mu\nu} = \frac{1}{2}(\partial_{\mu}\beta_{\nu} + \partial_{\nu}\beta_{\mu}). \tag{4.34}$$

The related mean spin four-vector is

$$S_{\xi}^{\mu}(p) = -\frac{1}{4m}\varepsilon^{\mu\rho\sigma\tau}\frac{p_{\tau}p^{\lambda}}{\epsilon}\frac{\int_{\Sigma} \mathrm{d}\Sigma_{\lambda}p^{\lambda}f(x,p)\left[1 - f(x,p)\right]\hat{t}_{\rho}\xi_{\sigma\lambda}}{\int_{\Sigma} \mathrm{d}\Sigma_{\lambda}p^{\lambda}f(x,p)}, \tag{4.35}$$

where $\epsilon = \sqrt{m^2 + \vec{p}^2}$ and $\hat{t}$ is the time direction in the CMS or QGP frame. The additional term in Eq. (4.35) is a purely local equilibrium as well and its contribution is significant with respect to the previous one in Eq. (4.33), as can be seen in Fig. 4.3.

The hypersurface Σ in Eq. (4.33) and (4.35) should be close to local thermodynamical equilibrium and also it should be the decoupling surface so that the hadronic effective fields could be quasi-free [128]. One may ask whether the applied approximations are the best possible for relativistic HI collisions at high energies. Actually, there is a way to improve the approximation owing to the expectation of the decoupling at constant temperature T. If Σ is an isothermal hypersurface, the temperature T included in Eq. (4.28) can be factored out of integral in the Local thermodynamical

Equilibrium (LE) density operator $\hat{\rho}_{\text{LE}}$ as follows

$$\hat{\rho}_{\text{LE}} = \frac{1}{Z_{\text{LE}}} \exp\left[-\frac{1}{T} \int_{\Sigma} d\Sigma_{\mu} \hat{T}^{\mu\nu} u_{\nu}\right], \tag{4.36}$$

where Z_{LE} is the related partition function. Then the four-velocity u can be expanded in a Taylor series which contrary to T is not constant over Σ. The expansion takes form

$$u_{\nu}(y) \approx u_{\nu}(x) + \partial_{\lambda} u_{\nu}(x)(y-x)^{\lambda}. \tag{4.37}$$

Hence, one gets

$$\hat{\rho}_{\text{LE}} \approx \frac{1}{Z_{\text{LE}}} \exp\left[-\beta_{\nu} \hat{P}^{\nu} - \frac{1}{T} \partial_{\lambda} u_{\nu}(x) \int_{\Sigma} d\Sigma_{\mu}(y)(y-x)^{\lambda} \hat{T}^{\mu\nu}(y)\right]. \tag{4.38}$$

If the constant temperature T would not be assumed, the density operator was given by

$$\hat{\rho}_{\text{LE}} \approx \frac{1}{Z_{\text{LE}}} \exp\left\{-\beta(x) \cdot \hat{P} - \left[\frac{1}{T} \partial_{\lambda} u_{\nu}(x) + u_{\nu} \partial_{\lambda} \left(\frac{1}{T}\right)\right] \int_{\Sigma} d\Sigma_{\mu}(y)(y-x)^{\lambda} \hat{T}^{\mu\nu}(y)\right\}, \tag{4.39}$$

where the additional gradient of temperature is present. Nevertheless, it should be noted that the temperature gradient ∂T is perpendicular to the hypersurface. Therefore, the temperature gradient in Eq. (4.39) is still present even though the temperature T is constant at the hypersurface Σ thereby it can eventually contribute to the spin polarization vectors S^{μ}_{ϖ} and S^{μ}_{ξ}. However, it was shown that for the purpose of the integration of function being constant over the space-time sub-manifold (in this case 3D hypersurface) the better approximation is Eq. (4.38) [128].

In order to introduce the approximated density operator in Eq. (4.38), the gradient $\partial\beta$ is simply replaced as follows

$$\partial\beta \to \frac{1}{T_{\text{dec}}} \partial u, \tag{4.40}$$

where T_{dec} represents the constant decoupling temperature. This replacement causes that the spin polarization vector for baryon with spin $1/2$ is changed to isothermal local equilibrium (ILE) form:

$$S^{\mu}_{\text{ILE}}(p) = -\varepsilon^{\mu\rho\sigma\tau} p_{\tau} \frac{\int_{\Sigma} d\Sigma_{\lambda} p^{\lambda} f(x,p)(1-f(x,p))\left[\omega_{\rho\sigma} + 2\hat{t}_{\rho} \frac{p^{\lambda}}{\epsilon} \Xi_{\lambda\sigma}\right]}{8mT_{\text{dec}} \int_{\Sigma} d\Sigma_{\lambda} p^{\lambda} f(x,p)} \tag{4.41}$$

with the kinematic vorticity

$$\omega_{\rho\sigma} = \frac{1}{2}(\partial_{\sigma} u_{\rho} - \partial_{\rho} u_{\sigma}) \tag{4.42}$$

and the kinematic shear tensor

$$\Xi_{\rho\sigma} = \frac{1}{2}(\partial_{\sigma} u_{\rho} + \partial_{\rho} u_{\sigma}). \tag{4.43}$$

68

One should keep in mind that

$$S^\mu_{\text{ILE}}(p) \neq S^\mu_\varpi(p) + S^\mu_\xi(p). \qquad (4.44)$$

This fact was confirmed by means of numerical model, see Fig. 4.4 where the rest frame polarization vector $\vec{P} = 2\vec{S}_*$ is depicted.
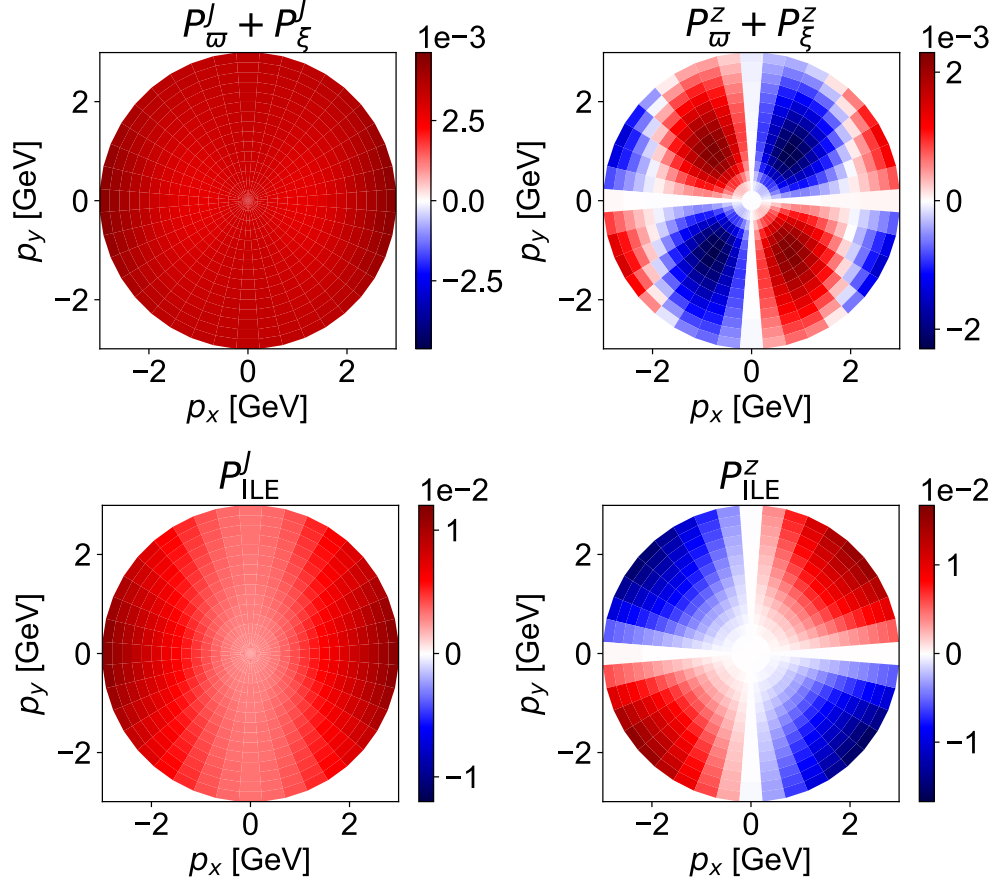
Figure 4.4: Components of Λ polarization at mid-rapidity with respect to its transverse momentum p_{T}, computed by vHLLE for Au-Au collisions at $\sqrt{s_{\text{NN}}} = 200$ GeV with centrality $20 - 60\%$. The upper panels show the sum of $P^{J,z}_\varpi(p)$ and $P^{J,z}_\xi(p)$ and the lower ones show $P^{J,z}_{\text{ILE}}(p)$ where J and z stand for the angular momentum and the beam axis direction, respectively [128].

Chapter 5

Dataset and Lambda hyperon reconstruction

In this chapter, the data set and its analysis are described. In order to compute the global polarization of Λ and $\overline{\Lambda}$ polarization, it is necessary to reconstruct the even plane of a collision including its resolution, reconstruct the Λ and $\overline{\Lambda}$ using Kalman Filter, obtain the daughter baryon angular distribution, boost it to the rest frame of the mother particle and obtain the angular distribution with respect to the reconstructed event plane.

5.1 Dataset

The data used for this analysis are from Au-Au collisions at $\sqrt{s_{\mathrm{NN}}} = 27$ GeV from the STAR experiment. The dataset was collected in 2018 with production tag P19ib [129]. The used library to process the dataset is TFG22a which is the abbrevation of Tracking Focus Group (TFG), 22 denotes the year 2022 and the last letter a describes the version. The number of events in the dataset is $N_e = 8.947 \cdot 10^8$. The events are divided into 9 centrality bins denoted as (C_{ID}) that are associated with centrality ranges C as it is gathered in Tab. 5.1.

The chosen decay channels for the Λ and $\overline{\Lambda}$ reconstruction are $\Lambda \to p + \pi^-$ and $\overline{\Lambda} \to \overline{p} + \pi^+$ due to non-zero electric charge of the daughter baryons and relatively high branching ratio $(63.9 \pm 0.5)\%$ [84].

C_{ID}	0	1	2	3	4	5	6	7	8
C [%]	70-80	60-70	50-60	40-50	30-40	20-30	10-20	5-10	0-5

Table 5.1: Centrality bins C_{ID} and the related centrality ranges C.

5.2 Kalman filter

The Kalman filter (KF) is a method that is used for the optimal estimation of particle traces in a detector. It is named after Hungarian scientist Rudolf Emil Kálmán [130]. In short, the KF performs estimation of the traces and after that, they are filtered.

In the first step, the state vector $\vec{r}$ given by

$$\vec{r} = (x, y, z, p_x, p_y, p_z, E), \tag{5.1}$$

where $\vec{x} = (x, y, z)$ is the position vector, $\vec{p} = (p_x, p_y, p_z)$ is the momentum vector, and E is the energy, is extrapolated to the subsequent k-th detector level. In the first surface, the state vector is denoted as $\vec{r}_0$ and the covariance matrix $\mathbb{C}_0$ is chosen as

$$\mathbb{C}_0 = \mathbb{I} \cdot A, \tag{5.2}$$

where $\mathbb{I}$ is an identity matrix of dimension $\dim(\vec{r})$ and A is an arbitrary large positive number. The covariance matrix of the state vector $\vec{r}$ given by

$$(\mathbb{C}_k)_{ij} = \mathrm{Cov}[(r_k)_i, (r_k)_j]. \tag{5.3}$$

The state vector between k-th and $(k+1)$-th surface is generally changed as follows

$$\vec{r}_{k+1} = \mathbb{A}_{k+1}\vec{r}_k + \vec{\eta}_{k+1}, \tag{5.4}$$

where matrix $\mathbb{A}_k$ (extrapolator) represents a linear function[1] describing evolution of the state vector and $\vec{\eta}_k$ is the process noise and background signal of the measurement. Assuming that the process noise is unbiased, the vector $\vec{\eta}_k$ meets condition

$$\langle \vec{\eta}_k \rangle = 0, \tag{5.5}$$

where the angle brackets $\langle \dots \rangle$ represent a mean value. The related covariance matrix of the noise $\mathbb{Q}_k$ is given by

$$(\mathbb{Q}_k)_{ij} = \mathrm{Cov}[(\eta_k)_i, (\eta_k)_j]. \tag{5.6}$$

The measured value at the surface at k-th step is denoted as a vector $\vec{m}_k$. It should be noted that $\dim(\vec{m}_k) \leq \dim(\vec{r}_k)$, because, for instance, the TPC yields only two position coordinates of a measurement. The initial state vector is used by the algorithm to proceed to the next level surface of a detector. Another assumption is that the vector $\vec{m}_k$ can be written by means of the state vector as follows

$$\vec{m}_k = \mathbb{H}_k\vec{r}_k + \vec{v}_k, \tag{5.7}$$

where the function $\mathbb{H}_k$ is a $\dim(\vec{m}_k) \times \dim(\vec{r}_k)$ matrix and the vector $\vec{v}_k$ represents measurement noise. Similarly to the noise vector $\vec{\eta}_k$, it meets condition

$$\langle \vec{v}_k \rangle = 0 \tag{5.8}$$

---

[1]However, one can also consider a nonlinear evolution where instead of $\mathbb{A}_k$ a nonlinear function $\phi_k(\vec{r}_k)$ is written.

and the related covariant matrix $\mathbb{V}$ is given by

$$(\mathbb{V}_k)_{ij} = \text{Cov}[(v_k)_i, (v_k)_j]. \tag{5.9}$$

In a case that the initial state vector r_0 is chosen, the next state vector r_1 and the related covariant matrix $\mathbb{C}_1$ is computed as follows

$$\vec{r}_{k+1} = \mathbb{A}_{k+1}\vec{r}_k, \tag{5.10}$$

$$\mathbb{C}_{k+1} = \mathbb{A}_{k+1}\mathbb{C}_k\mathbb{A}_{k+1}^{\text{T}} + \mathbb{Q}_{k+1}. \tag{5.11}$$

The vector $\vec{m}_k$ from a measurement is used to improve the state vector in the following way

$$\tilde{\vec{s}}_k = \vec{s}_k + \mathbb{K}_k(\vec{m}_k - \mathbb{H}_k\vec{s}_k), \tag{5.12}$$

where $\mathbb{K}_k$ is the so-called Kalman gain matrix which can be computed by

$$\mathbb{K}_k = \mathbb{C}_k\mathbb{H}_k^{\text{T}} \left(\mathbb{V}_k + \mathbb{H}_k\mathbb{S}_k\mathbb{H}_k^{\text{T}}\right)^{-1}. \tag{5.13}$$

Then, the algorithm proceeds to the next surface. If it is needed, the KF can perform a "smoothing" of the previously processed data. The smoothing starts with the last processed surface and proceeds recursively backward to the first measurement. The more surfaces are processed, the more accurate is the description of the particle trajectory. An example of the application of KF for a charged particle track in 2D space is depicted in Fig. 5.1. In addition to the above-mention algorithm, there are extended versions of the Kalman filter expecting nonlinear evolution of the state vector [130], [131].
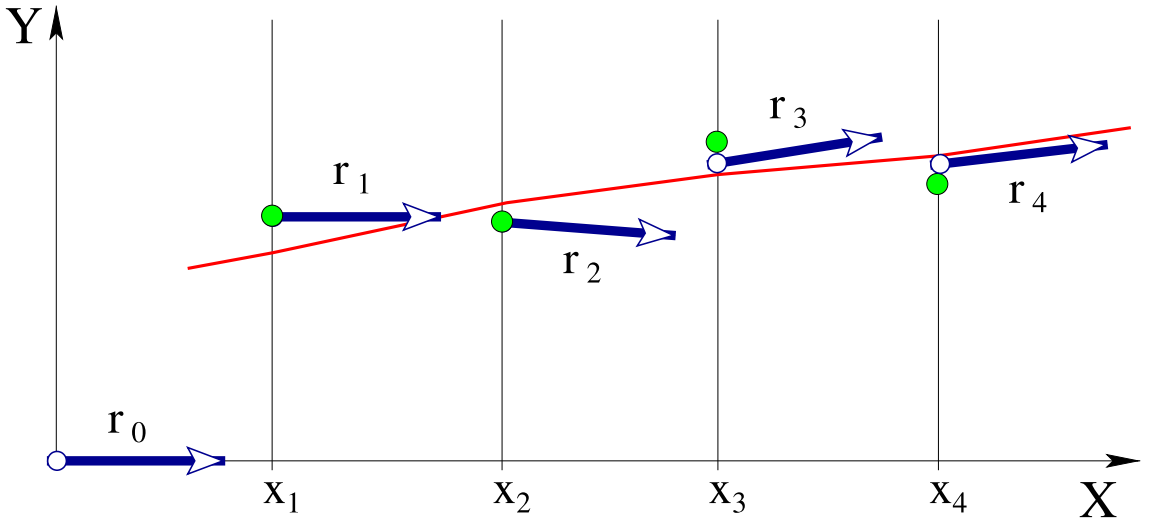

Figure 5.1: Kalman filter: measured values are labeled as green circles, the state vector as white circles and the real particle track as the red curve [131].

The advantages of the Kalman filter and smoothing are [132]:

- Compatible with another prefiltering provided by other method.

- Computation time is proportional to the number of detector surfaces passed by the charged particle.

- An inverse matrix of large matrices is not required.

- The reconstructed track follows the real particle path, it is not an only extrapolation of the initial condition.

- Linearity is required only between the detector surfaces, not over the overall trajectory.

- It provides an optimal track prediction between different kinds of detectors (calorimeters, muon chambers, RICH detectors, etc.).

As a tool for Λ and $\overline{\Lambda}$ reconstruction, the KF Particle Finder (KFPF) package that uses the Kalman filter, can be used. This package was first developed for the purposes of the Compressed Baryonic Matter experiment [133]. Currently, the KFPF package includes over 100 decay channels, cf. Fig. 5.2. In addition, it was successfully adapted to the geometry of the STAR detector. The KPFP package provides a wide range of parameters, for instance particle decay vertex, momentum, energy, mass, lifetime and decay length together with their uncertainties [134], [135].

The KFPF package is written in the ROOT program which ranks among the object-oriented frameworks and is used for data analysis written in C++. It was created for purpose of CERN because the previously used programs (e.g. written in FORTRAN) were not able to process the enormous amount of data [136].
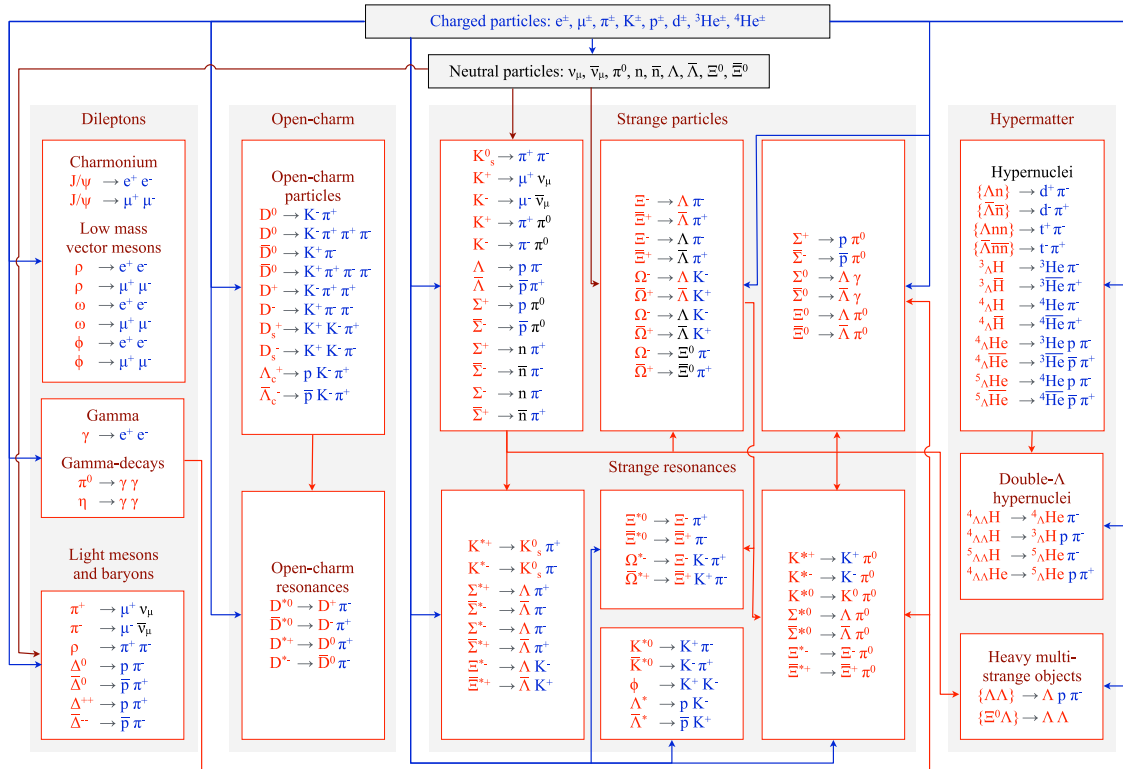

Figure 5.2: Block diagram including all decay channel implemented in KFPF package [134].

5.3 Reconstruction of $\Lambda/\overline{\Lambda}$ via KFPF

The KFPF can reconstruct the neutral particles Λ and $\overline{\Lambda}$ via their daughter baryons (proton) and daughter mesons (pion). However, not all of the reconstructed Λ or $\overline{\Lambda}$ candidates are real Lambdas. The fake Λ and $\overline{\Lambda}$ candidates come mostly from the combinatorial background of random proton-pion pairs which happened to be close together. Because of that, the pair seems like daughter of one particle. In order to minimize the amount of the fake candidates, selection criteria are applied, see Fig. 5.3. The most important topological variables are:[2]

- Proton to pion distance of closest approach (DCA) - maximum DCA between daughters. The shorter proton to pion DCA the more probably the daughters are from the Λ decay.

- Proton/pion DCA - minimum DCA between the daughter particle trajectory and the primary vertex (PV). If the particles are close to the PV, they could be primary or daughters of a different particle with a shorter lifetime.

- Λ DCA - maximum DCA between the reconstructed track of Λ and the PV. Relatively long Λ lifetime resulting in Λ being not a primary particle and so its Λ DCA is longer.

- Λ decay length - minimum distance between the reconstructed decay point of Λ and the PV. The decay point should be displaced from the PV.
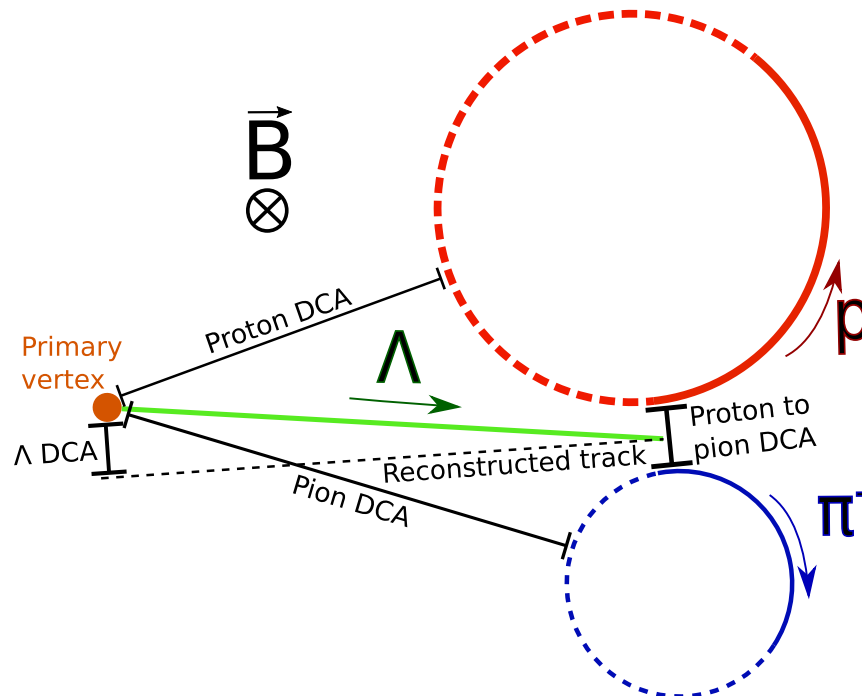

Figure 5.3: Decay of Λ hyperon into proton and pion in magnetic field of detector, various topological variables are pointed out.

---

[2]These variables are described for Λ hyperon reconstruction. They are analogous for $\overline{\Lambda}$.

$d_{\max}$ [cm]	l [cm]	$l/\mathrm{d}l$	χ^2_{fit}	χ^2_{topo}	χ^2_{prim}
<1	>5	>5	<10	<5	>18.6

Table 5.2: Applied selection criteria for Λ and $\overline{\Lambda}$ reconstruction in KFPF. See text for more details.

The applied selection criteria for KFPF are gathered in Tab. 5.2 where:

- d_{max} - maximum proton to pion DCA.

- l - a decay length of the mother particle.

- $\mathrm{d}l$ - uncertainty of the decay length l.

- χ^2_{fit} - χ^2 of a fit of the daughter particle tracks, whereas the chi-squared is defined as

$$\chi^2 = \sum_{i=1}^{n} \left(\frac{x_i - \mu_i}{\sigma_i} \right)^2, \tag{5.14}$$

  where x_i, μ_i, and σ_i represent i-th measured and fitted value, and its standard deviation, respectively.

- χ^2_{topo} - χ^2 of the distance between the Λ production point and the PV.

- χ^2_{prim} is defined as

$$\chi^2_{\mathrm{prim}} = \Delta\vec{r}^{\mathrm{T}} (\mathbb{C}_{\mathrm{track}} + \mathbb{C}_{\mathrm{PV}})^{-1} \Delta\vec{r}, \tag{5.15}$$

  where $\Delta\vec{r}$ denotes difference between the track and the PV position, and $\mathbb{C}_{\mathrm{track}}$ and $\mathbb{C}_{\mathrm{PV}}$ are covariance matrices of the reconstructed track and PV position, respectively.

Despite these selection criteria, still, some amount of the candidates are fake or secondary[3]. Real candidates can be distinguish from the background by means of an invariant mass method.

For this purpose, one plots invariant mass M_{inv} distribution[4]. This distribution is fitted by a double Gaussian distribution given by

$$G(x) = A_1 \exp\left[-\frac{1}{2} \left(\frac{x - \mu_1}{\sigma_1} \right)^2 \right] + A_2 \exp\left[-\frac{1}{2} \left(\frac{x - \mu_2}{\sigma_2} \right)^2 \right], \tag{5.17}$$

---

[3]Secondary particles are the ones that are daughter particles of heavier particles.

[4]Invariant mass of the mother particle can be computed as

$$M_{\mathrm{inv}} = \sqrt{(E_p + E_\pi)^2 - |\vec{p}_p + \vec{p}_\pi|^2}, \tag{5.16}$$

where E and $\vec{p}$ are the energy and momentum of the related daughter particle, respectively.

where $A_{1,2}$ coefficients represent amplitudes, $\mu_{1,2}$ and $\sigma_{1,2}$ are the mean value and the standard deviation of the first and the second Gaussian distribution, respectively. The mean value of the double Gaussian distribution can be derived as follows

$$\mu = \frac{A_1\mu_1\sigma_1 + A_2\mu_2\sigma_2}{A_1\sigma_1 + A_2\sigma_2} \tag{5.18}$$

and the related standard deviation σ is

$$\sigma = \sqrt{\frac{A_1\sigma_1(\sigma_1^2 + \mu_1^2) + A_2\sigma_2(\sigma_2^2 + \mu_2^2)}{A_1\sigma_1 + A_2\sigma_2} - \mu^2}. \tag{5.19}$$
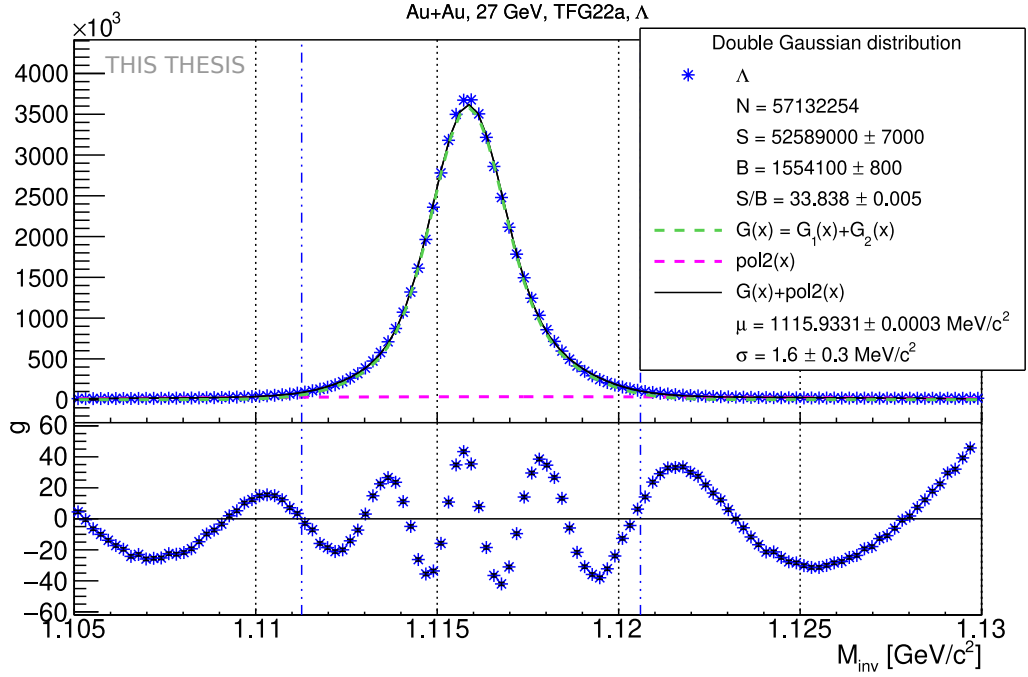

Figure 5.4: The invariant mass distribution M_{inv} of Λ hyperon for $C = 20 - 30\%$ centrality range where N is number of the reconstructed candidates, S is the signal yield, B is the background, S/B is the signal-to-background ratio. See text for more details.

Background distribution is described by the second order polynomial:

$$\mathrm{pol2}(x) = ax^2 + bx + c. \tag{5.20}$$

First, the distribution is fitted by the double Gaussian distribution $G(x)$ in the invariant mass range $M_{\mathrm{inv}} \in (1.105; 1.13)$ GeV/c^2 and the background in the full measured range except the expected peak region $M_{\mathrm{inv}} \in (1.111; 1.123)$ GeV/c^2. The obtained parameters $(A_{1,2}, \mu_{1,2}, \sigma_{1,2}, a, b, c)$ are used as the initial fitting parameter in the final fit where the distribution is fitted by function $G(x) + \mathrm{pol2}(x)$. In this thesis the background yield B is introduced as

$$B = \frac{\int_{\mu-3\sigma}^{\mu+3\sigma} \mathrm{d}x\, \mathrm{pol2}(x)}{b_w}, \tag{5.21}$$

where b_w denotes the histogram bin width. The signal yield S is introduced analogously as

$$S = \frac{\int_{\mu-3\sigma}^{\mu+3\sigma} \mathrm{d}x \; G(x)}{b_w}.$$ (5.22)

The uncertainties are computed by using ROOT *IntegralError* function.

An example of the invariant mass distribution fit is shown in Fig. 5.4. The quality of the fit is evaluated by the pull distribution $g(x_i)$ that is defined as

$$g(x_i) = \frac{x_i - f(x_i)}{\sigma(x_i)},$$ (5.23)

where x_i is the i-th value, $f(x_i) = G(x_i) + \mathrm{pol2}(x_i)$ and the $\sigma(x_i)$ is the uncertainty of the i-th value.

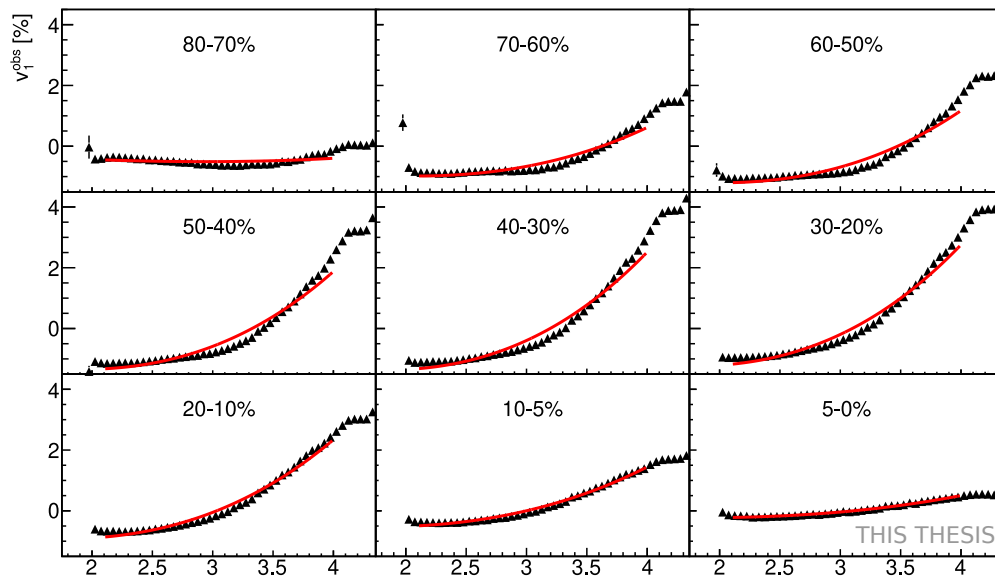## 5.4   Reconstruction of event plane and resolution

Figure 5.5: Flow coefficient v_1^{obs} as a function of pseudorapidity η for Au-Au collisions at $\sqrt{s_{\mathrm{NN}}} = 27$ GeV and at different centralities C measured by means of the EPD detector.

The EP was reconstructed including all corrections mentioned in Chapter 3.6 in 4 iterations that can be briefly described as:

1. Only ring-weighting was applied. The chosen ring-weights were $\vec{Z} = (1, 1, 1, 1, 1, \vec{0})$. The phi-weighting, eta-weighting, and psi-shifting cannot be used for the first iteration because they require values from the previous analysis. From the results of the first iteration, the weights for phi-weighting, correction values for psi-shifting, and v_1^{obs} and $\mathscr{R}_1$ values for eta-weighting are prepared.

2. The ring-weighting is switched to eta-weighting. Other corrections: phi-weighting and psi-shifting are applied. For the subsequent iteration, new results are used in the same way as mentioned above.

3. The same step as before is performed and the data are prepared for the last 4th iteration where the reconstruction of EP is launched together with the KFPF.

The reconstructed flow coefficients v_1^{obs}, as a function of pseudorapidity η in different centrality ranges C, used for the 4th iteration are shown in Fig. 5.5. The v_1^{obs} coefficient is fitted with polynomial function:

$$v_1^{\mathrm{obs}}(\eta, C) = a\eta^3 + c\eta. \tag{5.24}$$

The considered pseudorapidity range is $\eta \in (2.1; 4)$. The other η values measured by the EPD were neglected because of various edge detector effects. It should be noted that final eta-weight is v_1 instead of v_1^{obs}. However, these values are different only by scale factor $\mathscr{R}_1$, see Eq. (3.39). Thus, the v_1^{obs} dependence can be first fitted and scaled by the EP resolution later.

C [%]	a $[10^{-3}]$	c $[10^{-3}]$
0-5	0.198 ± 0.001	-1.91 ± 0.01
5-10	0.515 ± 0.001	-4.63 ± 0.01
10-20	0.859 ± 0.001	-7.90 ± 0.01
20-30	1.077 ± 0.001	-10.34 ± 0.01
30-40	1.086 ± 0.001	-11.09 ± 0.01
40-50	0.949 ± 0.001	-10.50 ± 0.01
50-60	0.745 ± 0.001	-9.00 ± 0.01
60-70	0.536 ± 0.002	-7.03 ± 0.02
70-80	0.100 ± 0.002	-2.59 ± 0.02

Table 5.3: Parameters from polynomial fit to the flow coefficient v_1^{obs} for Au-Au collisions at $\sqrt{s_{\mathrm{NN}}} = 27$ GeV for different centrality ranges C.

C [%]	$\mathscr{R}_1$
0-5	0.2090 ± 0.0006
5-10	0.3523 ± 0.0004
10-20	0.4563 ± 0.0002
20-30	0.5081 ± 0.0002
30-40	0.5048 ± 0.0002
40-50	0.4618 ± 0.0002
50-60	0.3971 ± 0.0002
60-70	0.3172 ± 0.0003
70-80	0.1294 ± 0.0008

Table 5.4: The resolution of the first order EP $\mathscr{R}_1$ for the last (IV) step in centrality ranges C.

The extracted polynomial coefficients a and c from the v_1^{obs} dependence are gathered in Tab. 5.3. The corrected first-order EP angular distribution Ψ_1 and the related EP resolution $\mathscr{R}_1$ in each iteration step are shown in Fig. 5.6 and Fig. 5.7, respectively. The EP resolution of the last iteration is gathered in Tab. 5.4.
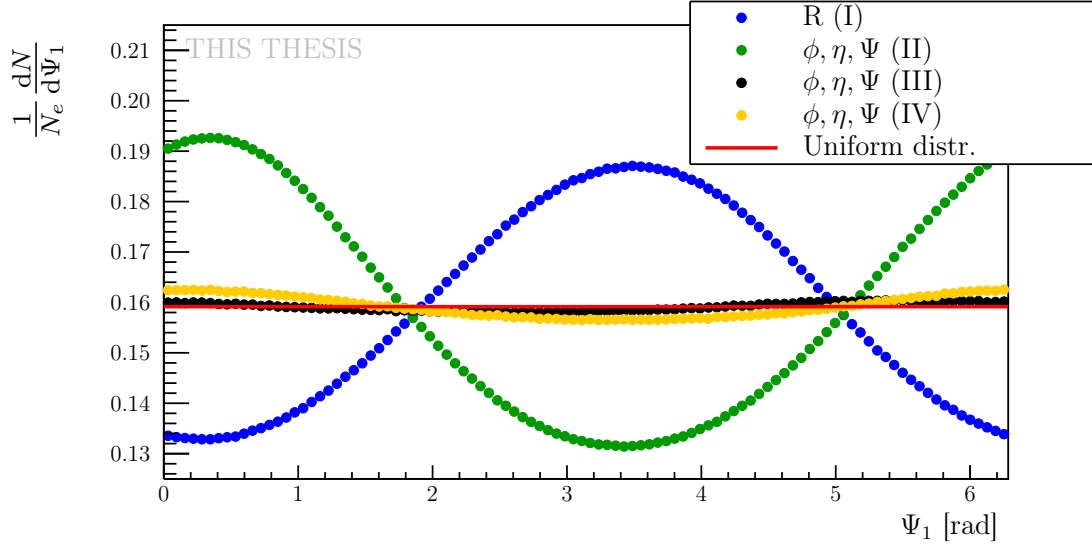

Figure 5.6: Comparison of $dN/d\Psi_1$ distribution scaled by number of events N_e with respect to the event plane angle Ψ_1, where R denotes the ring-weighting, ϕ is the phi-weighting, Ψ is the psi-shifting, η is the eta-weighting and (I-IV) represents the step of iterations for Au-Au collisions at energy $\sqrt{s_{\text{NN}}} = 27$ GeV. The red line shows the expected uniform distribution and N_e is the number of events.
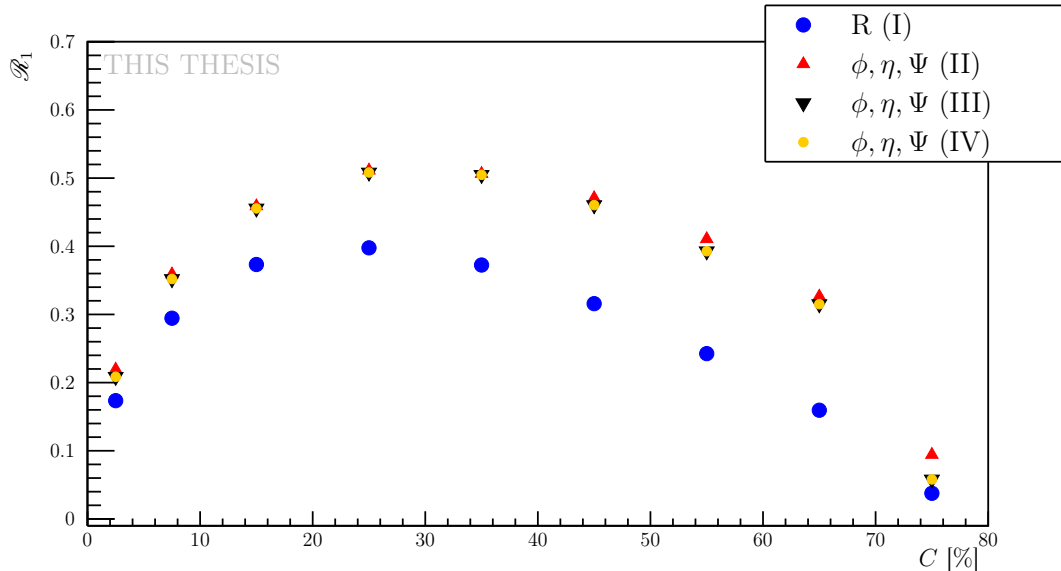

Figure 5.7: Comparison of the first order even plane resolution $\mathscr{R}_1$ as a function of centrality C where R denotes the ring-weighting, ϕ is the phi-weighting, Ψ is the psi-shifting, η is the eta-weighting and (I-IV) represents the step of iterations for Au-Au collisions at energy $\sqrt{s_{\text{NN}}} = 27$ GeV.

5.5 Daughter baryon angular distributions

In the next step, in order to obtain the global Λ and $\overline{\Lambda}$ hyperon polarization, one needs to extract the angular distribution of the daughter baryons. Recall, that the global polarization can be computed as

$$P_{\mathrm{H}} = \frac{8}{\pi \alpha_{\mathrm{H}}} \frac{\langle \sin(\Psi_1 - \phi_p^*) \rangle}{\mathscr{R}_1},$$ (5.25)

where the first order EP Ψ_1 and its resolution $\mathscr{R}_1$ has been already presented in the preceding pages and the last remaining needed information is the daughter baryon azimuthal angle in the rest frame of the mother particle.

First, one has to reconstruct the azimuthal angle of the daughter baryons. After the reconstruction of Λ and $\overline{\Lambda}$ candidates using KFPF, the associated daughter protons and antiprotons were plotted with respect to their azimuthal angle in the laboratory frame, see Fig. 5.8. The periodic minima that are visible in the distribution are caused by the construction of TPC which is segmented into 12 parts and some parts are less sensitive to the measurement, see Fig. 5.9 where the distribution is plotted in a polar graph and can be compared with the TPC construction. The shift of the distribution clockwise (protons) and anticlockwise (antiprotons) is caused by their electric charge in the magnetic field.
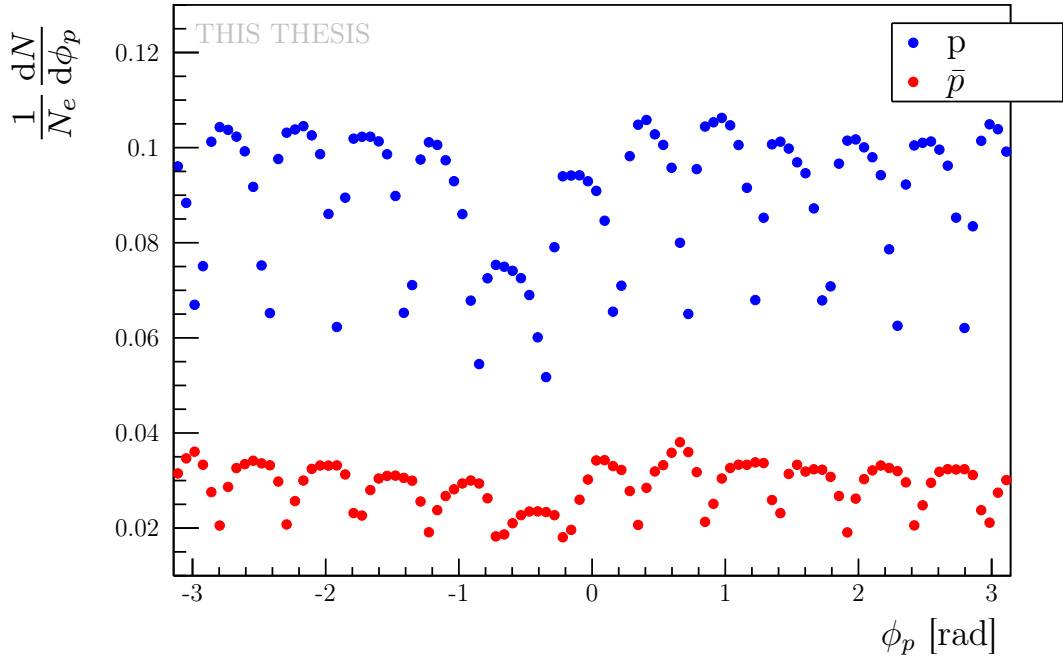

Figure 5.8: The angular distribution of the daughter protons (p) and antiprotons (p) from Λ and $\overline{\Lambda}$ decays, respectively, for Au-Au collisions at $\sqrt{s_{\mathrm{NN}}} = 27$ GeV where N_e is the number of events.
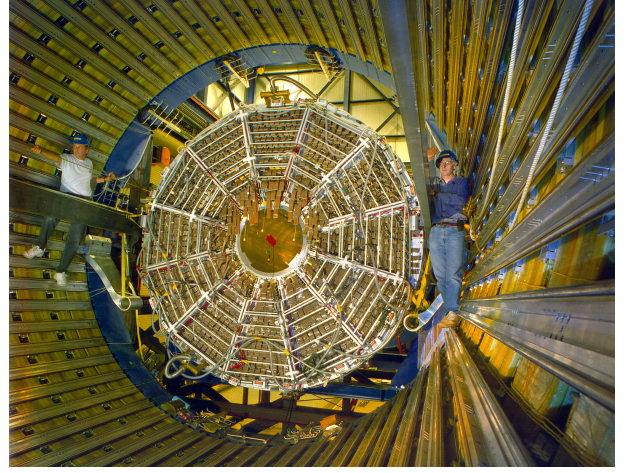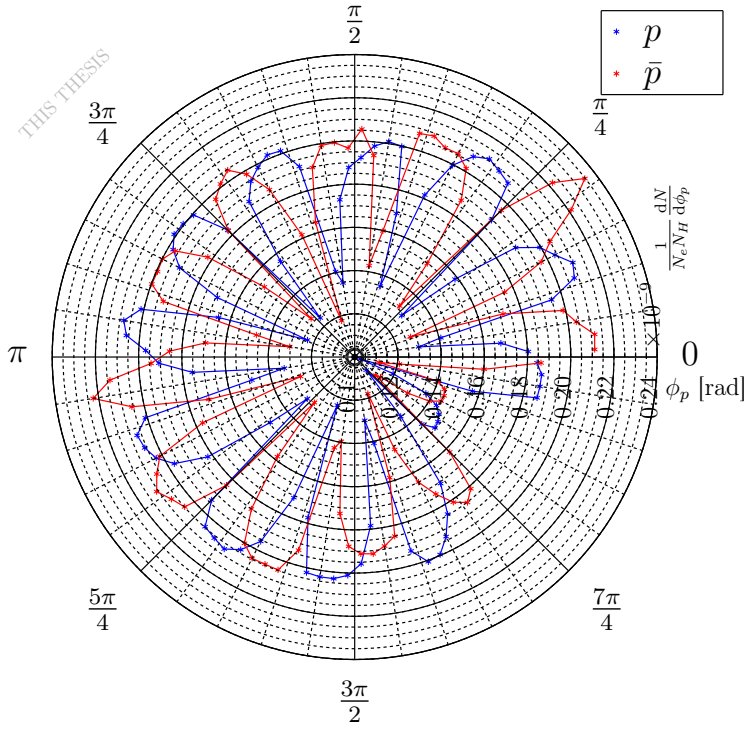
Figure 5.9: Left: The angular distribution of daughter protons (p) and antiprotons ($\overline{p}$) from Λ and $\overline{\Lambda}$ hyperon decays, respectively, in a polar graph for Au-Au collisions at $\sqrt{s_{\mathrm{NN}}} = 27$ GeV where N_e is the number of events and N_{H} is the number of related hyperons. Right: A photo of TPC construction at STAR [137].

The further step is the boost of the daughter protons and antiprotons in the rest frame of the mother Λ and $\overline{\Lambda}$ hyperons, respectively. The boost of the particle four-momentum $p = (E, p_x, p_y, p_z)$ is provided by the following relation:

$$
\begin{pmatrix} E' \\ p'_x \\ p'_y \\ p'_z \end{pmatrix} = \begin{pmatrix} \gamma & -\beta_x\gamma & -\beta_y\gamma & -\beta_z\gamma \\ -\beta_x\gamma & 1+(\gamma-1)\frac{\beta_x^2}{\beta^2} & (\gamma-1)\frac{\beta_x\beta_y}{\beta^2} & (\gamma-1)\frac{\beta_x\beta_z}{\beta^2} \\ -\beta_y\gamma & (\gamma-1)\frac{\beta_y\beta_x}{\beta^2} & 1+(\gamma-1)\frac{\beta_y^2}{\beta^2} & (\gamma-1)\frac{\beta_y\beta_z}{\beta^2} \\ -\beta_z\gamma & (\gamma-1)\frac{\beta_z\beta_x}{\beta^2} & (\gamma-1)\frac{\beta_z\beta_y}{\beta^2} & 1+(\gamma-1)\frac{\beta_z^2}{\beta^2} \end{pmatrix} \cdot \begin{pmatrix} E \\ p_x \\ p_y \\ p_z \end{pmatrix} \quad (5.26)
$$

with

$$
\vec{\beta} = (\beta_x, \beta_y, \beta_z) = (v_x, v_y, v_z) \qquad \text{and} \qquad \gamma = \frac{1}{\sqrt{1-\beta^2}}. \quad (5.27)
$$

Since the observed parameters are boosted into the laboratory frame, the boost back into the particle rest frame requires inverse Lorentz transformation which is similar to Eq. (5.26) except for the $\vec{\beta}$ which has to be with the opposite sign. The azimuthal angle of the boosted particle is then

$$
\phi_p^* = \arctan\left(\frac{p'_y}{p'_x}\right). \quad (5.28)
$$

Figure 5.10: The angular distribution of the daughter protons (p) and antiprotons ($\bar{p}$) from Λ and $\overline{\Lambda}$ decays, respectively, in the rest frame of the mother particle for Au-Au collisions at $\sqrt{s_{\mathrm{NN}}} = 27$ GeV where N_e is the number of events.

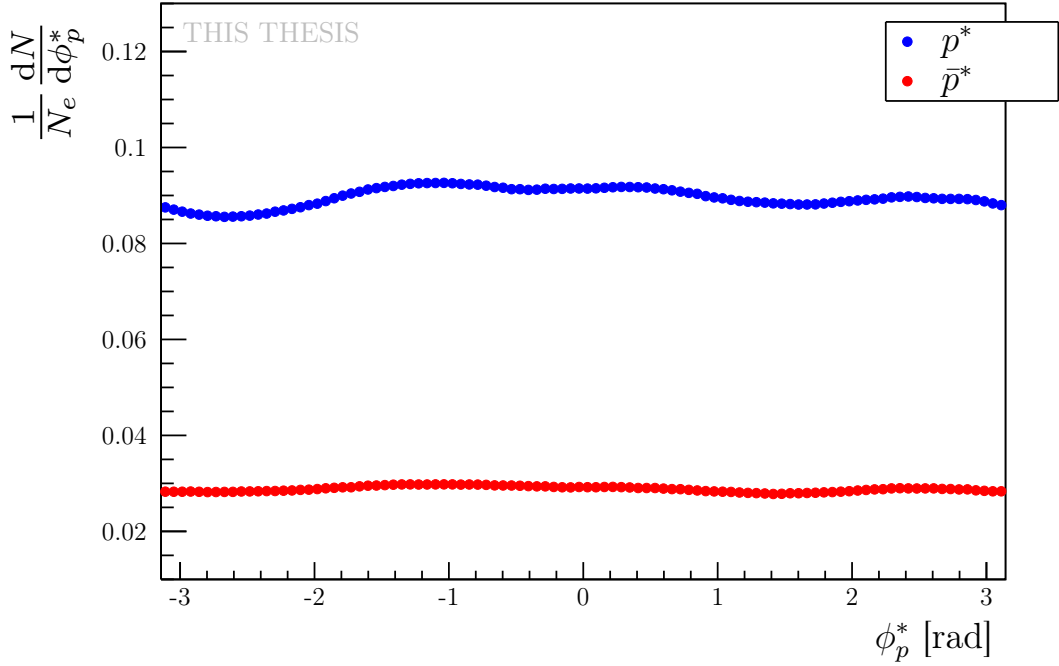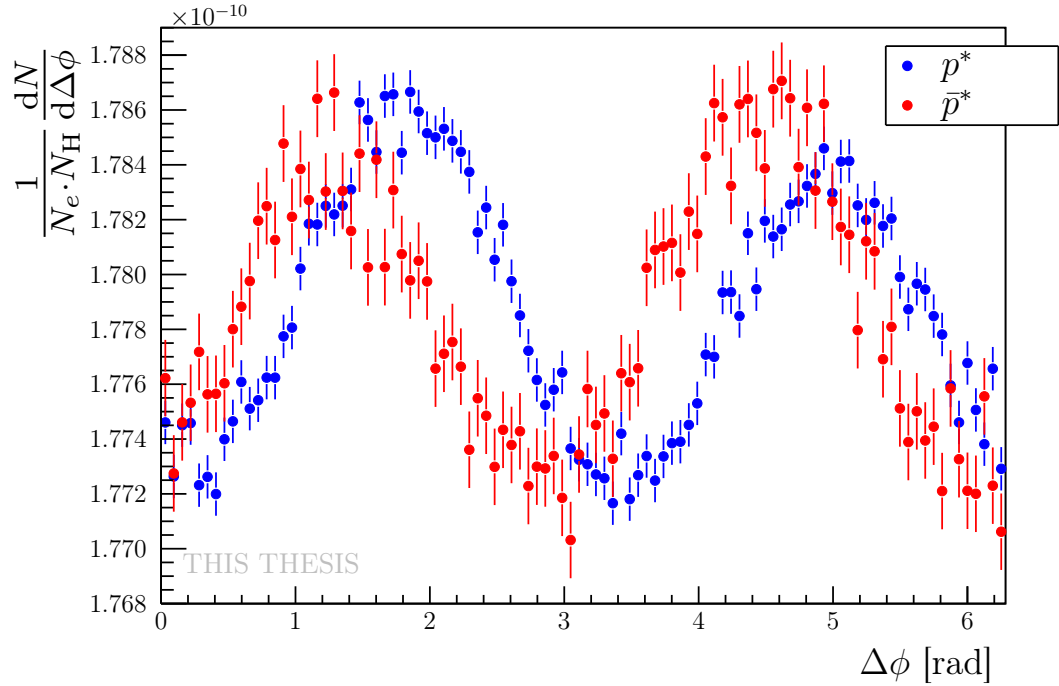Figure 5.11: The angular distribution of the daughter protons (p) and antiprotons ($\bar{p}$) from Λ and $\overline{\Lambda}$ decays, respectively, in the rest frame of the mother particle with respect to the angle of the event plane $\Delta\phi$ for Au-Au collisions at $\sqrt{s_{\mathrm{NN}}} = 27$ GeV where N_e is the number of events and N_{H} is the number of the corresponding hyperons.

The angular distribution of protons and antiprotons in the rest frame of the associated mother particle is presented in Fig. 5.10. Because the distribution of the EP should be uniform, the distribution of the daughter baryon distribution, as can be seen, is approximately uniform as well.

The last step is to utilize the knowledge of the EP angle gained in this Chapter in each event and obtain the final distribution $\Delta\phi = \Psi_1 - \phi_p^*$, see Fig. 5.11. As has been already mentioned, the daughter baryon should prefer the (opposite) direction of the mother Λ ($\overline{\Lambda}$) hyperon spin which is parallel to the direction of the system angular momentum J_{sys} that is perpendicular to the EP. This effect is noticeable in a polar graph in Fig. 5.12.
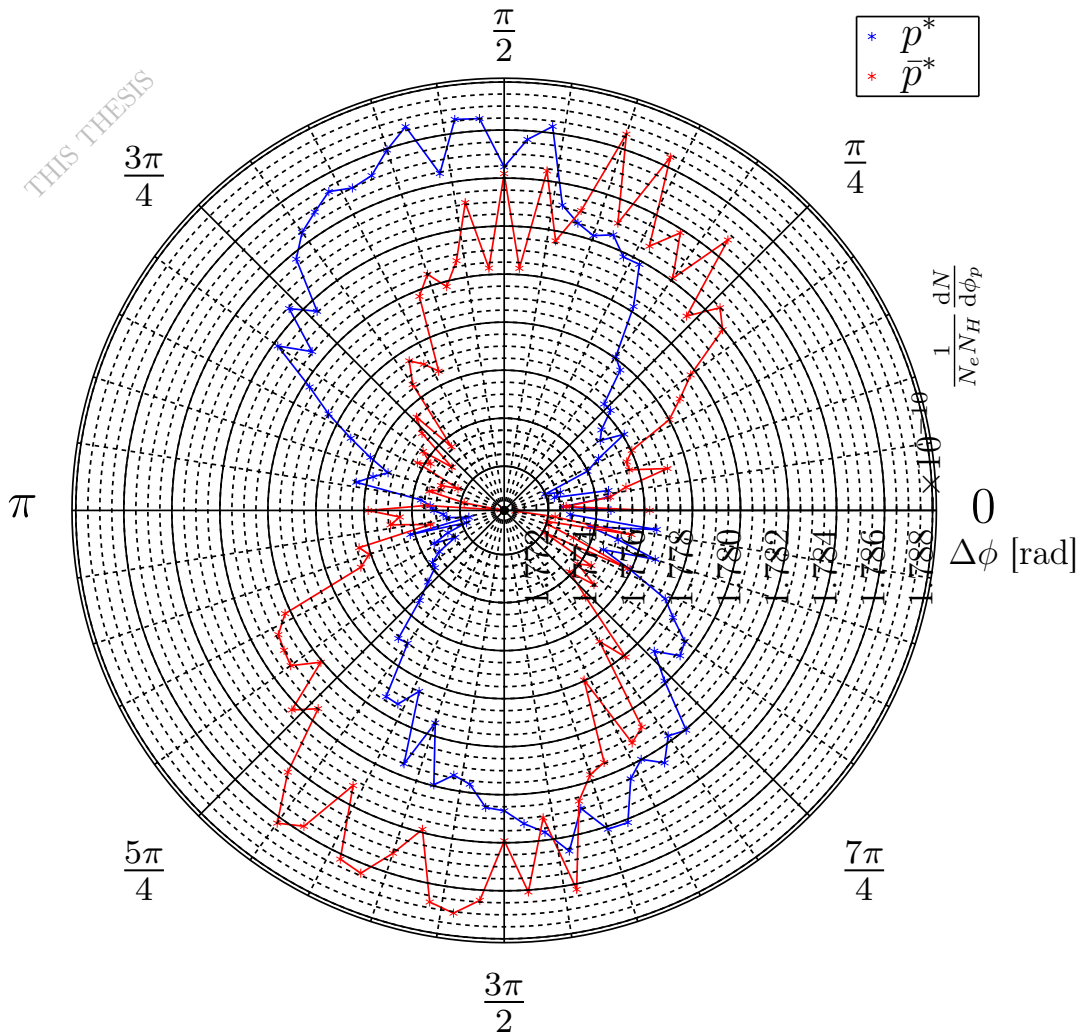
Figure 5.12: The angular distribution of the daughter protons (p) and antiprotons ($\overline{p}$) from Λ and $\overline{\Lambda}$ decays, respectively, in the rest frame of the mother particle with respect to the angle of event plane $\Delta\phi$ for Au-Au collisions at $\sqrt{s_{\mathrm{NN}}} = 27$ GeV in a polar graph, where N_e is the number of events and N_{H} is the number of the related hyperons.

Chapter 6

Results of global polarization of Lambda

This chapter presents the last steps needed for computation of the global Λ and $\overline{\Lambda}$ polarization P_{H}. Recall, that the polarization can be computed as

$$P_{\mathrm{H}} = \frac{8}{\pi\alpha_{\mathrm{H}}} \frac{\langle\sin(\Psi_1 - \phi_p^*)\rangle}{\mathscr{R}_1}, \tag{6.1}$$

where the first order EP Ψ_1, its resolution $\mathscr{R}_1$ and the azimuthal angle of the daughter particle in the hyperon's rest frame were extracted in Chapter 5. In this analysis, only hyperon candidates with $p_{\mathrm{T}} > 0.5$ GeV/c and $|y| < 1$ are considered.

Next, the other corrections, namely acceptance efficiency correction and helicity efficiency are discussed and applied.

At the end of this chapter, the various predictions of the global Λ polarization provided by hydrodynamic calculations are presented.

6.1 Polarization from a measurement

The extraction of the polarization signal $\langle\sin(\Psi_1 - \phi_p^*)\rangle$ can be realized using two different method. Results of the two methods may be then compared to estimate systematic uncertainties.

6.1.1 Invariant mass method

The first method called the invariant mass method (IMM) is based on the separation of a residual background signal, in particular, the polarization signal $\langle\sin(\Delta\phi)\rangle$ is rewritten as

$$\langle\sin(\Delta\phi)\rangle(M_{\mathrm{inv}}) = [1 - f^{Bg}(M_{\mathrm{inv}})] \cdot \langle\sin(\Delta\phi)\rangle_{Sg} + f^{Bg}(M_{\mathrm{inv}}) \cdot \langle\sin(\Delta\phi)\rangle_{Bg}, \tag{6.2}$$

where $\langle\sin(\Delta\phi)\rangle_{Sg}$ and $\langle\sin(\Delta\phi)\rangle_{Bg}$ is the peak and background polarization signal, respectively, and f^{Bg} is the background fraction having in this thesis the following form

$$f^{Bg}(x) = \frac{\text{pol2}(x)}{G(x) + \text{pol2}(x)}, \tag{6.3}$$

which is visualized in Fig. 6.1. The parameters needed for the computation of f^{Bg}, such as $A_{1,2}$, $\sigma_{1,2}$, $\mu_{1,2}$, a, b and c are extracted from the invariant mass distribution fits, in each analyzed centrality range.
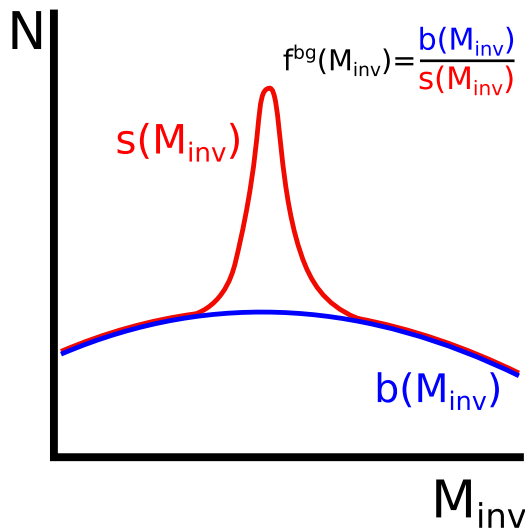

Figure 6.1: Schematic of a background fraction $f^{Bg}(M_{\text{inv}})$ where M_{inv} is the invariant mass, $s(M_{\text{inv}})$ is the measured signal and $b(M_{\text{inv}})$ is the background.

First, one has to compute the polarization signal for each invariant mass range M_{inv}. Then, the histogram is fitted with the function in Eq. (6.2). An example of this step for $30-40\%$ centrality is shown in Fig. 6.2 and Fig. 6.3. Results for all centrality ranges are gathered in Tab. 6.1.

C [%]	$\langle\sin(\Delta\phi)\rangle_{Sg}$ [10^{-4}]		$\langle\sin(\Delta\phi)\rangle_{Bg}$ [10^{-4}]	
	Λ	$\overline{\Lambda}$	Λ	$\overline{\Lambda}$
0-5	6.6 ± 0.4	-5 ± 1	1 ± 2	-4 ± 3
5-10	7.3 ± 0.5	-6 ± 1	2 ± 2	-6 ± 4
10-20	8 ± 1	-7 ± 1	5 ± 3	-5 ± 4
20-30	9 ± 1	-8 ± 1	5 ± 4	-7 ± 5
30-40	10 ± 1	-9 ± 2	3 ± 5	-10 ± 7
40-50	12 ± 1	-8 ± 2	-1 ± 8	-5 ± 10
50-60	11 ± 2	-6 ± 3	10 ± 11	-2 ± 14
60-70	11 ± 2	0 ± 4	5 ± 15	-7 ± 20
70-80	10 ± 4	2 ± 7	-22 ± 22	22 ± 32

Table 6.1: The polarization signal of the peak region $\langle\sin(\Delta\phi)\rangle_{Sg}$ and of the background $\langle\sin(\Delta\phi)\rangle_{Bg}$ for Λ and $\overline{\Lambda}$ hyperons with $p_T > 0.5$ GeV/c and $|y| < 1$ in Au-Au collisions at $\sqrt{s_{NN}} = 27$ GeV for various centrality ranges C.
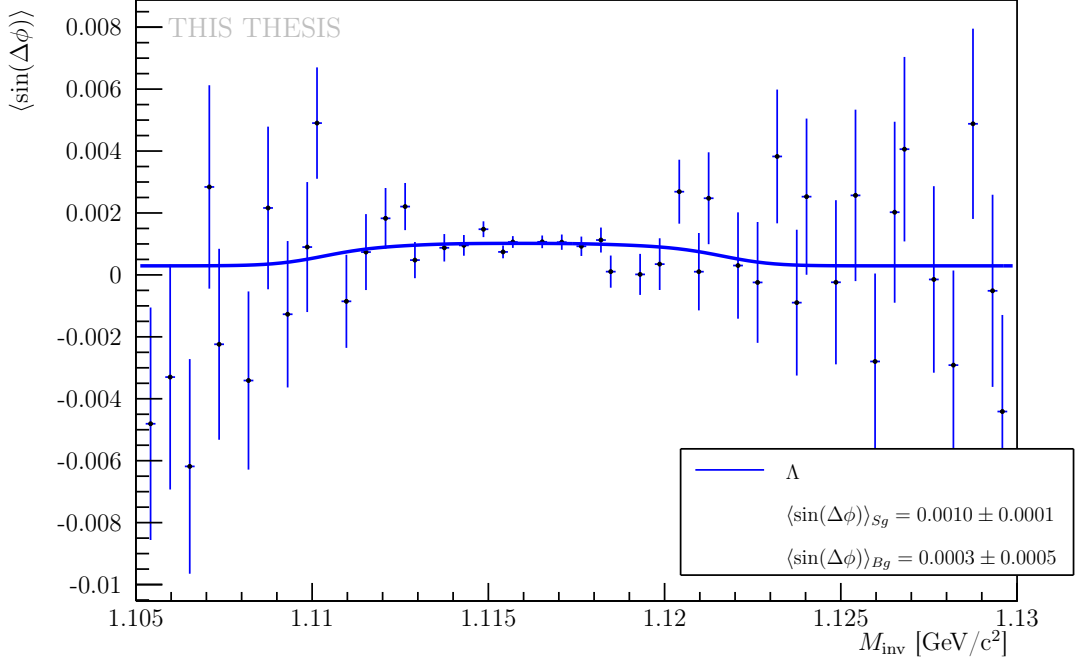
Figure 6.2: The polarization signal as a function of the Λ candidate invariant mass M_{inv} for Λ with $p_{\text{T}} > 0.5$ GeV/c and $|y| < 1$ in Au-Au collisions at $\sqrt{s_{\text{NN}}} = 27$ GeV in the centrality range $30 - 40\%$ fitted with the function in Eq. (6.2).

Figure 6.3: The polarization signal as a function of the $\overline{\Lambda}$ candidate invariant mass M_{inv} for $\overline{\Lambda}$ with $p_{\text{T}} > 0.5$ GeV/c and $|y| < 1$ in Au-Au collisions at $\sqrt{s_{\text{NN}}} = 27$ GeV in the centrality range $30 - 40\%$ fitted with the function in Eq. (6.2).
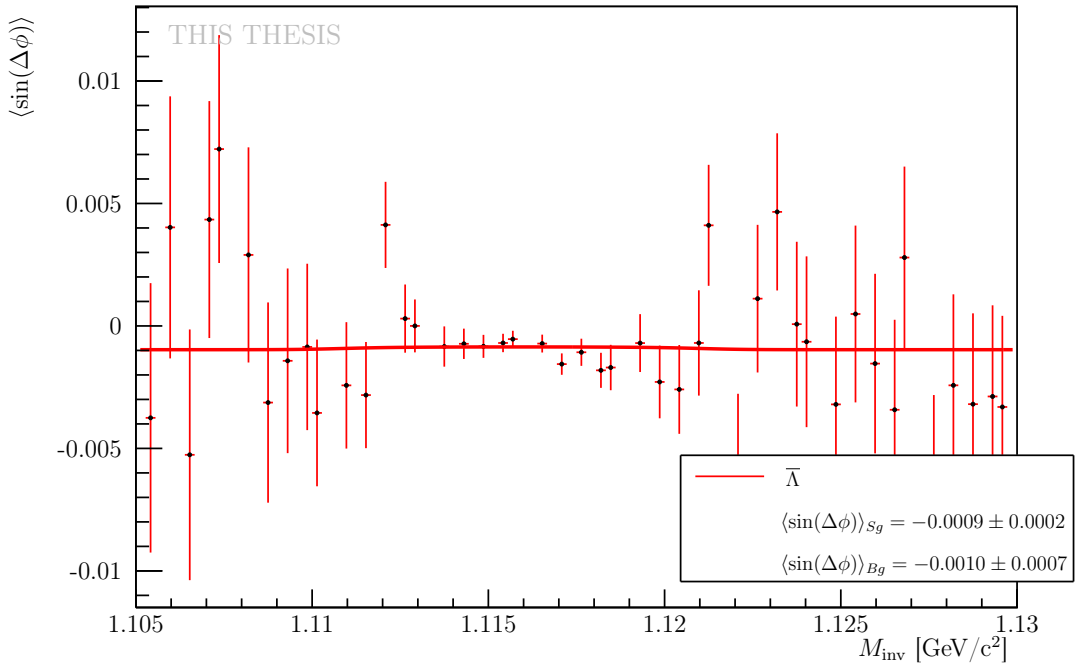
C [%]	P_Λ [%]	$P_{\overline{\Lambda}}$ [%]
0-5	1.08 ± 0.07	0.7 ± 0.1
5-10	0.70 ± 0.05	0.56 ± 0.08
10-20	0.60 ± 0.04	0.47 ± 0.07
20-30	0.60 ± 0.04	0.50 ± 0.08
30-40	0.69 ± 0.06	0.6 ± 0.1
40-50	0.87 ± 0.08	0.6 ± 0.1
50-60	1.0 ± 0.1	0.5 ± 0.2
60-70	1.2 ± 0.3	0.0 ± 0.5
70-80	3 ± 1	-1 ± 2

Table 6.2: The global polarization P_H for various centrality ranges C for Λ and $\overline{\Lambda}$ hyperons with $p_\mathrm{T} > 0.5$ GeV/c and $|y| < 1$ in Au-Au collisions at $\sqrt{s_\mathrm{NN}} = 27$ GeV where the invariant mass method (IMM) and acceptance efficiency correction are applied.

The global Λ and $\overline{\Lambda}$ polarization P_H computed using the IMM and Eq. (6.1) are presented in Fig. 6.4 and gathered in Tab. 6.2.
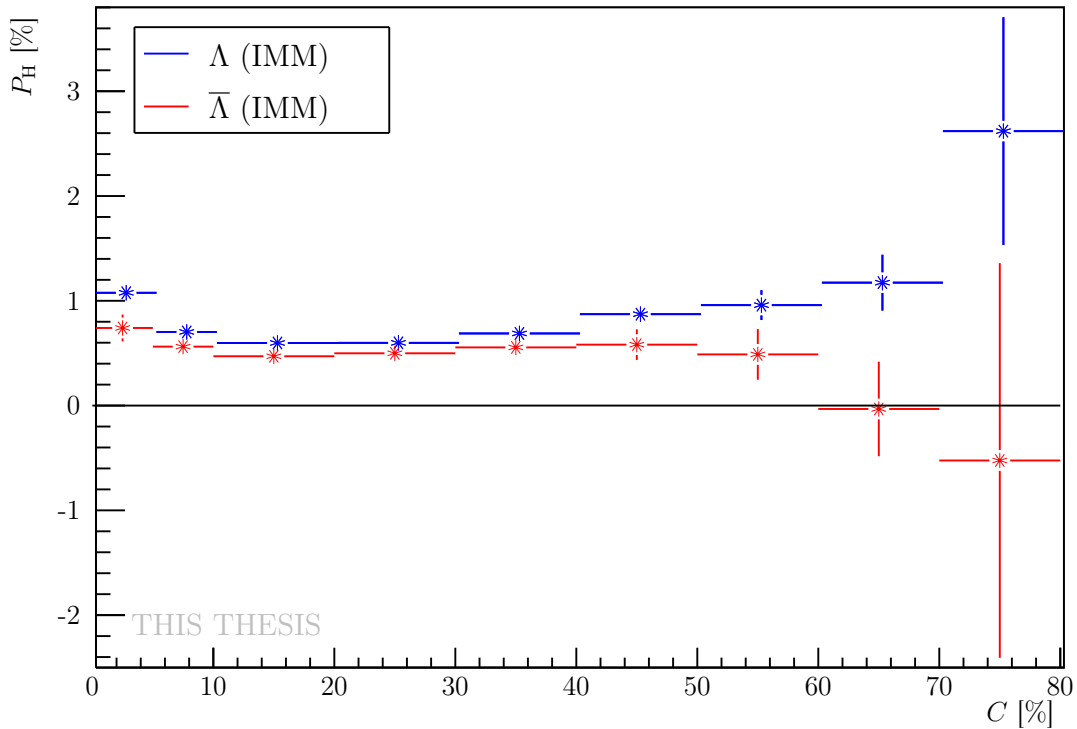
Figure 6.4: The global polarization P_H as a function of centrality C for Λ and $\overline{\Lambda}$ hyperons with $p_\mathrm{T} > 0.5$ GeV/c and $|y| < 1$ in Au-Au collisions at $\sqrt{s_\mathrm{NN}} = 27$ GeV where the invariant mass method (IMM) and acceptance efficiency correction are applied. Results for Λ hyperon are slightly shifted to the right for clarity.

6.1.2 Event plane method

The second method called the event plane method (EPM) is mainly used in flow analysis. Nevertheless, it can be used for polarization signal extraction as well. First, one divides the dataset into 12 intervals with respect to the $\Delta\phi = \Psi_1 - \phi_p^*$, for each centrality range C. The width of each $\Delta\phi$ range is $\pi/6$. Then, the signal yield S is computed for those ranges. After that, the signal yield distribution as a function of the $\Delta\phi$ is fitted by

$$S(\Delta\phi) = p_0 \left[1 + 2p_1 \sin(\Delta\phi) + 2 \sum_{n=2}^{k} p_n \cos(n\Delta\phi) \right],\qquad(6.4)$$

where the p_1 value represent the polarization signal $\langle \sin(\Psi_1 - \phi_p^*) \rangle$ [109]. An example of this step for $30 - 40\%$ centrality is shown in Fig. 6.5 and Fig. 6.6 where two different approximations of the Eq. (6.4) are used as a fitting function. First, only the first term of the sum (i.e. $k = 2$) is considered and the related parameters are labeled as p_n. In the second case, the sum of cosines is neglected and the related parameters are labeled as $p_{n,2}$. The results gathered in Tab. 6.3 show that the sum of cosines can be neglected because the higher terms do not significantly affect the p_1 parameter. The neglected higher terms are related to flow coefficients v_n.

	Λ		$\overline{\Lambda}$	
C [%]	p_1 [10^{-4}]	$p_{1,2}$ [10^{-4}]	p_1 [10^{-4}]	$p_{1,2}$ [10^{-4}]
0-5	4 ± 1	4 ± 1	2 ± 2	2 ± 2
5-10	4 ± 1	4 ± 1	2 ± 2	2 ± 2
10-20	8 ± 1	8 ± 1	-5 $\pm$ 2	-5 $\pm$ 2
20-30	8 ± 1	8 ± 1	-7 $\pm$ 2	-7 $\pm$ 2
30-40	8 ± 1	8 ± 1	-10 $\pm$ 2	-10 $\pm$ 2
40-50	11 ± 2	11 ± 2	-10 $\pm$ 3	-10 $\pm$ 3
50-60	10 ± 2	10 ± 2	-9 $\pm$ 4	-9 $\pm$ 4
60-70	9 ± 3	9 ± 3	0 ± 5	0 ± 5
70-80	8 ± 4	8 ± 4	-27 $\pm$ 7	-27 $\pm$ 7

Table 6.3: The polarization signal values p_1, $p_{1,2}$ of Λ and $\overline{\Lambda}$ hyperons with $p_{\mathrm{T}} > 0.5$ GeV/c and $|y| < 1$ for various centrality ranges C for Au-Au collisions at $\sqrt{s_{\mathrm{NN}}} = 27$ GeV extracted by the event plane method.

The global Λ and $\overline{\Lambda}$ polarization P_{H} computed using the EPM and Eq. (6.4) are presented in Fig. 6.7 and gathered in Tab. 6.4. In the next stage, the last two corrections will be discussed and applied.
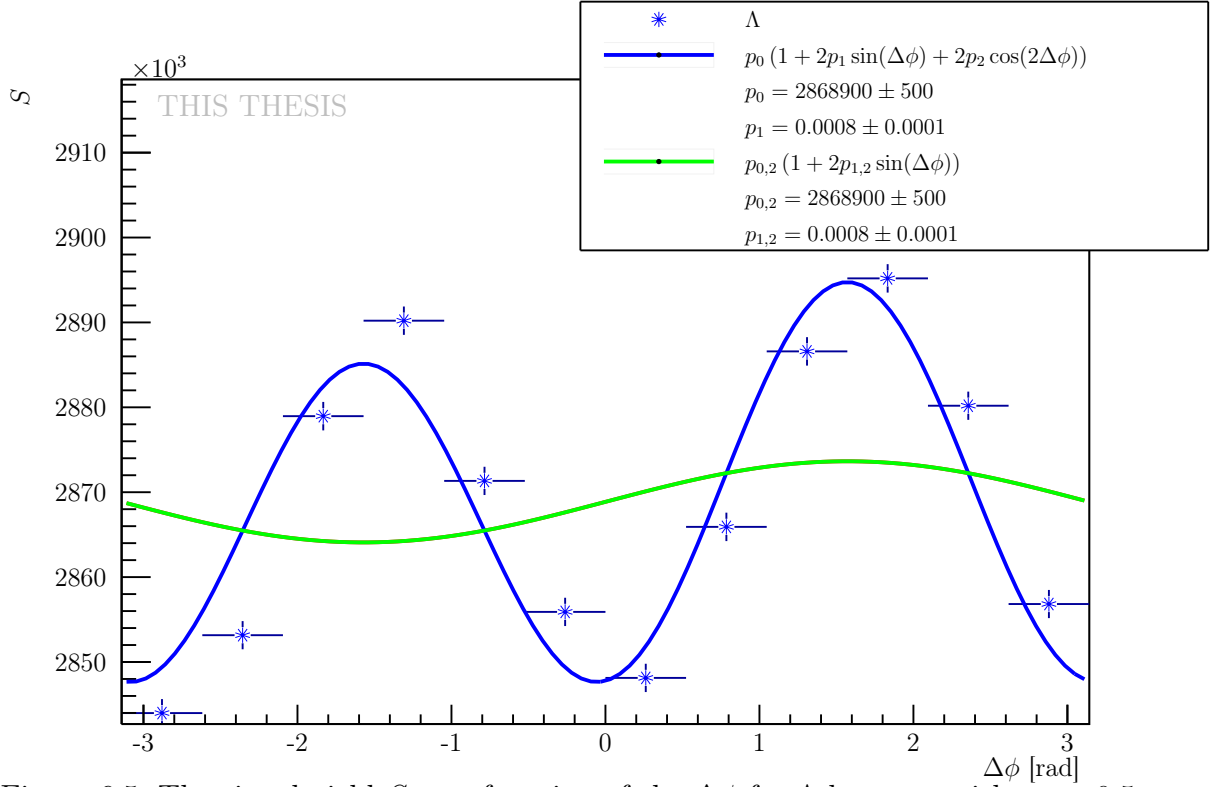
Figure 6.5: The signal yield S as a function of the $\Delta\phi$ for Λ hyperon with $p_{\mathrm{T}} > 0.5$ GeV/c and $|y| < 1$ from Au-Au collision at $\sqrt{s_{\mathrm{NN}}} = 27$ GeV in the centrality range $30 - 40\%$ fitted with the function in Eg. (6.4).

Figure 6.6: The signal yield S as a function of the $\Delta\phi$ for $\overline{\Lambda}$ hyperon with $p_{\mathrm{T}} > 0.5$ GeV/c and $|y| < 1$ from Au-Au collision at $\sqrt{s_{\mathrm{NN}}} = 27$ GeV in the centrality range $30 - 40\%$ fitted with the function in Eg. (6.4).
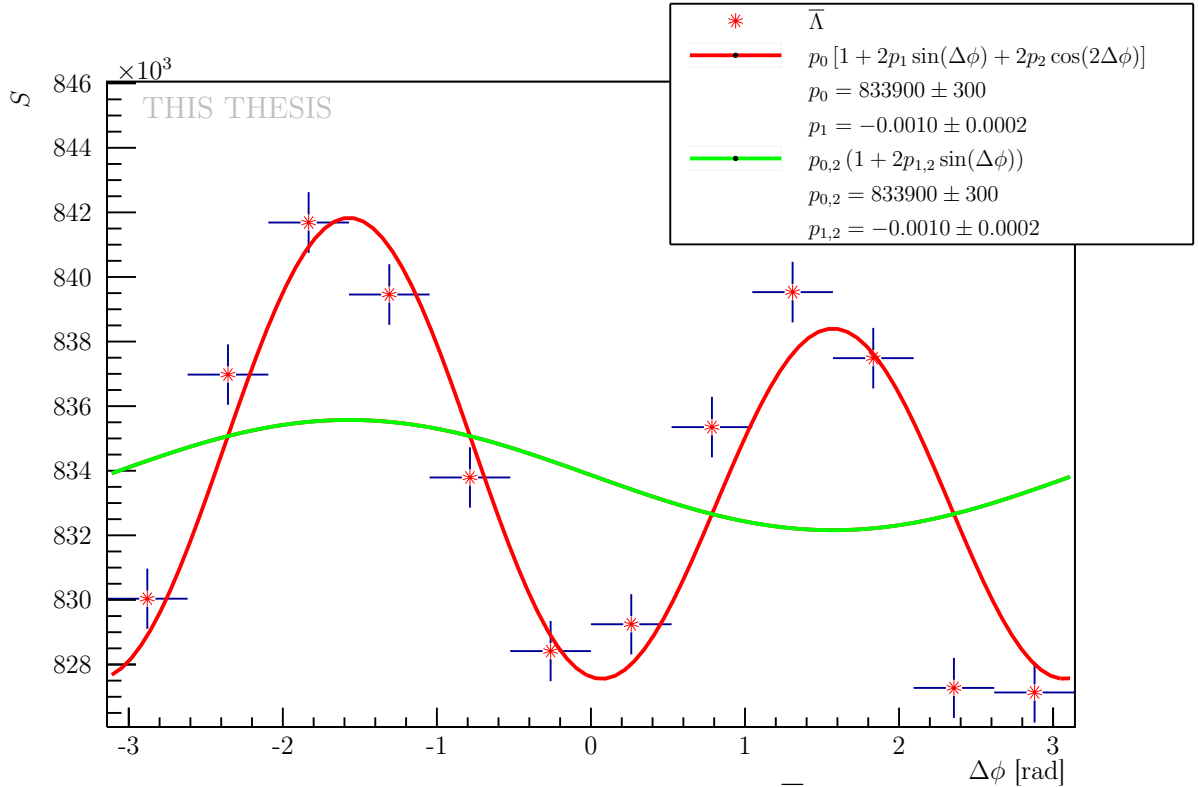
C [%]	P_Λ [%]	$P_{\overline{\Lambda}}$ [%]
0-5	0.7 ± 0.1	-0.3 ± 0.3
5-10	0.3 ± 0.1	-0.2 ± 0.2
10-20	0.58 ± 0.06	0.4 ± 0.1
20-30	0.55 ± 0.07	0.4 ± 0.1
30-40	0.56 ± 0.08	0.7 ± 0.1
40-50	0.8 ± 0.1	0.7 ± 0.2
50-60	0.9 ± 0.2	0.8 ± 0.3
60-70	1.0 ± 0.3	0.0 ± 0.5
70-80	2 ± 1	7 ± 2

Table 6.4: The global polarization P_H of Λ and $\overline{\Lambda}$ hyperon with $p_\mathrm{T} > 0.5$ GeV/c and $|y| < 1$ for various centrality ranges C in Au-Au collisions at $\sqrt{s_\mathrm{NN}} = 27$ GeV where the event plane method (EPM) and acceptance efficiency correction are applied.

Figure 6.7: The global polarization P_H as a function of centrality C for Λ and $\overline{\Lambda}$ hyperon with $p_\mathrm{T} > 0.5$ GeV/c and $|y| < 1$ in Au-Au collisions at $\sqrt{s_\mathrm{NN}} = 27$ GeV where the event plane me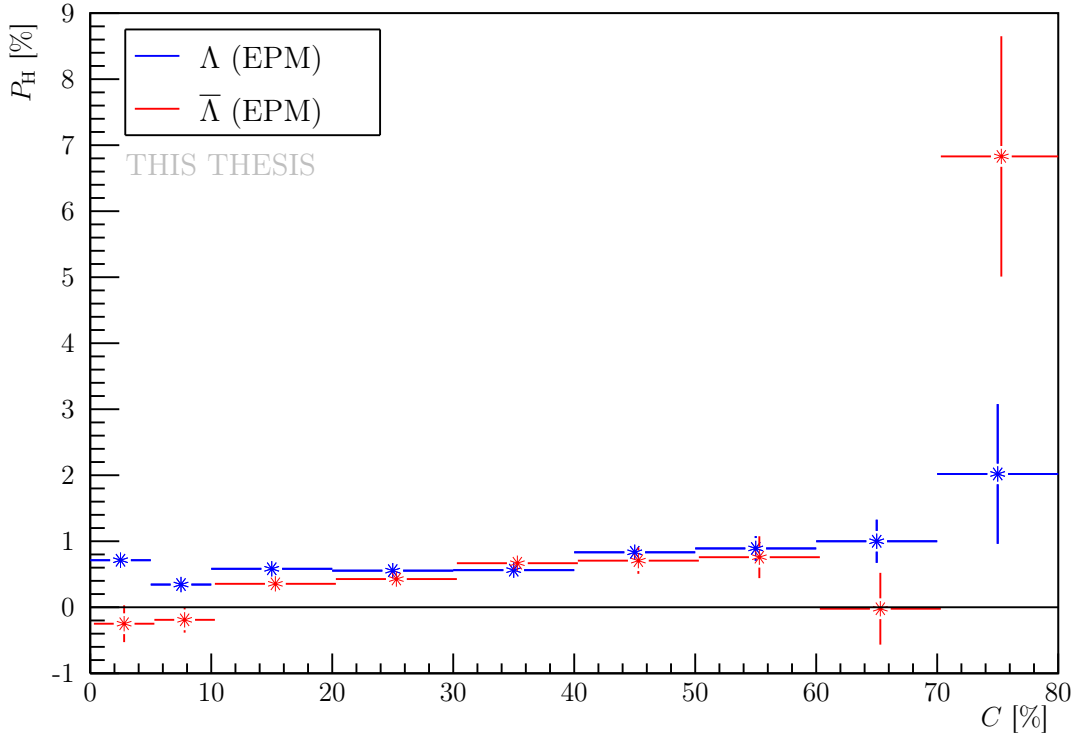thod (EPM) and acceptance efficiency correction are applied. Results for $\overline{\Lambda}$ hyperon are slightly shifted to the right for clarity.

6.1.3 Helicity efficiency

The helicity of a particle h is introduced as a positive h^+ (negative h^-) whether its momentum $\vec{p}$ is the same (opposite) direction as its spin $\vec{s}$. Mathematically, the

helicity can be written as

$$h = \frac{\vec{p} \cdot \vec{s}}{|\vec{p}| \cdot |\vec{s}|} = \begin{cases} h^+ & h > 0 \\ h^- & h < 0 \end{cases}. \tag{6.5}$$

Since the direction of the Λ's daughter baryon is positively correlated with the spin direction and negatively correlated in the case of $\overline{\Lambda}$, one can approximately estimate the helicity of the hyperons as

$$h_{\mathrm{H}} = \hat{\vec{p}}_{\mathrm{H}} \cdot \hat{\vec{p}}_{\mathrm{d}}^* = \begin{cases} \frac{\vec{p}_\Lambda \cdot \vec{p}_p^*}{|\vec{p}_\Lambda| \cdot |\vec{p}_p^*|} & \text{for } \Lambda \\ -\frac{\vec{p}_{\overline{\Lambda}} \cdot \vec{p}_{\overline{p}}^*}{|\vec{p}_{\overline{\Lambda}}| \cdot |\vec{p}_{\overline{p}}^*|} & \text{for } \overline{\Lambda} \end{cases}, \tag{6.6}$$

where $\vec{p}_{\mathrm{H}}$ and $\vec{p}_{\mathrm{d}}^*$ is the momentum vector of the hyperon and daughter baryon in the rest frame of the mother hyperon. The $\hat{\vec{p}}_{\mathrm{H}} \cdot \hat{\vec{p}}_{\mathrm{d}}$ distribution for the Λ and $\overline{\Lambda}$ hyperons from the analyzed dataset is shown in Fig. 6.8. This distribution reveals that Λ with a negative helicity and $\overline{\Lambda}$ with a positive helicity are measured in larger amounts
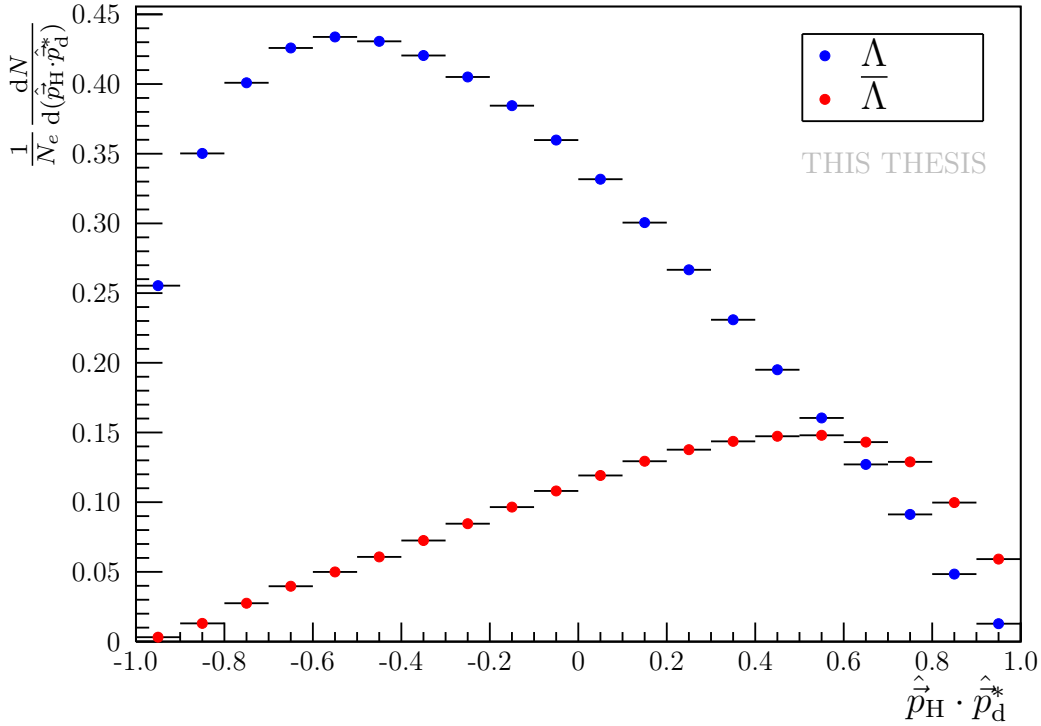

Figure 6.8: The $\hat{\vec{p}}_{\mathrm{H}} \cdot \hat{\vec{p}}_{\mathrm{d}}$ distribution where $\hat{\vec{p}}_{\mathrm{H}}$ is the momentum vector of Λ or $\overline{\Lambda}$ hyperon normalized to a unit vector and $\hat{\vec{p}}_{\mathrm{d}}$ is the momentum or opposite momentum of the daughter baryon of the Λ or $\overline{\Lambda}$ hyperon normalized to a unit vector, respectively, for Au-Au collisions at energy $\sqrt{s_{\mathrm{NN}}} = 27$ GeV. The N_e represents number of events.

The helicity efficiency is mainly a detector effect and can be explained by the fact that the mass of a pion $m_\pi \approx 139.6$ MeV/c^2 is much lower than the mass of a proton $m_p \approx 938.2$ MeV/c^2 [138]. Therefore, the slower pions are more likely lost in the

TPC than the heavier protons. This situation is depicted in Fig. 6.9, where one can see two Λs (blue arrow) and two $\overline{\Lambda}$s (red arrow) whereas the momentum of the first one is positively correlated with the global angular momentum of the system L and the second one's momentum is negatively correlated. In the laboratory frame, both of them are moving away from the the primary vertex V. However, in case of Λ polarization, in the rest frame of the Λ, proton's momentum p_p^* is positively correlated with the global angular momentum L. Due to momentum energy conservation, the pion's momentum $p_{\pi^-}^*$ has the opposite direction than the proton. Hence, after the boost in the laboratory frame, the pion from the Λ decay with a positive helicity is slower than the pion having the same momentum in the Λ's rest frame coming from the Λ with a negative helicity. Thus the Λ with a positive helicity is less likely reconstructed because the slower pion is more likely to be lost [139].
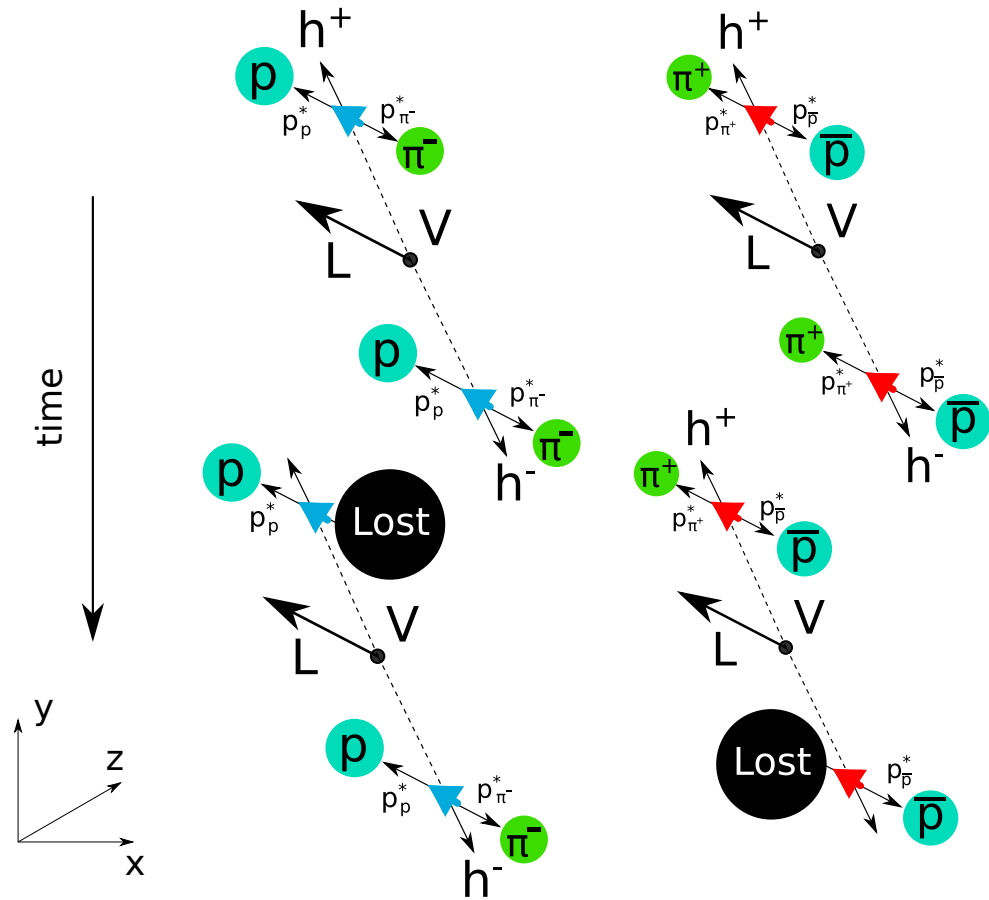

Figure 6.9: Scheme of the Λ (blue arrow) and $\overline{\Lambda}$ (red arrow) decay including the daughter particles proton p, antiproton $\overline{p}$, negative pion π^- and positive pion π^+ with their momentum in the rest frame of mother particle p_p^*, $p_{\overline{p}}^*$, p_{π^-} and p_{π^+}, respectively, and h^+ and h^- represents positive and negative helicity, respectively, the V is the primary vertex and L the global angular momentum of the system.

By analogy but with the difference that the antiproton's momentum $\vec{p}_{\overline{p}}$ is negatively correlated with the global angular momentum L, one can find out, that the $\overline{\Lambda}$ with

a positive helicity is more likely to be reconstructed than that one with a negative helicity.

If one focuses on the polarization signal $\langle\sin(\Psi_1 - \phi_p^*)\rangle$ as a function of the hyperon azimuthal angle ϕ_H with respect to the first order EP Ψ_1, cf. Fig. 6.10, the higher polarization signal in one direction is obvious[1]. In the case of Λ, the increased polarization signal is visible approximately at angle $3\pi/2$ which corresponds to the idea that Λs with a negative helicity has increased efficiency in its reconstruction. On the other hand, the polarized Λ at angle $\pi/2$ has the efficiency decreased.

Since the helicity efficiency in Fig. 6.10 causes a sinusoidal shape of the polarization signal, the effect should cancel out for the global hyperon polarization P_H integrated over all values ϕ_H.
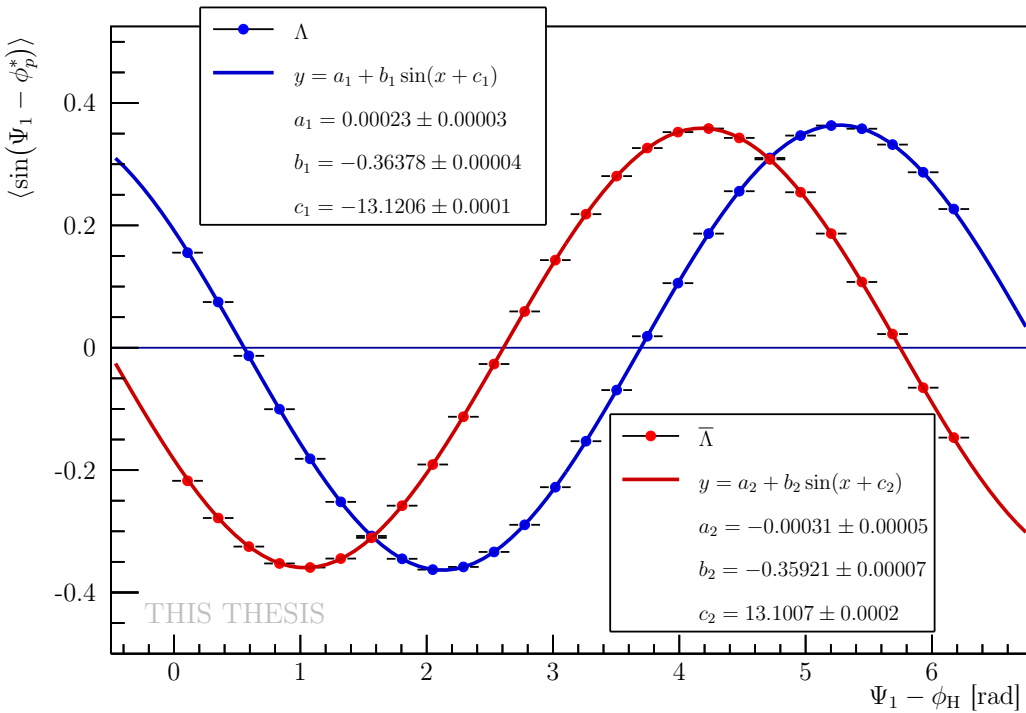

Figure 6.10: The polarization signal $\langle\sin(\Psi_1 - \phi_p^*)\rangle$ of Λ (blue) and $\overline{\Lambda}$ (red) as a function of $\Psi_1 - \phi_H$ from Au-Au collisions at energy $\sqrt{s_{NN}} = 27$ GeV for centrality range $C = 0 - 80\%$ where Ψ_1 is the first order event plane, ϕ_p^* the azimuthal angle of the daughter baryon in the rest frame of the mother hyperon and ϕ_H is the hyperon's azimuthal angle.

6.1.4 Acceptance efficiency correction

The relation for the global lambda polarization in Eq. (3.40) assumes a perfect 4π detector. To acquire more accurate results, one should consider the influence of the

---

[1]The polarization signal is not the same as the global hyperon polarization P_H where among other things the decay parameter $\alpha_{\overline{\Lambda}}$ with a negative sign would flip the function in Fig. 6.10 for $\overline{\Lambda}$ hyperons.

imperfect detector acceptance. Therefore, the derivation of $\langle\sin(\Psi_{RP}-\phi_p^*)\rangle$ in Eq. (3.36) taking into account the dependence of the polarization P_H on the reaction plane Ψ_{RP} and the azimuthal angle of the Λ hyperon momentum $\vec{p}_H$ is modified as follows

$$\langle\sin(\Psi_{RP}-\phi_p^*)\rangle = \int_S \frac{d\Omega}{4\pi}\int_0^{2\pi}\frac{d\phi_H}{2\pi}\int_0^{2\pi}\frac{d\Psi_{RP}}{2\pi}A(\vec{p}_H,\vec{p}_p^*)\overbrace{\frac{dN}{d\Omega}(\Psi_{RP},\phi_H)}^{\frac{dN}{d\cos\theta^*}(\Psi_{RP},\phi_H)=1+\alpha_H P_H(\Psi_{RP},\phi_H)\sin\theta_p^*\sin(\Psi_{RP}-\phi_p^*)}\sin(\Psi_{RP}-\phi_p^*),$$

(6.7)

where $A(\vec{p}_H,\vec{p}_p^*)$ is the function describing the acceptance of the detector [140]. Due to the symmetry of the system, the global polarization P_H can be expand into Fourier series of even harmonics

$$P_H(\Psi_{RP}-\phi_H,p_T^H,\eta^H)=\sum_{n=0}^{+\infty}P_H^{(2n)}(p_T^H,\eta^H)\cos[2n(\Psi_{RP}-\phi_H)],\qquad(6.8)$$

where p_T^H is the transverse momentum and η^H is the pseudorapidity of the hyperon, respectively. In this case, the global polarization $P_H(p_T^H,\eta^H)$ is defined as

$$P_H(p_T^H,\eta^H)\equiv\frac{1}{2\pi}\int_0^{2\pi}d\Delta_H P_H(\overbrace{\Psi_{RP}-\phi_H}^{\Delta_H},p_T^H,\eta^H)=P_H^{(0)}(p_T^H,\eta^H).\qquad(6.9)$$

Considering an imperfect detector, the global polarization of hyperon P_H in Eq. (3.40) is proportional to $P_H^{(0)}$ including the other higher harmonics, e.g. $P_H^{(2)}$ [141]. To prove that, one computes the integral over the Ψ_{RP} in Eq. (6.7) as follows

$$\int_0^{2\pi}\frac{d\Psi_{RP}}{2\pi}[\overbrace{\sin(\Psi_{RP}-\phi_p^*)}^{\int_0^{2\pi}d\Psi_{RP}\sin(\Psi_{RP}-\phi_p^*)=0}+\alpha_H\overbrace{P_H(\Psi_{RP},\phi_H)}^{\text{Eq. (6.8)}}\sin\theta_p^*\overbrace{\sin^2(\Psi_{RP}-\phi_p^*)}^{\frac{1}{2}\{1-\cos[2(\Psi_{RP}-\phi_p^*)]\}}]=$$

$$=\alpha_H\sin\theta_p^*\int_0^{2\pi}\frac{d\Psi_{RP}}{4\pi}\sum_{n=0}^{+\infty}P_H^{(2n)}\{\overbrace{\cos[2n(\Psi_{RP}-\phi_H)]}^{+\sum_{n=0}^{+\infty}\int_0^{2\pi}d\Psi_{RP}P_H^{(2n)}\cos[2n(\Psi_{RP}-\phi_H)]=2\pi P_H^{(0)}}-$$

$$-\overbrace{\cos[2n(\Psi_{RP}-\phi_H)]\cos[2(\Psi_{RP}-\phi_p^*)]}^{\frac{1}{2}\cos[2(\Psi_{RP}(n-1)+\phi_p^*-n\phi_H)]+\frac{1}{2}\cos[2(\Psi_{RP}(n+1)-\phi_p^*-n\phi_H)]}\}=$$

$$\overset{n\leq2}{=}\frac{\alpha_H\sin\theta_p^*}{2}\left[P_H^{(0)}-\int_0^{2\pi}\frac{d\Psi_{RP}}{4\pi}[P_H^{(2)}\{\cos[2(\phi_p^*-\phi_H)]+\overbrace{\cos[4\Psi_{RP}-2(\phi_p^*+\phi_H)]}^{\int_0^{2\pi}d\Psi_{RP}[\cdots]=0}\}]\right]=$$

$$=\frac{\alpha_H\sin\theta_p^*}{2}\left[P_H^{(0)}-\frac{1}{2}P_H^{(2)}\cos[2(\phi_p^*-\phi_H)]\right],\qquad(6.10)$$

where the higher terms $(n>2)$ were neglected. Hence, the Eq. (6.7) can be rewritten as

$$\langle\sin(\Psi_{RP}-\phi_p^*)\rangle=\frac{\alpha_H}{2}\int_S\frac{d\Omega}{4\pi}\int_0^{2\pi}\frac{d\phi_H}{2\pi}A(\vec{p}_H,\vec{p}_p^*)\sin\theta_p^*\left[P_H^{(0)}-\frac{1}{2}P_H^{(2)}\cos[2(\phi_p^*-\phi_H)]\right]$$

$$\frac{8}{\alpha_{\mathrm{H}}\pi}\langle\sin\left(\Psi_{\mathrm{RP}}-\phi_p^*\right)\rangle = P_{\mathrm{H}}^{(0)} \overbrace{\frac{4}{\pi}\int_S\frac{\mathrm{d}\Omega}{4\pi}\int_0^{2\pi}\frac{\mathrm{d}\phi_{\mathrm{H}}}{2\pi}A(\vec{p}_{\mathrm{H}},\vec{p}_p^*)\sin\theta_p^*}^{\equiv A_0(p_{\mathrm{T}}^{\mathrm{H}},\eta_{\mathrm{H}})} -$$

$$- P_{\mathrm{H}}^{(2)} \overbrace{\frac{2}{\pi}\int_S\frac{\mathrm{d}\Omega}{4\pi}\int_0^{2\pi}\frac{\mathrm{d}\phi_{\mathrm{H}}}{2\pi}A(\vec{p}_{\mathrm{H}},\vec{p}_p^*)\sin\theta_p^*\cos[2(\phi_p^*-\phi_{\mathrm{H}})]}^{\equiv A_2(p_{\mathrm{T}}^{\mathrm{H}},\eta_{\mathrm{H}})}$$

$$\frac{8}{\alpha_{\mathrm{H}}\pi}\langle\sin\left(\Psi_{\mathrm{RP}}-\phi_p^*\right)\rangle = A_0(p_{\mathrm{T}}^{\mathrm{H}},\eta_{\mathrm{H}})P_{\mathrm{H}}^{(0)}(p_{\mathrm{T}}^{\mathrm{H}},\eta_{\mathrm{H}}) - A_2(p_{\mathrm{T}}^{\mathrm{H}},\eta_{\mathrm{H}})P_{\mathrm{H}}^{(2)}(p_{\mathrm{T}}^{\mathrm{H}},\eta_{\mathrm{H}}). \qquad (6.11)$$

The first contribution of the detector acceptance, $A_0(p_{\mathrm{T}}^{\mathrm{H}},\eta_{\mathrm{H}})$, influences the overall scale of the measured global polarization. The second one, $A_2(p_{\mathrm{T}}^{\mathrm{H}},\eta_{\mathrm{H}})$, proportional to $P_{\mathrm{H}}^{(2)}(p_{\mathrm{T}}^{\mathrm{H}},\eta_{\mathrm{H}})$ caused by non-uniform detector acceptance is expected to be small and can be neglected [93]. In the case of a perfect detector, the following applies

$$A_0(p_{\mathrm{T}}^{\mathrm{H}},\eta_{\mathrm{H}}) = 1, \quad A_2(p_{\mathrm{T}}^{\mathrm{H}},\eta_{\mathrm{H}}) = 0. \qquad (6.12)$$

Because of the low background for hyperons, the values of the acceptance functions $A_0(p_{\mathrm{T}}^{\mathrm{H}},\eta_{\mathrm{H}})$ and $A_2(p_{\mathrm{T}}^{\mathrm{H}},\eta_{\mathrm{H}})$ can be extracted from the measured data by averaging over all events with hyperons candidates:

$$A_0(p_{\mathrm{T}}^{\mathrm{H}},\eta_{\mathrm{H}}) = \frac{4}{\pi}\overline{\sin\theta_p^*}, \qquad (6.13)$$

$$A_2(p_{\mathrm{T}}^{\mathrm{H}},\eta_{\mathrm{H}}) = \frac{2}{\pi}\overline{\sin\theta_p^*\cos[2(\phi_p^*-\phi_{\mathrm{H}})]}. \qquad (6.14)$$

The extracted parameters A_0 and A_2 integrated over $p_{\mathrm{T}}^{\mathrm{H}}$ and η_{H} from the processed dataset are gathered in Fig 6.11 and Fig. 6.12.

A_0	1.02586 ± 0.00001
A_2	-0.10860 ± 0.00001

Table 6.5: Extracted A_0 and A_2 parameters for acceptance efficiency correction from Au-Au collisions at $\sqrt{s_{\mathrm{NN}}} = 27$ GeV. See text for more details.

As can be seen, the parameters A_0 and A_2, see Tab. 6.5, are close to the case of the perfect detector, cf. Eq. (6.12). The second parameter A_2 is small and can be neglected. The final global hyperon polarization p_{H} including the acceptance efficiency correction has the form

$$P_{\mathrm{H}} = \frac{1}{A_0}\frac{8}{\pi\alpha_{\mathrm{H}}}\frac{\langle\sin\left(\Psi_1-\phi_p^*\right)\rangle}{\mathscr{R}_1}. \qquad (6.15)$$

The results of P_{H} for Λ and $\overline{\Lambda}$ can be easily divided by A_0 value to apply the final correction.
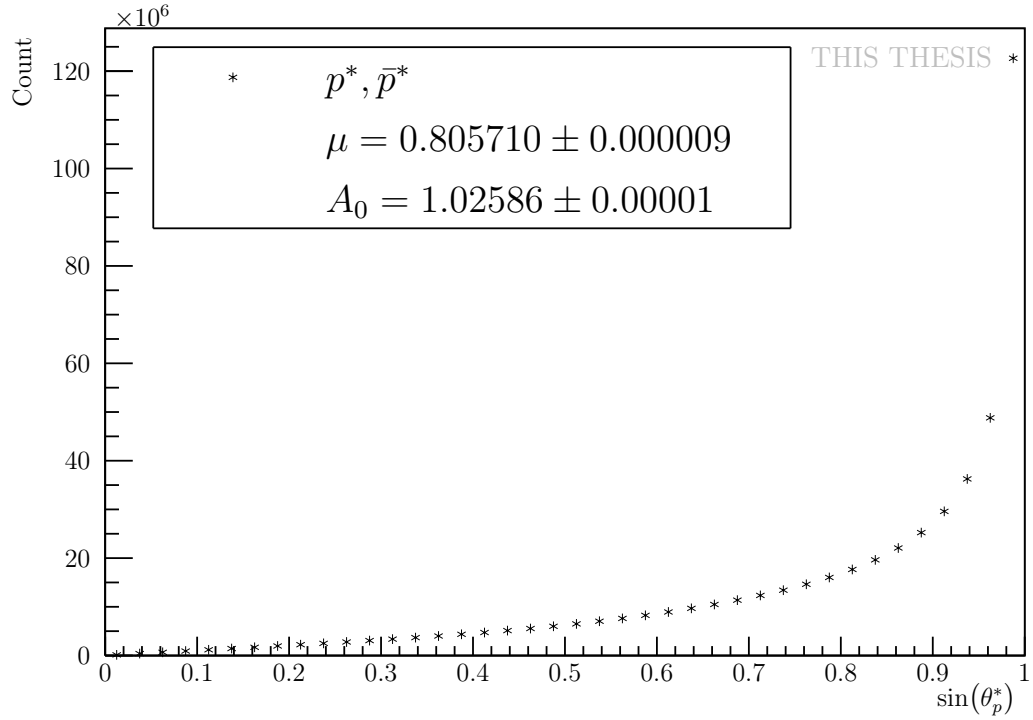
Figure 6.11: The histogram of $\sin\left(\theta_p^*\right)$ where θ_p^* is the polar angle of the daughter proton (p) and antiproton $(\overline{p})$ in the rest frame of mother particle Λ and $\overline{\Lambda}$, respectively, and A_0 is parameter used for acceptance efficiency correction. The data are from Au-Au collisions at $\sqrt{s_{\mathrm{NN}}} = 27$ GeV.
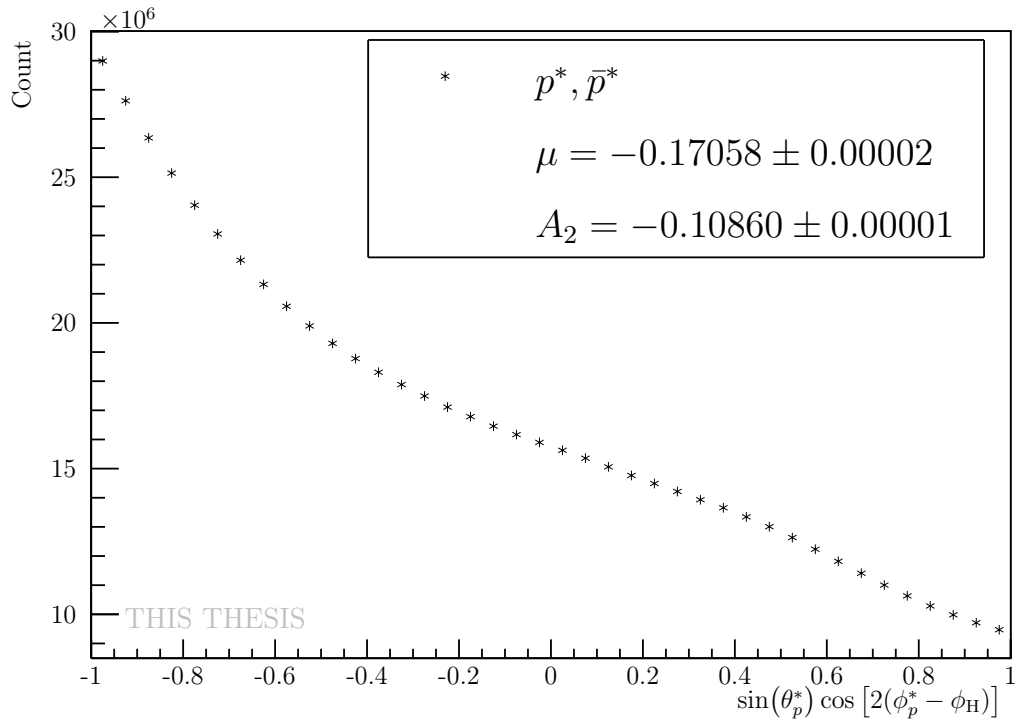

Figure 6.12: The histogram of $\sin\left(\theta_p^*\right)\cos\left[2(\phi_p^* - \phi_{\mathrm{H}})\right]$ where θ_p^* and ϕ_p^* are the polar and azimuthal angle of the daughter proton (p) and antiproton $(\overline{p})$ in the rest frame of mother hyperon Λ and $\overline{\Lambda}$, respectively, ϕ_{H} is the azimuthal angle of the related hyperon and A_2 is parameter used for acceptance efficiency correction. The data are from Au-Au collisions at $\sqrt{s_{\mathrm{NN}}} = 27$ GeV.

6.1.5 Systematic uncertainties

To estimate the systematic uncertainties, the following sources were considered:

- Comparison of the IMM and EPM, see Fig. 6.13 and Fig. 6.14 - the differences between the mean values are considered as the systematic uncertainty.
  (2% to 20% of the P_Λ and $P_{\overline{\Lambda}}$ for centrality range $20 - 50\%$).

- Uncertainty of the EP resolution $\mathscr{R}_1$, see Tab. 5.4.
  ($\approx 0.1\%$ of the P_Λ and $P_{\overline{\Lambda}}$).

- Uncertainty of the A_0 coefficient, see Tab. 6.5.
  ($\approx 1{\cdot}10^{-3}\%$ of the P_Λ and $P_{\overline{\Lambda}}$).

- Uncertainty of the decay parameter α_{H}, see Tab. 3.2.
  ($\approx 19\%$ of the P_Λ and $\approx 16\%$ of the $P_{\overline{\Lambda}}$).

- The feed-down effect is expected to suppress the mean polarization by $\approx 15\%$ [10]. The KFPF should reduce the feed-down effect nevertheless it is not possible to recognize how many secondary hyperons were reconstructed. For sake of simplicity, the expected asymmetric systematic uncertainty is considered as 15% of the P_Λ and $P_{\overline{\Lambda}}$.

The mean values of the P_{H} for Λ and $\overline{\Lambda}$ hyperon are calculated as

$$\overline{P_{\mathrm{H}}} = \frac{\sum_{i=1}^{2} p_i P_{\mathrm{H,i}}}{\sum_{i=1}^{2} p_i} \qquad \text{and} \qquad \sigma_{\mathrm{stat.}} = \sqrt{\frac{1}{\sum_{i=1}^{2} p_i}} \qquad (6.16)$$

with

$$p_i = \frac{1}{\sigma_{\mathrm{stat.},i}^2}, \qquad (6.17)$$

where the subscript i stands for the IMM and EPM and σ represents the related statistic standard deviation. The final global hyperon polarization including the statistic and systematic uncertainties is gathered in Tab. 6.6 and in Fig. 6.15.

C [%]	P_Λ	$P_{\overline{\Lambda}}$
0-5	$1.01 \pm 0.06(\text{stat.})\ ^{+0.44}_{-0.41}(\text{syst.})$	$0.6 \pm 0.1(\text{stat.}) \pm 1.0(\text{syst.})$
5-10	$0.64 \pm 0.04(\text{stat.})\ ^{+0.39}_{-0.38}(\text{syst.})$	$0.44 \pm 0.08(\text{stat.}) \pm 0.76(\text{syst.})$
10-20	$0.59 \pm 0.03(\text{stat.})\ ^{+0.14}_{-0.11}(\text{syst.})$	$0.44 \pm 0.06(\text{stat.})\ ^{+0.15}_{-0.13}(\text{syst.})$
20-30	$0.59 \pm 0.04(\text{stat.})\ ^{+0.15}_{-0.12}(\text{syst.})$	$0.48 \pm 0.07(\text{stat.})\ ^{+0.13}_{-0.10}(\text{syst.})$
30-40	$0.65 \pm 0.05(\text{stat.})\ ^{+0.20}_{-0.18}(\text{syst.})$	$0.59 \pm 0.08(\text{stat.})\ ^{+0.17}_{-0.15}(\text{syst.})$
40-50	$0.86 \pm 0.07(\text{stat.})\ ^{+0.21}_{-0.17}(\text{syst.})$	$0.6 \pm 0.1(\text{stat.}) \pm 0.2(\text{syst.})$
50-60	$0.9 \pm 0.1(\text{stat.}) \pm 0.2(\text{syst.})$	$0.6 \pm 0.2(\text{stat.}) \pm 0.3(\text{syst.})$
60-70	$1.1 \pm 0.2(\text{stat.}) \pm 0.3(\text{syst.})$	$-0.03 \pm 0.35(\text{stat.}) \pm 0.01(\text{syst.})$
70-80	$2.3 \pm 0.8(\text{stat.})\ ^{+0.8}_{-0.7}(\text{syst.})$	$3 \pm 1(\text{stat.}) \pm 7(\text{syst.})$

Table 6.6: The global polarization P_{H} for Λ and $\overline{\Lambda}$ with $p_{\mathrm{T}} < 0.5$ GeV/c and $|y| < 1$ in Au-Au collisions at 27 GeV.
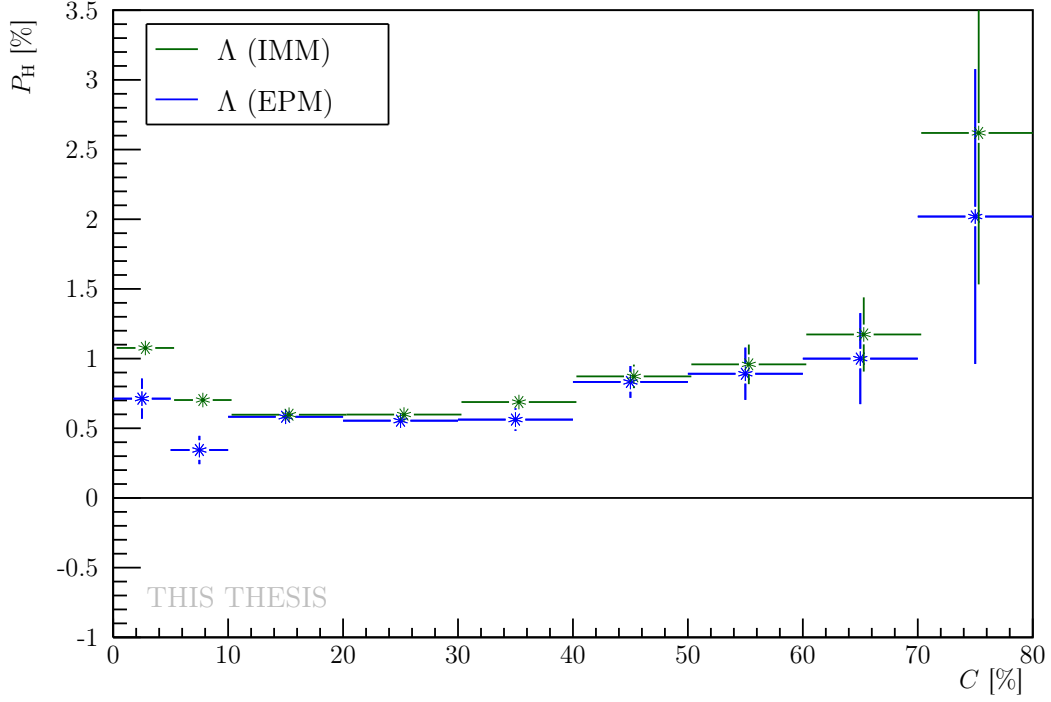
Figure 6.13: Comparison of global polarization P_H from the IMM and EPM method, as a function of centrality C for Λ with $p_\mathrm{T} > 0.5$ GeV/c and $|y| < 1$ in Au-Au collisions at $\sqrt{s_\mathrm{NN}} = 27$ GeV where the acceptance correction is applied. Results for IMM are slightly shifted to the right for clarity.

Figure 6.14: Comparison of global polarization P_H from the IMM and EPM method, as a function of centrality C for $\overline{\Lambda}$ with $p_\mathrm{T} > 0.5$ GeV/c and $|y| < 1$ in Au-Au collisions at $\sqrt{s_\mathrm{NN}} = 27$ GeV where the acceptance correction is applied. Results for EPM are slightly shifted to the right for clarity.
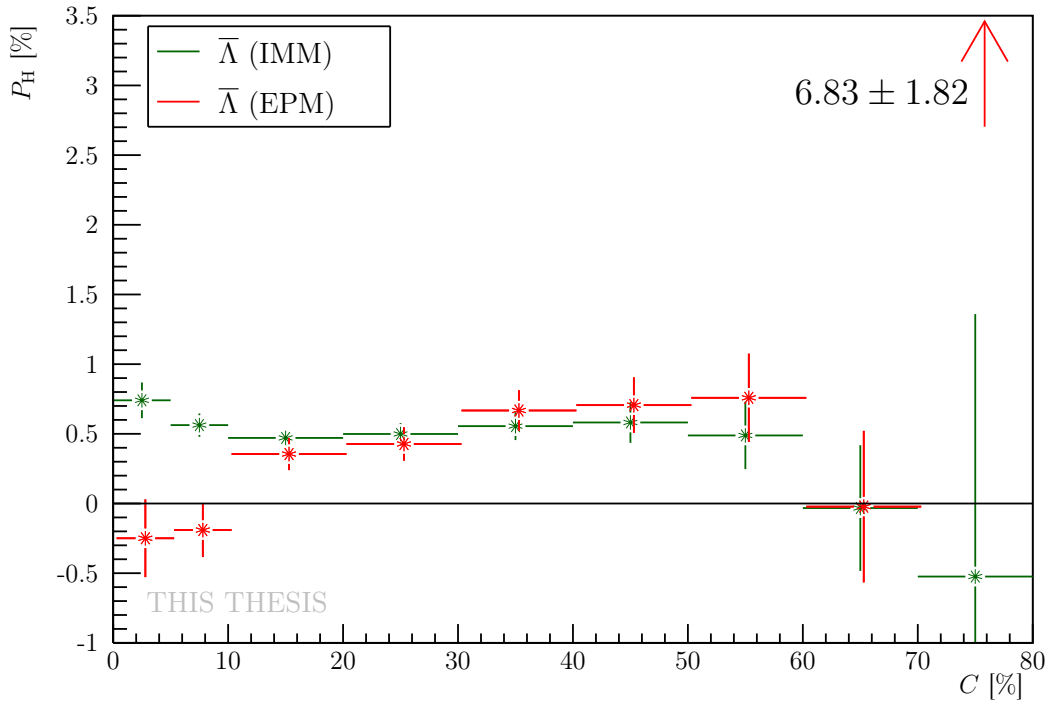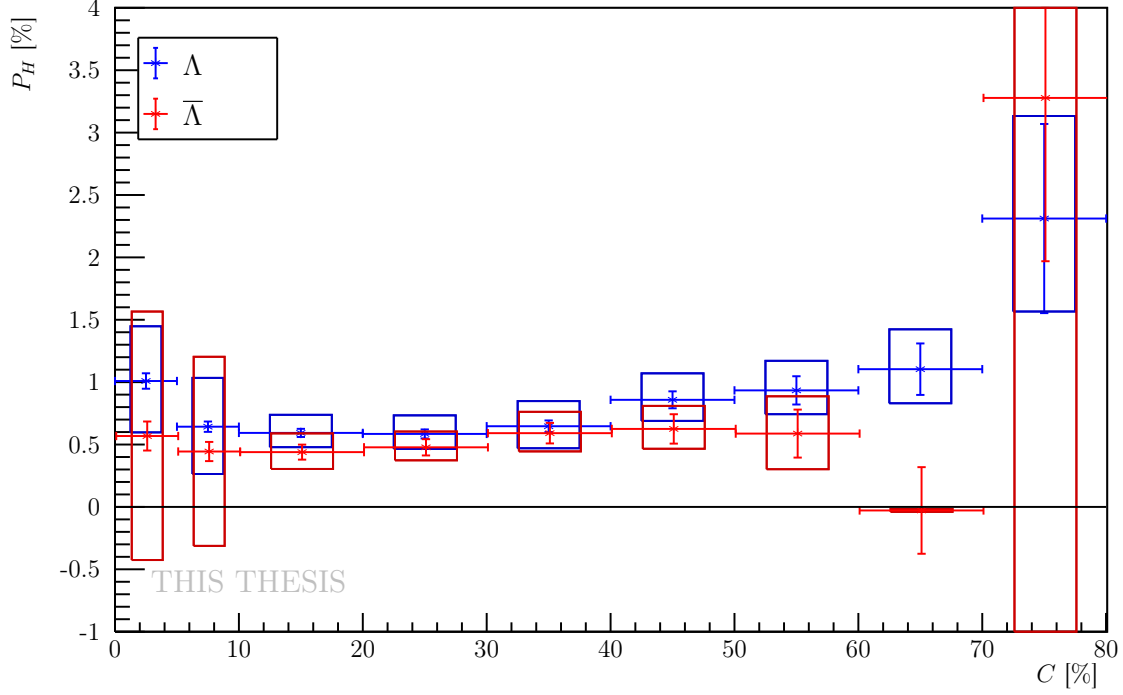
Figure 6.15: The global polarization P_H as a function of centrality C for Λ and $\overline{\Lambda}$ hyperon with $p_\mathrm{T} > 0.5$ GeV/c and $|y| < 1$ in Au-Au collisions at $\sqrt{s_\mathrm{NN}} = 27$ GeV where the acceptance correction is applied.

6.2 Polarization from a hydrodynamic simulation

For purpose of the hydrodynamic simulation of the global Λ hyperon polarization in Au-Au collisions at $\sqrt{s_\mathrm{NN}} = 27$ GeV, the different initial conditions SMASH and GLISSANDO were chosen. In both cases, the initial conditions were averaged from 1000 events. The centrality range was chosen as $20 - 50\%$ which corresponds to the impact parameter range $b = 6.6$-10.4 fm for ^{197}Au nuclei.

The hydrodynamic evolution is calculated with vHLLE code with parameters gathered in Tab. 6.7. The bulk viscosity ζ of the medium is neglected.

τ_0 [fm/c]	$R_\perp$ [fm]	R_η [fm]	η/s
0.89	1.0	0.4	0.12

Table 6.7: The model parameters used to reproduce the experimental data of Au-Au collisions at $\sqrt{s_\mathrm{NN}} = 27$ GeV where τ_0 is the passing time of two nuclei, η/s is the shear viscosity to entropy ratio, and R_η and $R_\perp$ are the transverse and longitudinal smearing parameters, respectively.

Then, two different equations to extract the polarization were applied. The first one, see Eq. (4.33) and Eq. (4.35), considers the polarization induced by thermal vorticity ϖ and thermal shear ξ. The other one, see Eq. (4.41), considers the isothermal local

100

equilibrium. The results of the all above-mentioned are depicted in Fig. 6.16. The comparison of the global Λ polarization P_Λ between the results of the simulation, results published in Nature and result presented in this thesis are shown in Fig. 6.17.
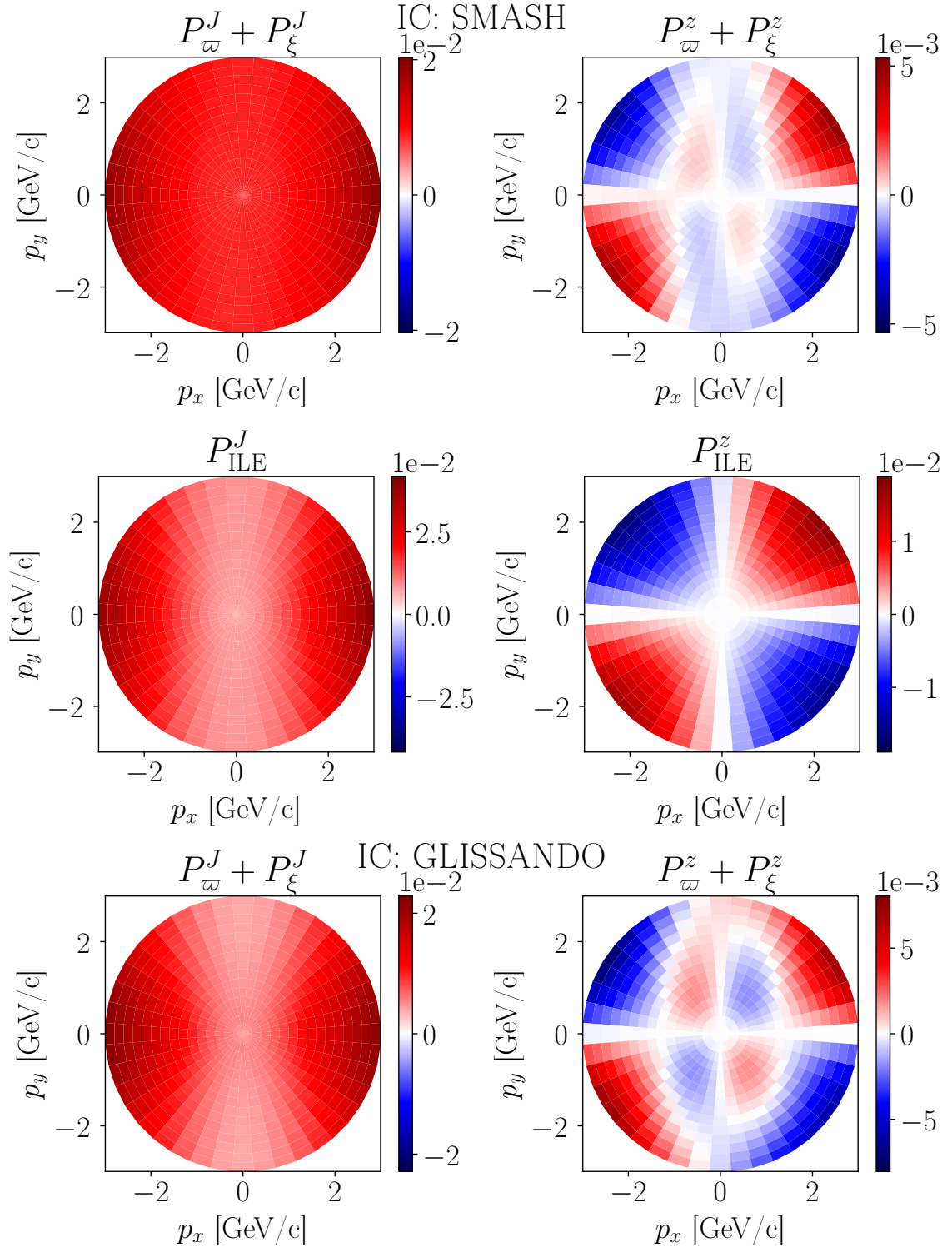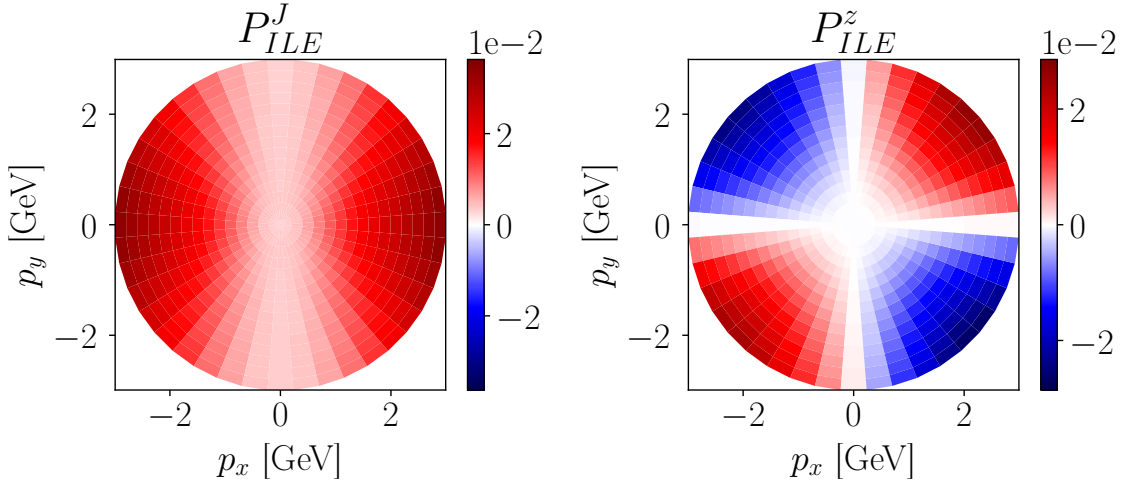
Figure 6.16: Components of Λ polarization $P^{J,z}$ where J and z stand for the angular momentum and the beam axis direction, respectively, at mid-rapidity as a function of the transverse momentum p_{T}, computed by vHLLE with the SMASH and GLISSANDO initial condition (IC) for Au-Au collisions at $\sqrt{s_{\mathrm{NN}}} = 27$ GeV with centrality $20 - 50\%$. See text for more details.
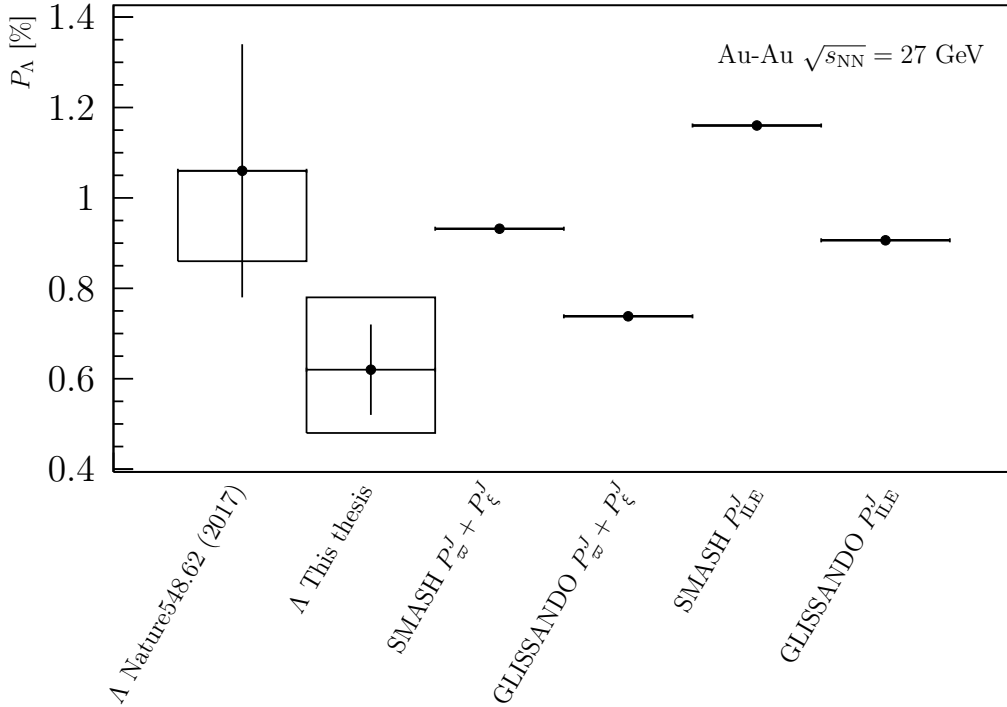

Figure 6.17: Comparison of Λ polarization at mid-rapidity $|y| < 1$ for Λ with $p_{\mathrm{T}} > 0.5$ GeV/c in Au-Au collisions and computed by vHLLE with the SMASH or GLISSANDO initial condition at $\sqrt{s_{\mathrm{NN}}} = 27$ GeV with centrality $20 - 50\%$. See text for more details.

Chapter 7

Discussion

In chapter 5, the first-order EP Ψ_1 was reconstructed using various correction methods. The final Ψ_1 distribution for the last iteration step (IV), see Fig. 5.6, is unambiguously flat concerning the first two iteration (I) and (II). It should be noted, that the third iteration (III) seems to be closest to the uniform distribution. Hence, there arises a question of whether the higher subsequent iterations deteriorate the uniformity of the distribution or whether it is just insubstantial random fluctuation. The reason why one expects the uniform distribution is that the orientation of the reaction plane is determined by the impact parameter $\vec{b}$ which should be uniformly distributed concerning its angle in the transverse plane of a collision.

The resolution of the EP $\mathscr{R}_1$, see Fig. 5.7, does not change from the second iteration except for the most peripheral collisions with centrality $70 - 80\%$. Before the EPD was installed at STAR, the first-order EP including its resolution had been measured using the BBC and the resolution had been more than 1.4 times worse for collisions at $\sqrt{s_{\mathrm{NN}}} = 27$ GeV than now [142]. Since the resolution is larger than 0.5 for centralities $20 - 40\%$, generally the approximation of the resolution in Eq. (3.62) was not applied.

The daughter angular distribution in the laboratory frame was obviously affected by the construction of the TPC, see Fig. 5.9. Nevertheless, since the EP is uniformly distributed, this effect should be canceled out for a large sample of collisions whether the angle ϕ_p is considered with respect to the EP angle Ψ_1. After the boost into the rest frame of a mother particle, the daughter baryon distribution ϕ_p^* is approximately flat, see Fig. 5.10, without any significant sign of the aforementioned effect. The daughter angular distribution with respect to the EP $(\Psi_1 - \phi_p^*)$, see Fig. 5.12 and Fig. 5.11, reveals the expected polarization effect, i.e. one should observe more daughter protons in the direction of the global angular momentum (at $\pi/2$) for Λ hyperon and more daughter antiprotons in the opposite direction (at $3\pi/2$). However, at this stage is too soon to make some conclusions because the distribution is still somehow contaminated with a background.

Alternative way to check whether the non-zero global hyperon polarization is to plot the daughter baryon distribution introduced in Eq. (3.34) using the expression in Eq. (3.35), see Fig. 7.1. In the case of zero polarization, one should see uniform distribution. Since the distribution increases significantly with increasing $\cos\theta^*$, Λ

and $\overline{\Lambda}$ are polarized.
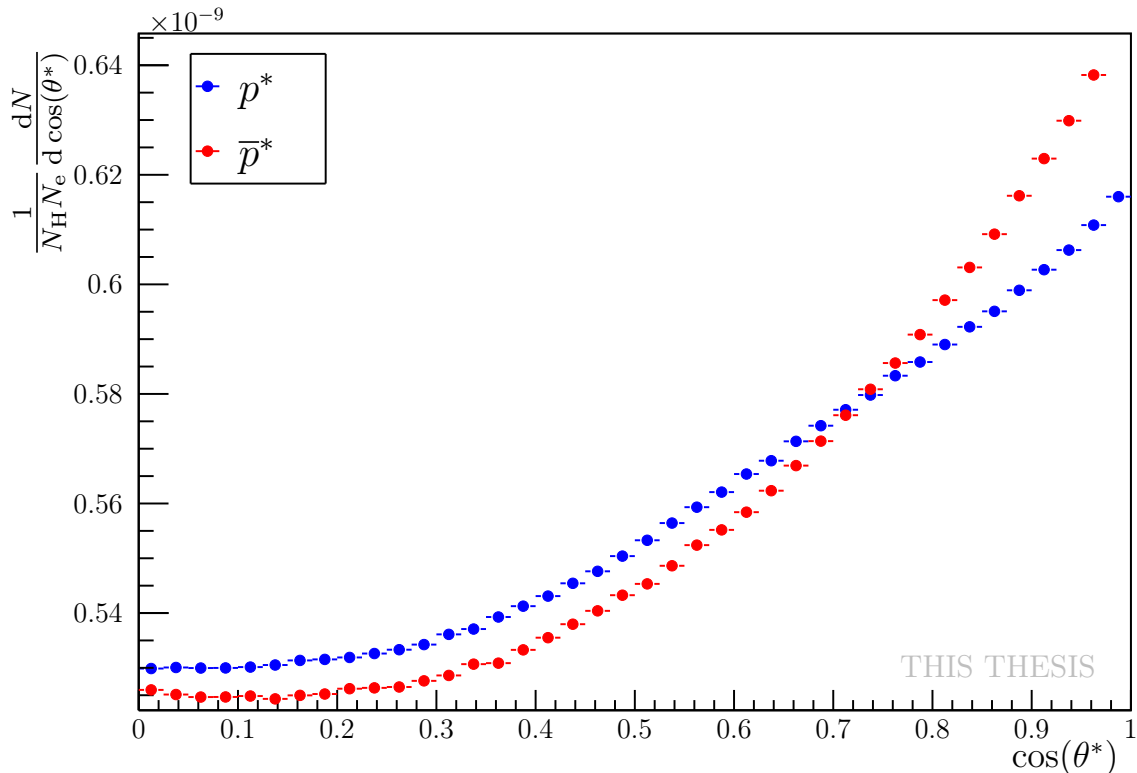

Figure 7.1: The $\cos(\theta^*)$ distribution where θ^* is the polar angle of the daughter proton (p) and antiproton $(\overline{p})$ in the rest frame of the mother Λ and $\overline{\Lambda}$ hyperon, respectively, in Au-Au collisions at $\sqrt{s_{\mathrm{NN}}} = 27$ GeV where N_e is the number of events and N_{H} is the number of the corresponding hyperons.

In order to suppress background and extract the Λ $(\overline{\Lambda})$ global polarization, two methods are used. The invariant mass method and the event plane method, that provided comparable results within one standard deviation for collision centralities in the range $10 - 70\%$, see Fig. 6.13 and Fig. 6.14. The most interesting range for polarization studies is centrality range $20 - 50\%$ or $20 - 60\%$ where the creation of the QGP is expected and concurrently the global angular momentum reaches the highest values, see Fig. 7.2. On the other hand, the best conditions for creating of the QGP are in the most central collisions, however, the global angular momentum is relatively weak. In most peripheral collisions, the creation of the QGP is less probable, and the global angular momentum is relatively low, as well. In the methods comparison, the discrepancies are observed exactly in the most central $0 - 10\%$ and the most peripheral $70 - 80\%$ collisions where the result is most sensitive to the signal extraction model.

Compare to my previous work, the number of $\Delta\phi$ intervals in the EPM, see examples in Fig. 6.5 and Fig. 6.6, was doubled from 6 to 12 which was possible thanks to the large statistics. During the analysis, it turned out that the six bin is insufficient since

the fit was very sensitive to the shape, and even one deviated value could change the sign of the computed polarization.

The combined results of both methods, see Fig. 6.15, show comparable polarization values within one standard deviation for Λ and $\overline{\Lambda}$ for centrality range $20 - 50\%$, contrary to the previously published results [7] where the $\overline{\Lambda}$ polarization is slightly higher. This is caused by choice of the decay parameter α_H. In this thesis, the decay parameters are $\alpha_\Lambda = 0.732 \pm 0.014$ and $\alpha_{\overline{\Lambda}} = -0.758 \pm 0.012$ which reduced the global $\overline{\Lambda}$ polarization more, see Eq. (6.1). If one considers CP conservation then the decay parameter meets the condition $\alpha_\Lambda = -\alpha_{\overline{\Lambda}}$ which can lead to slightly higher extracted polarization of the $\overline{\Lambda}$ hyperon.
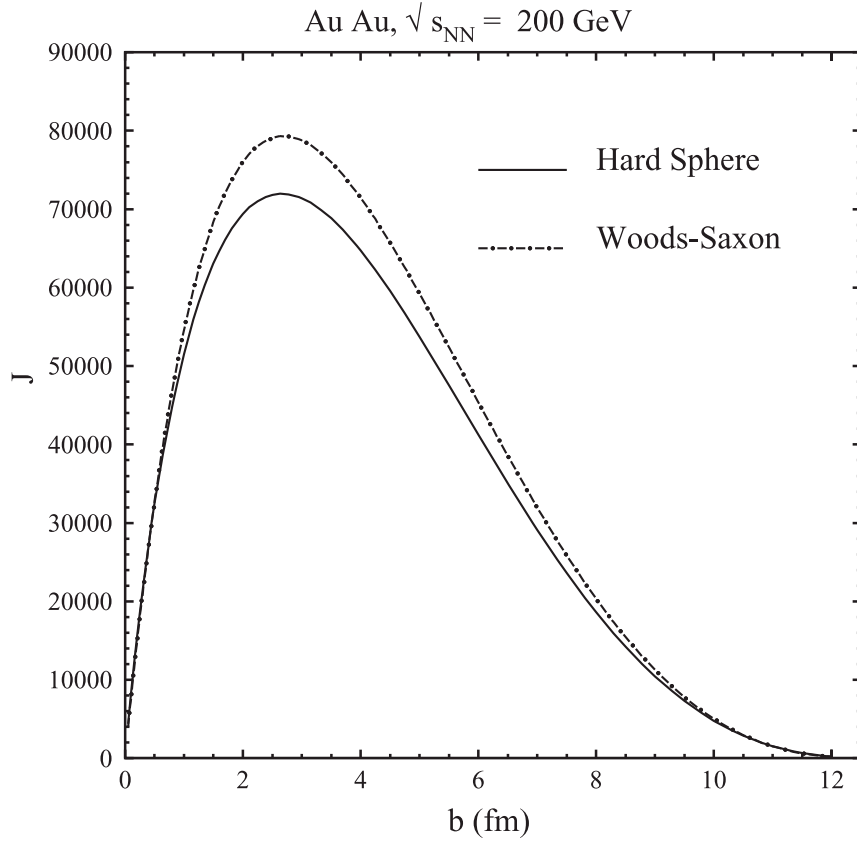

Figure 7.2: Angular momentum J of the interaction region with dependence on the impact parameter b in Au-Au collisions at $\sqrt{s_{NN}} = 200$ GeV [143].

The polarization for the centrality range $20 - 50\%$ was computed as the weighted average of the centrality subranges $20 - 30\%$, $30 - 40\%$, and $40 - 50\%$ where the weight was chosen as the signal yield S for the given subrange. The final results $P_\Lambda^{20-50\%} = 0.62 \pm 0.10(\text{stat.})^{+0.16}_{-0.14}(\text{syst.})\%$ and $P_{\overline{\Lambda}}^{20-50\%} = 0.58 \pm 0.06(\text{stat.})^{+0.17}_{-0.14}(\text{syst.})\%$ are $\approx 40\%$ and $\approx 50\%$ lower than the published results [7], respectively, but still in agreement within the statistic and systematic uncertainties.

The impact of the helicity efficiency, see Fig. 6.10, where the influence has a sinusoidal shape, cancels out if one integrates the global hyperon polarization over all azimuthal angles ϕ_H.

The overall impact of the acceptance efficiency in the first order is approximately 2.5% increase of the observed polarization. Since the second order polarization $P_{\mathrm{H}}^{(\check{2})}$ was not measured, the second order acceptance coefficient A_2 is neglected.

Following systematic uncertainties were considered: the difference between the IMM and EPM method, the uncertainty of the EP resolution $\mathscr{R}_1$, A_0 coefficient, decay parameter α_{H}, and the feed-down effect. Other sources of the systematic uncertainties, such as the tracking efficiency, fitting range of the invariant mass methods, and A_2 coefficient, were neglected. Nevertheless, they should be studied in further work if they significantly influence the extracted polarization.

The feed-down effect, i.e. polarization contribution from non-primary hyperons, was considered as a decrease of the polarization by 15%. Fraction of the non-primary Λ is rejected by the selection criteria applied in KFPF. Nevertheless, it is not feasible to reject all of them. Hence, the reduction of the polarization should be lower than 15%. However, more detail studies using simulation would need to be performed in order to extract the exact feed-down fraction in this analysis. Therefore a conservative number of 15% was used here.

Regarding the hydrodynamic simulations, see Fig. 6.17, all of the results are consistent within statistic and systematic uncertainties with results published in Nature. Considering two possible polarization approaches (thermal vorticity ϖ + thermal shear ξ and isothermal local equilibrium ILE), the model predicts higher polarization in the case of the ILE for both initial conditions generated by SMASH and GLISSANDO. Only the polarization value $P_{\varpi}^J + P_{\xi}^J$ predicted by the model with the SMASH initial condition is not comparable within 3 standard deviations with the global Λ polarization computed in this thesis. Nevertheless, it should be helpful to evaluate uncertainties of the predicted polarization values which is a complicated process and will be performed in my following work. It could be concluded that the angle integrated polarization P^J is reasonable considering the published results for all initial condition and approaches. The main distinction one can find in the longitudinal polarization, see Fig. 6.16, where the p_{T} dependence of the longitudinal polarization P^z is significantly different, namely only the ILE approach produces the right sign of P^z and correct $P^J(\phi)$ dependence.

Conclusion

In the thesis, the global Λ and $\overline{\Lambda}$ polarization for various centrality ranges in Au-Au collisions at $\sqrt{s_{\mathrm{NN}}} = 27$ GeV from the STAR experiment was successfully computed.

Data from the STAR event plane detector were utilized to reconstruct the first-order event plane as an intermediate step. By applying multiple corrections, including phi-weighting, eta-weighting, and psi-shifting, an angle of the event plane Ψ_1 was refined. Next, the resolution of the event plane $\mathscr{R}_1$ for various centrality ranges was evaluated.

As a next step, the KF Particle Finder was employed to reconstruct the primary Λ and $\overline{\Lambda}$ candidates. Various topological cuts were applied to suppress background and non-primary contributions. Following the candidate identification, the related daughter baryon distributions in the rest frame of the mother hyperon ϕ_p^* was obtained.

The polarization signal $\langle \sin(\Psi_1 - \phi_p^*) \rangle$ was extracted using the invariant mass method and event plane method. In both cases, the goal is to extract the Λ and $\overline{\Lambda}$ global polarization and to disentangle it from the background polarization. The results coming from those models are comparable within one standard deviation for centralities between $10 - 70\%$.

In the final stage, the helicity efficiency was discussed and it was demonstrated that its effect cancels out if ϕ_{H}-dependent global hyperon polarization P_{H} is not considered. Next, the acceptance efficiency correction taking into account the imperfection of a detector was discussed and applied to refine the final global hyperon polarization P_{H}. The final extracted global polarizations ($P_{\Lambda}^{20-50\%} = 0.62 \pm 0.10(\mathrm{stat.})_{-0.14}^{+0.16}(\mathrm{syst.})\%$ and $P_{\overline{\Lambda}}^{20-50\%} = 0.58 \pm 0.06(\mathrm{stat.})_{-0.14}^{+0.17}(\mathrm{syst.})\%$) are in agreement with the published results in Nature [7] within the statistic and systematic uncertainties

In addition to the measurement, a hydrodynamic simulation of the global hyperon polarization in Au-Au collisions at $\sqrt{s_{\mathrm{NN}}} = 27$ GeV was presented. The initial conditions were provided by the SMASH and the GLISSANDO models. The hydrodynamic stage was calculated using the 3+1D viscous hydrodynamic code vHLLE. For the polarization evaluation, two different approaches were applied: thermal vorticity and thermal shear contribution and isothermal local equilibrium. In case of the integrated global polarization for the above-mentioned collisions with centrality $20 - 50\%$, the results ($P_{\Lambda}^{\mathrm{model}} \approx 0.74 - 1.16\%$) were comparable with the published ones considering statistical and systematic uncertainties. In comparison with the data analyzed in this thesis considering the systematic uncertainties all data predicted by the hydro

simulations were consistent within 3 standard deviations except for the simulation with the initial state generated by the SMASH model using the isothermal local equilibrium assumption.

In the next work, the additional systematic uncertainties (the tracking efficiency, fitting range of the invariant mass method or variation of selection criteria) will be studied to provide more accurate results and the uncertainties of the hydrodynamic simulation will be evaluated.

Bibliography

[1] YAGI, Kohsuke, Tetsuo HATSUDA, and Yasuo MIAKE. Quark-Gluon plasma: from big bang to little bang. Cambridge University Press, 2008. ISBN 9780521089241.

[2] PASECHNIK, Roman, and Michal ŠUMBERA. Phenomenological review on quark–gluon plasma: concepts vs. observations. Online. Universe, vol. 3 (January 2017), no. 1, p. 7. ISSN 2218-1997. Available from: `https://doi.org/10.3390/universe3010007`. [viewed 2022-04-23].

[3] SHI, Shuzhe. Soft and hard probes of QCD topological structures in relativistic heavy-ion collisions. Springer, 2019. ISBN 9783030254810.

[4] STOCK, R. (ed.). Relativistic heavy ion physics. Online. Berlin, Heidelberg: Springer Berlin Heidelberg, 2010. ISBN 9783642015380. Available from: `https://doi.org/10.1007/978-3-642-01539-7`. [viewed 2022-04-23].

[5] ALVER, B., and G. ROLAND. Collision-geometry fluctuations and triangular flow in heavy-ion collisions. Online. Physical Review C, vol. 81 (May 2010), no. 5. ISSN 1089-490X. Available from: `https://doi.org/10.1103/physrevc.81.054905`. [viewed 2022-04-23].

[6] SATZ, Helmut. Extreme states of matter in strong interaction physics: an introduction. Springer, 2018. ISBN 9783319718934.

[7] Global Λ hyperon polarization in nuclear collisions. Online. Nature, vol. 548 (August 2017), no. 7665, pp. 62–65. ISSN 1476-4687. Available from: `https://doi.org/10.1038/nature23004`. [viewed 2022-04-23].

[8] BECATTINI, Francesco, and Michael A. LISA. Polarization and vorticity in the quark–gluon plasma. Online. Annual Review of Nuclear and Particle Science, vol. 70 (October 2020), no. 1, pp. 395–423. ISSN 1545-4134. Available from: `https://doi.org/10.1146/annurev-nucl-021920-095245`. [viewed 2022-04-23].

[9] KISEL, Ivan. Real-Time event reconstruction and analysis in CBM and STAR experiments. Online. Journal of Physics: Conference Series, vol. 1602 (July 2020), p. 012006. ISSN 1742-6596. Available from: `https://doi.org/10.1088/1742-6596/1602/1/012006`. [viewed 2022-04-23].

[10] KARPENKO, Iu., and F. BECATTINI. Study of Λ polarization in relativistic nuclear collisions at $\sqrt{s_{\mathrm{NN}}} = 7.7$ –200 GeV. Online. The European Physical Journal C, vol. 77 (April 2017), no. 4. ISSN 1434-6052. Available from: `https://doi.org/10.1140/epjc/s10052-017-4765-1`. [viewed 2022-04-23].

[11] WEI, De-Xian, Wei-Tian DENG, and Xu-Guang HUANG. Thermal vorticity and spin polarization in heavy-ion collisions. Online. Physical Review C, vol. 99 (January 2019), no. 1. ISSN 2469-9993. Available from: `https://doi.org/10.1103/physrevc.99.014905`. [viewed 2022-04-23].

[12] CONTRIBUTORS TO WIKIMEDIA PROJECTS. Standard model - wikipedia. Online. Wikipedia, the free encyclopedia. 2002-04-04. Available from: `https://en.wikipedia.org/wiki/Standard_Model`. [viewed 2022-04-23].

[13] AAD, G., T. ABAJYAN, B. ABBOTT, J. ABDALLAH, S. ABDEL KHALEK, et al. Observation of a new particle in the search for the Standard Model Higgs boson with the ATLAS detector at the LHC. Online. Physics Letters B, vol. 716 (September 2012), no. 1, pp. 1–29. ISSN 0370-2693. Available from: `https://doi.org/10.1016/j.physletb.2012.08.020`. [viewed 2022-04-23].

[14] ALTARELLI, Guido. The higgs and the excessive success of the standard model. Online. 2014, p. 19. Available from: `https://doi.org/10.48550/arXiv.1407.2122`.

[15] SARKAR, Sourav, Helmut SATZ, and Bikash SINHA (eds.). The physics of the quark-gluon plasma. Online. Berlin, Heidelberg: Springer Berlin Heidelberg, 2010. ISBN 9783642022852. Available from: `https://doi.org/10.1007/978-3-642-02286-9`. [viewed 2022-04-23].

[16] DISSERTORI, Günther. The determination of the strong coupling constant. Online. Advanced Series on Directions in High Energy Physics, 2016. Available from: `https://doi.org/10.48550/arXiv.1506.05407`. [viewed 2022-04-28].

[17] BARTKE, J. Introduction to relativistic heavy ion physics. Singapore: World Scientific, 2009. ISBN 9789810212315.

[18] CHERNODUB, Maxim N. Background magnetic field stabilizes QCD string against breaking. Online. 2010. Available from: `https://doi.org/10.1142/s0217732314501624`. [viewed 2022-04-23].

[19] AN, Xin, Marcus BLUHM, Lipei DU, Gerald V. DUNNE, Hannah ELFNER, et al. The BEST framework for the search for the QCD critical point and the chiral magnetic effect. Online. Nuclear Physics A, vol. 1017 (January 2022), p. 122343. ISSN 0375-9474. Available from: `https://doi.org/10.1016/j.nuclphysa.2021.122343`. [viewed 2022-04-23].

[20] HEINZ, Ulrich, and Maurice JACOB. Evidence for a new state of matter: an assessment of the results from the CERN lead beam programme. Online. 2000, p. 7. Available from: `https://arxiv.org/abs/nucl-th/0002042`. [viewed 2022-04-23].

[21] RAFELSKI, Johann. Discovery of quark-gluon plasma: strangeness diaries. Online. The European Physical Journal Special Topics, vol. 229 (January 2020), no. 1, pp. 1–140. ISSN 1951-6401. Available from: `https://doi.org/10.1140/epjst/e2019-900263-x`. [viewed 2022-04-23].

[22] BAZAVOV, A., H. T. DING, P. HEGDE, O. KACZMAREK, F. KARSCH, et al. Chiral crossover in QCD at zero and non-zero chemical potentials. Online. Physics Letters B, vol. 795 (August 2019), pp. 15–21. ISSN 0370-2693. Available from: `https://doi.org/10.1016/j.physletb.2019.05.013`. [viewed 2022-04-23].

[23] ODYNIEC, Grazyna, and STAR. Beam energy scan program at RHIC (BES I and BES II) – probing QCD phase diagram with heavy-ion collisions. Online. PoS, vol. CORFU2018 (2019), p. 151. Available from: `https://doi.org/10.22323/1.347.0151`.

[24] KIRSCH, Johannes, Stefan SCHRAMM, Jan STEINHEIMER-FROSCHAUER, and Horst STÖCKER (eds.). Discoveries at the frontiers of science. Online. Cham: Springer International Publishing, 2020. ISBN 9783030342333. Available from: `https://doi.org/10.1007/978-3-030-34234-0`. [viewed 2022-04-23].

[25] NIIDA, T., and Y. MIAKE. Signatures of QGP at RHIC and the LHC. Online. AAPPS Bulletin, vol. 31 (May 2021), no. 1. ISSN 2309-4710. Available from: `https://doi.org/10.1007/s43673-021-00014-3`. [viewed 2022-04-23].

[26] NONAKA, Toshihiro. Studying the QCD Phase Diagram in RHIC-BES at STAR. Online. JPS Conf. Proc., vol. 26 (2019), p. 6. Available from: `https://doi.org/10.7566/JPSCP.26.024007`. [viewed 2022-04-23].

[27] BEOLÈ, S. Looking for quark gluon plasma in pb-pb collisions at 158 gev/c. Online. 2014, p. 118. Available from: `https://www.researchgate.net/publication/40618661_Looking_for_Quark_Gluon_Plasma_in_Pb-Pb_collisions_at_158_GeVc`. [viewed 2022-04-23].

[28] SNELLINGS, Raimond. Collective expansion at the LHC: selected ALICE anisotropic flow measurements. Online. Journal of Physics G: Nuclear and Particle Physics, vol. 41 (November 2014), no. 12, p. 124007. ISSN 1361-6471. Available from: `https://doi.org/10.1088/0954-3899/41/12/124007`. [viewed 2022-04-23].

[29] DAS, Sruthy Jyothi, Giuliano GIACALONE, Pierre-Amaury MONARD, and Jean-Yves OLLITRAULT. Relating centrality to impact parameter in nucleus-nucleus collisions. Online. Physical Review C, vol. 97 (January 2018), no. 1. ISSN 2469-9993. Available from: `https://doi.org/10.1103/physrevc.97.014905`. [viewed 2022-04-23].

[30] ACHARYA, S., F. T. ACOSTA, D. ADAMOVÁ, J. ADOLFSSON, M. M. AGGARWAL, et al. Transverse momentum spectra and nuclear modification factors of charged particles in pp, p-Pb and Pb-Pb collisions at the LHC. Online.

Journal of High Energy Physics, vol. 2018 (November 2018), no. 11. ISSN 1029-8479. Available from: `https://doi.org/10.1007/jhep11(2018)013`. [viewed 2022-04-23].

[31] IVANOV, Yuri. Directed flow in heavy-ion collisions and its implications for astrophysics. Online. Universe, vol. 3 (November 2017), no. 4, p. 79. ISSN 2218-1997. Available from: `https://doi.org/10.3390/universe3040079`. [viewed 2022-04-23].

[32] BRAVINA, Larissa, Y. KVASIUK, D. SACHENKO, S. Y. SIVOKLOKOV, O. VITIUK, et al. Directed flow and freeze-out in relativistic heavy-ion collisions at NICA and FAIR energies. Online. PoS, vol. CORFU2018 (2019), p. 171. Available from: `https://doi.org/10.22323/1.347.0171`. [viewed 2022-04-23].

[33] CHATRCHYAN, S., V. KHACHATRYAN, A. M. SIRUNYAN, A. TUMASYAN, W. ADAM, et al. Measurement of the elliptic anisotropy of charged particles produced in pbpb collisions atsnn=2.76tev. Online. Physical Review C, vol. 87 (January 2013), no. 1. ISSN 1089-490X. Available from: `https://doi.org/10.1103/physrevc.87.014902`. [viewed 2022-04-23].

[34] MILOSEVIC, J. Triangular flow of negative pions emitted in PbAu collisions at top SPS energy. Online. EPJ Web of Conferences, vol. 164 (2017), p. 07054. ISSN 2100-014X. Available from: `https://doi.org/10.1051/epjconf/201716407054`. [viewed 2022-04-23].

[35] ACHARYA, S., D. ADAMOVÁ, A. ADLER, J. ADOLFSSON, M. M. AGGAR-WAL, et al. J/ψ elliptic and triangular flow in Pb-Pb collisions at $\sqrt{s_{\mathrm{NN}}} = 5.02$ TeV. Online. Journal of High Energy Physics, vol. 2020 (October 2020), no. 10. ISSN 1029-8479. Available from: `https://doi.org/10.1007/jhep10(2020)141`. [viewed 2022-04-23].

[36] AGS booster celebrates a quarter-century of service. Online. Brookhaven National Laboratory. 2016-06-27. Available from: `https://www.bnl.gov/newsroom/news.php?a=26425`. [viewed 2022-04-23].

[37] SHILTSEV, V., and F. ZIMMERMANN. Modern and future colliders. Online. Reviews of Modern Physics, vol. 93 (March 2021), no. 1. ISSN 1539-0756. Available from: `https://doi.org/10.1103/revmodphys.93.015006`. [viewed 2022-04-23].

[38] FRASER, Gordon. The quark machines. Online. Taylor & Francis, 1997. ISBN 9780750304474. Available from: `https://doi.org/10.1201/noe0750304474`. [viewed 2022-04-23].

[39] BAYM, G. RHIC: from dreams to beams in two decades. Online. Nuclear Physics A, vol. 698 (February 2002), no. 1-4, pp. xxiii—xxxii. ISSN 0375-9474. Available from: `https://doi.org/10.1016/s0375-9474(01)01342-2`. [viewed 2022-04-23].

[40] Electron beam ion source pre-injector project (ebis). Online. BNL-73700-2005-IR-R1. Upton: Brookhaven National Laboratory, 2005. Available from: `https://www.bnl.gov/isd/documents/30527.pdf`. [viewed 2022-04-23].

[41] LITVINENK, V. N., Y. LUO, V. PTITSYN, T. SATOGATA, S. TEPIKIAN, et al. Experience with IBS-suppression lattice in RHIC. Online. BNL-81335-2008-CP. Upton: Brookhaven National Laboratory, 2008. Available from: `https://www.bnl.gov/isd/documents/43238.pdf`. [viewed 2022-04-23].

[42] TANNENBAUM, Michael J. Latest results from RHIC + progress on determining $\hat{q}$L in RHI collisions using di-hadron correlations. Online. Universe, vol. 5 (June 2019), no. 6, p. 140. ISSN 2218-1997. Available from: `https://doi.org/10.3390/universe5060140`. [viewed 2022-04-23].

[43] SPHENIX beam use proposal. Online. SPH-TRG-2020-001. 2020. Available from: `https://indico.bnl.gov/event/7881/attachments/30176/47160/sPH-TRG-2020-001.pdf`. [viewed 2022-05-01].

[44] PÉREZ LARA, Carlos E. The sPHENIX Experiment. Online. EPJ Web of Conferences, vol. 171 (2018), p. 10002. ISSN 2100-014X. Available from: `https://doi.org/10.1051/epjconf/201817110002`. [viewed 2022-04-23].

[45] ALESSI, J., E. BEEBE, S. BINELLO, L. HOFF, K. KONDO, et al. Commissioning of the ebis-based heavy ion preinjector at brookhaven. Online. Proceedings - 25th Linear Accelerator Conference, LINAC 2010, 2011. Available from: `https://www.researchgate.net/publication/228575492`. [viewed 2022-04-23].

[46] ROSER, Thomas, W. W. MACKAY, I. ALEKSEEV, Mei BAI, Keonta BROWN, et al. Configuration manual polarized proton collider at rhic. Online. 2001. Available from: `https://doi.org/10.2172/15011215`. [viewed 2022-04-23].

[47] VOSSBERG, M., J. SCHMIDT, B. HOFMANN, A. SCHEMPP, C. ZHANG, et al. The new EBIS RFQ for BNL. Online. Proceedings of LINAC08, 2008, p. 3. Available from: `https://accelconf.web.cern.ch/linac08/papers/mop033.pdf`. [viewed 2022-04-23].

[48] SCHEMPP, Alwin, Ulrich RATZINGER, Chuan ZHANG, Deepak RAPARIA, R. TIEDE, et al. RFQ AND IH accelerators for the new EBIS injector at BNL. Online. Proceedings of PAC07, 2007. Available from: https://www.researchgate.net/publication/224304685. [viewed 2022-04-23].

[49] EDELEN, Jonathan, Kevin BROWN, Nathan COOK, and Philip DYER. Optimal control for rapid switching of beam energies for the ATR line at BNL. Online. Proceedings, 17th International Conference on Accelerator and Large Experimental Physics Control Systems, ICALEPCS2019, 2019, p. 6. ISSN 2226-0358. Available from: `https://doi.org/10.18429/JACoW-ICALEPCS2019-TUCPL07`. [viewed 2022-04-23].

[50] TSOUPAS, N., W. FISCHER, J. KEWISCH, W. W. MACKAY, S. PEGGS, et al. Focusing and matching properties of the AtR transfer line. Online. Proceedings of the 1997 Particle Accelerator Conference (Cat. No.97CH36167), vol. 1 (1997). Available from: `https://doi.org/10.1109/PAC.1997.749599`. [viewed 2022-04-23].

[51] LUO, Y., W. FISCHER, and S. WHITE. Analysis and modeling of proton beam loss and emittance growth in the Relativistic Heavy Ion Collider. Online. Physical Review Accelerators and Beams, vol. 19 (February 2016), no. 2. ISSN 2469-9888. Available from: `https://doi.org/10.1103/physrevaccelbeams.19.021001`. [viewed 2022-04-23].

[52] NAGLE, J. L., and T. S. ULLRICH. Heavy ion experiments at RHIC: the first year. Online. QCD Perspectives on Hot and Dense Matter, 2002, p. 50. Available from: `https://doi.org/10.48550/arxiv.nucl-ex/0203007`. [viewed 2022-04-23].

[53] MONTAG, Christoph. RHIC status and plans. Online. AIP Conference Proceedings, vol. 2160 (2019). Available from: `https://doi.org/10.1063/1.5127686`. [viewed 2022-04-23].

[54] RHIC run overview. Online. Page Moved. [n.d.]. Available from: `https://www.rhichome.bnl.gov/RHIC/Runs/`. [viewed 2022-04-23].

[55] YANG, Qian. The STAR BES-II and forward rapidity physics and upgrades. Online. Nuclear Physics A, vol. 982 (February 2019), pp. 951–954. ISSN 0375-9474. Available from: `https://doi.org/10.1016/j.nuclphysa.2018.10.029`. [viewed 2022-04-23].

[56] YE, Zhenyu. Heavy flavor production in high energy nuclear collisions & forty years of quark-gluon plasma. Online. Indico. 2018. Available from: `https://indico.cern.ch/event/732540/contributions/3260184/`. [viewed 2022-04-23].

[57] ANDERSON, M., J. BERKOVITZ, W. BETTS, R. BOSSINGHAM, F. BIESER, et al. The STAR time projection chamber: a unique tool for studying high multiplicity events at RHIC. Online. Nuclear Instruments and Methods in Physics Research Section A: Accelerators, Spectrometers, Detectors and Associated Equipment, vol. 499 (March 2003), no. 2-3, pp. 659–678. ISSN 0168-9002. Available from: `https://doi.org/10.1016/s0168-9002(02)01964-2`. [viewed 2022-04-23].

[58] LLOPE, W. J. The large-area time-of-flight upgrade for STAR. Online. Nuclear Instruments and Methods in Physics Research Section B: Beam Interactions with Materials and Atoms, vol. 241 (December 2005), no. 1-4, pp. 306–310. ISSN 0168-583X. Available from: `https://doi.org/10.1016/j.nimb.2005.07.089`. [viewed 2022-04-23].

[59] SHAO, Ming, Olga BARANNIKOVA, Xin DONG, Yuri FISYAK, Lijuan RUAN, et al. Extensive particle identification with TPC and TOF at the STAR experiment. Online. Nuclear Instruments and Methods in Physics Research Section A: Accelerators, Spectrometers, Detectors and Associated Equipment, vol. 558 (March 2006), no. 2, pp. 419–429. ISSN 0168-9002. Available from: `https://doi.org/10.1016/j.nima.2005.11.251`. [viewed 2022-04-23].

[60] BEDDO, M., E. BIELICK, T. FORNEK, V. GUARINO, D. HILL, et al. The STAR barrel electromagnetic calorimeter. Online. Nuclear Instruments and Methods in Physics Research Section A: Accelerators, Spectrometers, Detectors and Associated Equipment, vol. 499 (March 2003), no. 2-3, pp. 725–739. ISSN 0168-9002. Available from: `https://doi.org/10.1016/s0168-9002(02)01970-8`. [viewed 2022-04-23].

[61] THE STAR COLLABORATION. Conceptual design report. Online. PUB-5347. Upton, 1992. Available from: `https://drupal.star.bnl.gov/STAR/files/StarCDR.pdf`. [viewed 2022-04-23].

[62] WHITTEN, C. A., and STAR COLLABORATION. The beam-beam counter: A local polarimeter at STAR. Online. AIP Conference Proceedings, vol. 980 (2008). Available from: `https://doi.org/10.1063/1.2888113`. [viewed 2022-04-23].

[63] LLOPE, W. J., J. ZHOU, T. NUSSBAUM, G. W. HOFFMANN, K. ASSELTA, et al. The STAR vertex position detector. Online. Nuclear Instruments and Methods in Physics Research Section A: Accelerators, Spectrometers, Detectors and Associated Equipment, vol. 759 (September 2014), pp. 23–28. ISSN 0168-9002. Available from: `https://doi.org/10.1016/j.nima.2014.04.080`. [viewed 2022-04-23].

[64] JUDD, E. G., L. C. BLAND, H. J. CRAWFORD, J. ENGELAGE, J. M. LANDGRAF, et al. The evolution of the STAR Trigger System. Online. Nuclear Instruments and Methods in Physics Research Section A: Accelerators, Spectrometers, Detectors and Associated Equipment, vol. 902 (September 2018), pp. 228–237. ISSN 0168-9002. Available from: `https://doi.org/10.1016/j.nima.2018.03.070`. [viewed 2022-04-23].

[65] YANG, C., and Q. YANG. The STAR detector upgrades for the BES-II and at forward rapidity. Online. Journal of Instrumentation, vol. 15 (July 2020), no. 07, p. C07040. ISSN 1748-0221. Available from: `https://doi.org/10.1088/1748-0221/15/07/c07040`. [viewed 2022-04-23].

[66] YANG, Chi. The STAR beam energy scan phase II physics and upgrades. Online. Nuclear Physics A, vol. 967 (November 2017), pp. 800–803. ISSN 0375-9474. Available from: `https://doi.org/10.1016/j.nuclphysa.2017.05.042`. [viewed 2022-04-23].

[67] MEEHAN, Kathryn. STAR results from Au+Au fixed-target collisions at $\sqrt{s_{\mathrm{NN}}}$ = 4.5 GeV. Online. Nuclear Physics A, vol. 967 (November 2017), pp. 808–811. ISSN 0375-9474. Available from: `https://doi.org/10.1016/j.nuclphysa.2017.06.007`. [viewed 2022-04-23].

[68] YANG, Yi. The STAR detector upgrades for the BES II and beyond physics program. Online. Nuclear Physics A, vol. 1005 (January 2021), p. 121758. ISSN 0375-9474. Available from: `https://doi.org/10.1016/j.nuclphysa.2020.121758`. [viewed 2022-04-23].

[69] THE STAR COLLABORATION. The STAR beam use request for run-22 and data taking in 2023-25. Online. Upton, 2020. Available from: `https://drupal.star.bnl.gov/STAR/files/STAR_Beam_Use_Request_Runs22_25.pdf`. [viewed 2022-04-23].

[70] ADAMS, J., A. EWIGLEBEN, S. GARRETT, W. HE, T. HUANG, et al. The STAR event plane detector. Online. Nuclear Instruments and Methods in Physics Research Section A: Accelerators, Spectrometers, Detectors and Associated Equipment, vol. 968 (July 2020), p. 163970. ISSN 0168-9002. Available from: `https://doi.org/10.1016/j.nima.2020.163970`. [viewed 2022-04-24].

[71] COOPER, Daniel. The next U.S. particle accelerator will be built on long island by 2031. Online. Entrepreneur. 2020. Available from: `https://www.entrepreneur.com/article/356548`. [viewed 2022-04-24].

[72] KHALEK, R. A., A. ACCARDI, J. ADAM, D. ADAMIAK, W. AKERS, et al. Science requirements and detector concepts for the electron-ion collider: EIC yellow report. Online. BNL-220990-2021-FORE. arXiv, 2021. Available from: `https://doi.org/10.48550/arXiv.2103.05419`. [viewed 2022-04-24].

[73] U.S. department of energy selects brookhaven national laboratory to host major new nuclear physics facility. Online. Brookhaven National Laboratory. 2020. Available from: `https://www.bnl.gov/newsroom/news.php?a=116996`. [viewed 2022-04-24].

[74] RAVEL, Olivier. Early cosmic ray research in France. Online. AIP Conference Proceedings, vol. 1516 (2013), pp. 67–71. Available from: `https://doi.org/10.1063/1.4792542`. [viewed 2022-04-24].

[75] WROBLEWSKI, A. Hypernuclei (and strange particles)-how it all began? Online. Acta Physica Polonica B, vol. 35 (2004). Available from: `https://www.researchgate.net/publication/228455416_Hypernuclei_and_Strange_Particles-How_It_All_Began`. [viewed 2022-04-24].

[76] VIDAÑA, Isaac. Hyperons: the strange ingredients of the nuclear equation of state. Online. Proceedings of the Royal Society A: Mathematical, Physical and Engineering Sciences, vol. 474 (September 2018), no. 2217, p. 20180145. ISSN 1471-2946. Available from: `https://doi.org/10.1098/rspa.2018.0145`. [viewed 2022-04-24].

[77] FORTIN, M., S. S. AVANCINI, C. PROVIDÊNCIA, and I. VIDAÑA. Hypernuclei and massive neutron stars. Online. Physical Review C, vol. 95 (June 2017), no. 6. ISSN 2469-9993. Available from: `https://doi.org/10.1103/physrevc.95.065803`. [viewed 2022-04-24].

[78] GAL, A., E. V. HUNGERFORD, and D. J. MILLENER. Strangeness in nuclear physics. Online. Reviews of Modern Physics, vol. 88 (August 2016), no. 3. ISSN 1539-0756. Available from: `https://doi.org/10.1103/revmodphys.88.035004`. [viewed 2022-04-24].

[79] ROCHESTERDR., G. D., and C. C. BUTLERDR. Evidence for the existence of new unstable elementary particles. Online. Nature, vol. 160 (December 1947), no. 4077, pp. 855–857. ISSN 1476-4687. Available from: `https://doi.org/10.1038/160855a0`. [viewed 2022-04-24].

[80] SERIFF, A. J., R. B. LEIGHTON, C. HSIAO, E. W. COWAN, and C. D. ANDERSON. Cloud-Chamber observations of the new unstable cosmic-ray particles. Online. Physical Review, vol. 78 (May 1950), no. 3, pp. 290–291. ISSN 0031-899X. Available from: `https://doi.org/10.1103/physrev.78.290`. [viewed 2022-04-24].

[81] GRIFFITHS, David. Introduction to elementary particles. Wiley & Sons, Incorporated, John, 2008. ISBN 9783527618477.

[82] OERTER, Robert. The theory of almost everything. New York: Penguin USA, Inc., 2009. ISBN 9781101120903.

[83] HOPPER, V. D., and S. BISWAS. Evidence concerning the existence of the new unstable elementary neutral particle. Online. Physical Review, vol. 80 (December 1950), no. 6, pp. 1099–1100. ISSN 0031-899X. Available from: `https://doi.org/10.1103/physrev.80.1099`. [viewed 2022-04-24].

[84] ZYLA, P. A et al. Review of particle physics. Online. PTEP, vol. 2020 (2020), no. 8. Available from: `https://pdg.lbl.gov/2021/listings/rpp2021-list-lambda.pdf`. [viewed 2022-04-24].

[85] SMITH, A. C., and P. N. KALONI. A note on spin, vorticity and the deformation-rate tensor. Online. Journal of Non-Newtonian Fluid Mechanics, vol. 62 (January 1996), no. 1, pp. 95–98. ISSN 0377-0257. Available from: `https://doi.org/10.1016/0377-0257(95)01390-3`. [viewed 2022-04-24].

[86] Descriptive physical oceanography. Online. Elsevier, 2011. ISBN 9780750645522. Available from: `https://doi.org/10.1016/c2009-0-24322-4`. [viewed 2022-04-24].

[87] KHARZEEV, D. E., J. LIAO, S. A. VOLOSHIN, and G. WANG. Chiral magnetic and vortical effects in high-energy nuclear collisions—A status report. Online. Progress in Particle and Nuclear Physics, vol. 88 (May 2016), pp. 1–28. ISSN 0146-6410. Available from: `https://doi.org/10.1016/j.ppnp.2016.01.001`. [viewed 2022-04-24].

[88] JAFFE, R. L. Polarized lambdas in the current fragmentation region. Online. Physical Review D, vol. 54 (December 1996), no. 11, pp. R6581—R6585. ISSN 1089-4918. Available from: `https://doi.org/10.1103/physrevd.54.r6581`. [viewed 2022-04-24].

[89] BURKARDT, M., and R. L. JAFFE. Polarized $q \to \Lambda$ fragmentation functions from $e^+e^- \to \Lambda + X^*$. Online. Physical Review Letters, vol. 70 (April 1993), no. 17, pp. 2537–2540. ISSN 0031-9007. Available from: `https://doi.org/10.1103/physrevlett.70.2537`. [viewed 2022-04-24].

[90] DEUR, Alexandre, Stanley J. BRODSKY, and Guy F. DE TÉRAMOND. The spin structure of the nucleon. Online. Reports on Progress in Physics, vol. 82 (June 2019), no. 7, p. 076201. ISSN 1361-6633. Available from: `https://doi.org/10.1088/1361-6633/ab0b8f`. [viewed 2022-04-24].

[91] IRELAND, D. G., M. DÖRING, D. I. GLAZIER, J. HAIDENBAUER, M. MAI, et al. Kaon photoproduction and the Λ decay parameter α^-. Online. Physical Review Letters, vol. 123 (October 2019), no. 18. ISSN 1079-7114. Available from: `https://doi.org/10.1103/physrevlett.123.182301`. [viewed 2022-04-24].

[92] KOCH, W. Determination of the Ξ decay parameters. Online. Proceedings of the 1964 Easter School for Physicists Using the CERN Proton Synchrotron and Synchro-Cyclotron, 1964, pp. 75–112. Available from: `https://doi.org/10.5170/CERN-1964-013-V-2.75`. [viewed 2022-04-24].

[93] ABELEV, B. I., M. M. AGGARWAL, Z. AHAMMED, B. D. ANDERSON, D. ARKHIPKIN, et al. Global polarization measurement in Au+Au collisions. Online. Physical Review C, vol. 76 (August 2007), no. 2. ISSN 1089-490X. Available from: `https://doi.org/10.1103/physrevc.76.024915`. [viewed 2022-04-24].

[94] BURKA, K. The Flow Harmonics Measurement with the Event Plane and Multi-particle Cumulant Methods in Pb+Pb Collisions at 2.76 TeV in ATLAS. Online. Acta Physica Polonica B, vol. 47 (2016), no. 6, p. 1625. ISSN 1509-5770. Available from: `https://doi.org/10.5506/aphyspolb.47.1625`. [viewed 2022-04-24].

[95] IVASHKIN, Alexander, Dmitry FINOGEEV, Marina GOLUBEVA, Fedor GUBER, Alexander IZVESTNYY, et al. Determination of geometry of heavy ion collisions with forward hadron calorimeter (FHCal) at MPD/NICA. Online. EPJ Web of Conferences, vol. 204 (2019), p. 07002. ISSN 2100-014X. Available from: `https://doi.org/10.1051/epjconf/201920407002`. [viewed 2022-04-24].

[96] POSKANZER, A. M., and S. A. VOLOSHIN. Methods for analyzing anisotropic flow in relativistic nuclear collisions. Online. Physical Review C, vol. 58 (September 1998), no. 3, pp. 1671–1678. ISSN 1089-490X. Available from: `https://doi.org/10.1103/physrevc.58.1671`. [viewed 2022-04-24].

[97] LISA, Michael A. EP resolution with the EPD and BBC. Online. The STAR experiment. 2018-05-08. Available from: `https://drupal.star.bnl.gov/STAR/blog/lisa/ep-resolution-epd-and-bbc`. [viewed 2022-04-24].

[98] LISA, Michael A. EPD calibration for Au+Au 2017 (and method in general). Online. The STAR experiment. 2017-10-12. Available from: `https://drupal.star.bnl.gov/STAR/blog/lisa/epd-calibration-auau-2017-and-method-general`. [viewed 2022-04-24].

[99] POSKANZER, A. M., and S. A. VOLOSHIN. Methods for analyzing anisotropic flow in relativistic nuclear collisions. Online. Physical Review C, vol. 58 (September 1998), no. 3, pp. 1671–1678. ISSN 1089-490X. Available from: `https://doi.org/10.1103/physrevc.58.1671`. [viewed 2022-04-24].

[100] VOLOSHIN, Sergei A., Arthur M. POSKANZER, and Raimond SNELLINGS. Collective phenomena in non-central nuclear collisions. Online. arXiv, 2000. Available from: `https://doi.org/10.48550/arxiv.0809.2949`. [viewed 2022-04-24].

[101] LISA, Michael A. Phi-weighting and optimizing ring weights in Au+Au 27 GeV. Online. The STAR experiment. 2018. Available from: `https://drupal.star.bnl.gov/STAR/blog/lisa/phi-weighting-and-optimizing-ring-weights-auau-27-gev#Update6June2018`. [viewed 2022-04-24].

[102] LISA, Michael A. EP resolution and the eta dependence of directed flow in Au+Au collisions. Online. The STAR experiment. 2018. Available from: `https://drupal.star.bnl.gov/STAR/blog/lisa/ep-resolution-and-eta-dependence-directed-flow-auau-collisions`. [viewed 2022-04-24].

[103] JAMES, F. MINUIT function minimization and error analysis: reference manual version 94.1. Online. CERN-D-506. Geneva, 1994. Available from: `https://inspirehep.net/literature/1258343`. [viewed 2022-04-24].

[104] LISA, Michael A. Optimizing EP[1] resolution in Au27Au: from ring-dependent weights to eta-dependent weights. Online. The STAR experiment. 2018. Available from: `https://drupal.star.bnl.gov/STAR/blog/lisa/optimizing-ep1-resolution-au27au-ring-dependent-weights-eta-dependent-weights`. [viewed 2022-04-24].

[105] BARRETTE, J., R. BELLWIED, S. BENNETT, R. BERSCH, P. BRAUN-MUNZINGER, et al. Proton and pion production relative to the reaction plane in Au + Au collisions at 11AGeV/c. Online. Physical Review C, vol. 56 (December 1997), no. 6, pp. 3254–3264. ISSN 1089-490X. Available from: `https://doi.org/10.1103/physrevc.56.3254`. [viewed 2022-04-24].

[106] OLLITRAULT, Jean-Yves. Reconstructing azimuthal distributions in nucleus-nucleus collisions. Online. arXiv, 1997. Available from: `https://doi.org/10.48550/arXiv.nucl-ex/9711003`. [viewed 2022-04-24].

[107] NIIDA, Takafumi. Global polarization and spin alignment measurements. Online. EPJ Web of Conferences, vol. 259 (2022), p. 06002. ISSN 2100-014X. Available from: `https://doi.org/10.1051/epjconf/202225906002`. [viewed 2022-04-24].

[108] ACHARYA, S., D. ADAMOVÁ, S. P. ADHYA, A. ADLER, J. ADOLFSSON, et al. Global polarization of Λ and $\overline{\Lambda}$ hyperons in Pb-Pb collisions at $\sqrt{s_{\mathrm{NN}}}=$ 2.76 and 5.02 TeV. Online. Physical Review C, vol. 101 (April 2020), no. 4. ISSN 2469-9993. Available from: `https://doi.org/10.1103/physrevc.101.044611`. [viewed 2022-04-24].

[109] ADAM, J., L. ADAMCZYK, J. R. ADAMS, J. K. ADKINS, G. AGAKISHIEV, et al. Global polarization of Λ hyperons in Au + Au collisions at $\sqrt{s_{\mathrm{NN}}} = 200$ GeV. Online. Physical Review C, vol. 98 (July 2018), no. 1. ISSN 2469-9993. Available from: `https://doi.org/10.1103/physrevc.98.014910`. [viewed 2022-04-24].

[110] ABDALLAH, M. S., B. E. ABOONA, J. ADAM, L. ADAMCZYK, J. R. ADAMS, et al. Global Λ-hyperon polarization in Au+Au collisions at $\sqrt{s_{\mathrm{NN}}} = 3$ GeV. Online. Physical Review C, vol. 104 (December 2021), no. 6. ISSN 2469-9993. Available from: `https://doi.org/10.1103/physrevc.104.l061901`. [viewed 2022-04-24].

[111] OKUBO, Kosuke. Measurement of global polarization of Λ hyperons in Au+Au $\sqrt{s_{\mathrm{NN}}} = 7.2$ GeV fixed target collisions at RHIC-STAR experiment. Online. EPJ Web of Conferences, vol. 259 (2022), p. 06003. ISSN 2100-014X. Available from: `https://doi.org/10.1051/epjconf/202225906003`. [viewed 2022-04-24].

[112] ADAM, J., L. ADAMCZYK, J. R. ADAMS, J. K. ADKINS, G. AGAK-ISHIEV, et al. Global Polarization of Ξ and Ω Hyperons in Au+Au Collisions at $\sqrt{s_{\mathrm{NN}}}$=200 GeV. Online. Physical Review Letters, vol. 126 (April 2021), no. 16. ISSN 1079-7114. Available from: `https://doi.org/10.1103/physrevlett.126.162301`. [viewed 2022-04-24].

[113] GALE, Charles, Sangyong JEON, and Björn SCHENKE. Hydrodynamic modeling of heavy-ion collisions. Online. International Journal of Modern Physics A, vol. 28 (April 2013), no. 11, p. 1340011. ISSN 1793-656X. Available from: `https://doi.org/10.1142/s0217751x13400113`. [viewed 2022-04-24].

[114] HUOVINEN, Pasi, and Hannah PETERSEN. Particlization in hybrid models. Online. The European Physical Journal A, vol. 48 (November 2012), no. 11. ISSN 1434-601X. Available from: `https://doi.org/10.1140/epja/i2012-12171-9`. [viewed 2022-04-24].

[115] HOLOPAINEN, H., H. NIEMI, and K. J. ESKOLA. Event-by-event hydrodynamics and elliptic flow from fluctuating initial states. Online. Physical Review C, vol. 83 (March 2011), no. 3. ISSN 1089-490X. Available from: `https://doi.org/10.1103/physrevc.83.034901`. [viewed 2022-04-24].

[116] SHEN, Chun, and Li YAN. Recent development of hydrodynamic modeling in heavy-ion collisions. Online. Nuclear Science and Techniques, vol. 31 (December 2020), no. 12. ISSN 2210-3147. Available from: `https://doi.org/10.1007/s41365-020-00829-z`. [viewed 2022-04-24].

[117] OLIINYCHENKO, D., and H. PETERSEN. Deviations of the energy-momentum tensor from equilibrium in the initial state for hydrodynamics from transport approaches. Online. Physical Review C, vol. 93 (March 2016), no. 3. ISSN 2469-9993. Available from: `https://doi.org/10.1103/physrevc.93.034905`. [viewed 2022-04-24].

[118] PETERSEN, Hannah, Jan STEINHEIMER, Gerhard BURAU, Marcus BLE-ICHER, and Horst STÖCKER. Fully integrated transport approach to heavy ion reactions with an intermediate hydrodynamic stage. Online. Physical Review C, vol. 78 (October 2008), no. 4. ISSN 1089-490X. Available from: `https://doi.org/10.1103/physrevc.78.044901`. [viewed 2022-04-24].

[119] SKOKOV, V. V., and V. D. TONEEV. Semi-central In-In collisions and Brown-Rho scaling. Online. Physical Review C, vol. 73 (February 2006), no. 2. ISSN 1089-490X. Available from: `https://doi.org/10.1103/physrevc.73.021902`. [viewed 2022-04-24].

[120] KARPENKO, Iu. A., P. HUOVINEN, H. PETERSEN, and M. BLEICHER. Estimation of the shear viscosity at finite net-baryon density from $A+A$ collision data at $\sqrt{s_{\mathrm{NN}}}$ = 7.7 - 200 GeV. Online. Physical Review C, vol. 91 (June 2015), no. 6. ISSN 1089-490X. Available from: `https://doi.org/10.1103/physrevc.91.064901`. [viewed 2022-04-24].

[121] PANG, Longgang, Qun WANG, and Xin-Nian WANG. Effects of initial flow velocity fluctuation in event-by-event (3+1)D hydrodynamics. Online. Physical Review C, vol. 86 (August 2012), no. 2. ISSN 1089-490X. Available from: `https://doi.org/10.1103/physrevc.86.024911`. [viewed 2022-04-24].

[122] SCHÄFER, Anna, Iurii KARPENKO, Xiang-Yu WU, Jan HAMMELMANN, and Hannah ELFNER. Particle production in a hybrid approach for a beam energy scan of Au+Au/Pb+Pb collisions between $\sqrt{s_{\mathrm{NN}}}$ = 4.3 GeV and $\sqrt{s_{\mathrm{NN}}}$ = 200.0 GeV. Online. arXiv, 2021. Available from: `https://doi.org/10.48550/arxiv.2112.08724`. [viewed 2022-04-24].

[123] WEIL, J., V. STEINBERG, J. STAUDENMAIER, L. G. PANG, D. OLI-INYCHENKO, et al. Particle production and equilibrium properties within a new hadron transport approach for heavy-ion collisions. Online. Physical Review C, vol. 94 (November 2016), no. 5. ISSN 2469-9993. Available from: `https://doi.org/10.1103/physrevc.94.054905`. [viewed 2022-04-24].

[124] RYBCZYŃSKI, Maciej, Grzegorz STEFANEK, Wojciech BRONIOWSKI, and Piotr BOŻEK. GLISSANDO 2: glauber initial-state simulation AND more..., ver. 2. Online. Computer Physics Communications, vol. 185 (June 2014), no. 6, pp. 1759–1772. ISSN 0010-4655. Available from: `https://doi.org/10.1016/j.cpc.2014.02.016`. [viewed 2022-04-24].

[125] BRONIOWSKI, Wojciech, Maciej RYBCZYŃSKI, and Piotr BOŻEK. GLIS-SANDO: GLauber Initial-State Simulation AND mOre... Online. Computer Physics Communications, vol. 180 (January 2009), no. 1, pp. 69–83. ISSN 0010-4655. Available from: `https://doi.org/10.1016/j.cpc.2008.07.016`. [viewed 2022-04-24].

[126] BOŻEK, Piotr, Wojciech BRONIOWSKI, Maciej RYBCZYŃSKI, and Grzegorz STEFANEK. GLISSANDO 3: glauber initial-state simulation AND more, ver. 3. Online. Computer Physics Communications, vol. 245 (December 2019), p.

106850. ISSN 0010-4655. Available from: `https://doi.org/10.1016/j.cpc.2019.07.014`. [viewed 2022-04-24].

[127] KARPENKO, Iu, P. HUOVINEN, and M. BLEICHER. A 3+1 dimensional viscous hydrodynamic code for relativistic heavy ion collisions. Online. Computer Physics Communications, vol. 185 (November 2014), no. 11, pp. 3016–3027. ISSN 0010-4655. Available from: `https://doi.org/10.1016/j.cpc.2014.07.010`. [viewed 2022-04-24].

[128] BECATTINI, F., M. BUZZEGOLI, A. PALERMO, G. INGHIRAMI, and I. KARPENKO. Local polarization and isothermal local equilibrium in relativistic heavy ion collisions. Online. Physical Review Letters, vol. 127 (December 2021), no. 27. ISSN 1079-7114. Available from: `https://doi.org/10.1103/physrevlett.127.272302`. [viewed 2022-04-24].

[129] Production picoDst Size on DD. Online. The STAR Collaboration. 2022-04-23. Available from: `https://www.star.bnl.gov/public/comp/prod/localdata/DDpicosize.html`. [viewed 2022-04-24].

[130] PRUNEAU, Claude. Data analysis techniques for physical scientists. Cambridge University Press, 2017. ISBN 9781108416788.

[131] GORBUNOV, Sergey. On-line reconstruction algorithms for the CBM and ALICE experiments. Online. Doctoral Thesis. Frankfurt: Johann Wolfgang Goethe-Universität, 2013. Available from: `http://publikationen.ub.uni-frankfurt.de/frontdoor/index/index/docId/29538`. [viewed 2022-04-24].

[132] FRÜHWIRTH, R., M. REGLER, R. K. BOCK, H. GROTE, and D. NOTZ. Data analysis techniques for high-energy physics. 2nd ed. Cambridge, U.K: Cambridge University Press, 2000. ISBN 0521632196.

[133] ZYZAK, M., I. KISEL, I. KULAKOV, and I. VASSILIEV. The KF Particle Finder package for short-lived particles reconstruction for CBM. Online. GSI SCIENTIFIC REPORT PHN-NQM-EXP-49. 2012. Available from: `http://repository.gsi.de/record/51983/files/PHN-NQM-EXP-49.pdf`. [viewed 2022-04-24].

[134] KISEL, Ivan. Real-Time event reconstruction and analysis in CBM and STAR experiments. Online. Journal of Physics: Conference Series, vol. 1602 (July 2020), p. 012006. ISSN 1742-6596. Available from: `https://doi.org/10.1088/1742-6596/1602/1/012006`. [viewed 2022-04-24].

[135] ZYZAK, Maksym. KFParticle tutorial. Online. The STAR experiment. 2018. Available from: `https://drupal.star.bnl.gov/STAR/system/files/KFParticleTutorial_11.12.2018.pdf`. [viewed 2022-04-24].

[136] BRUN, Rene, and Fons RADEMAKERS. ROOT — An object oriented data analysis framework. Online. Nuclear Instruments and Methods in Physics Research Section A: Accelerators, Spectrometers, Detectors and Associated Equipment, vol. 389 (April 1997), no. 1-2, pp. 81–86. ISSN 0168-9002. Available from: `https://doi.org/10.1016/s0168-9002(97)00048-x`. [viewed 2022-04-24].

[137] STAR TPC photographs and drawings. Online. STAR: The STAR Collaboration. 2009. Available from: `https://www.star.bnl.gov/public/tpc/photos/tpc_photos.html`. [viewed 2022-04-24].

[138] ZYLA, P. A et al. Review of particle physics. Online. PTEP, vol. 2020 (2020), no. 8. Available from: `https://pdg.lbl.gov/2021/listings/contents_listings.html`. [viewed 2022-04-24].

[139] UPSAL, Isaac. Global polarization of the $\lambda/\overline{\lambda}$ system in the STAR BES. Online. Dissertation. The Ohio State University, 2018. Available from: `https://drupal.star.bnl.gov/STAR/files/UpsalThesisV4.pdf`. [viewed 2022-05-23].

[140] SELYUZHENKOV, Ilya. Acceptance effects in the hyperons global polarization measurement. Online. In: INTERSECTIONS OF PARTICLE AND NUCLEAR PHYSICS: 9th Conference CIPAN2006. Rio Grande, Puerto Rico (USA). AIP, 2006. Available from: https://doi.org/10.1063/1.2402736. [viewed 2022-04-25].

[141] SELYUZHENKOV, I. Anti-Lambda hyperon global polarization in Au+Au collisions at RHIC. Online. arXiv, 2007. Available from: `https://doi.org/10.48550/arxiv.nucl-ex/0702001`. [viewed 2022-04-24].

[142] UPSAL, Isaac. Determining eta weights for EPD event plane analysis. Online. The STAR experiment. 2019. Available from: `https://drupal.star.bnl.gov/STAR/blog/iupsal/determining-eta-weights-epd-event-plane-analysis`. [viewed 2022-04-28].

[143] BECATTINI, F., F. PICCININI, and J. RIZZO. Angular momentum conservation in heavy ion collisions at very high energy. Online. Physical Review C, vol. 77 (February 2008), no. 2. ISSN 1089-490X. Available from: `https://doi.org/10.1103/physrevc.77.024906`. [viewed 2022-04-28].